University of cambridge

Spectral and dynamical properties of disordered and noisy quantum spin models

Daniel Alexander Rowlands

Corpus Christi College

This dissertation is submitted for the degree of
Doctor of Philosophy

Cavendish Laboratory

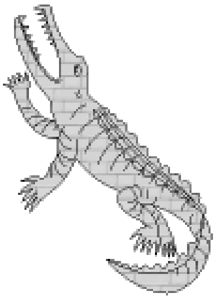

August 2018

Spectral and dynamical properties of disordered and noisy quantum spin models

by Daniel Alexander Rowlands

Abstract

This thesis, divided into two parts, is concerned with the analysis of spectral and dynamical characteristics of certain quantum spin systems in the presence of either I) quenched disorder, or II) dynamical noise.

In the first part, the quantum random energy model (QREM), a mean-field spin glass model with a many-body localisation transition, is studied. In Chapter 2, we attempt a diagrammatic perturbative analysis of the QREM from the ergodic side, proceeding by analogy to the single-particle theory of weak localisation. Whilst we are able to describe diffusion, the analogy breaks down and a description of the onset of localisation in terms of quantum corrections quickly becomes intractable. Some progress is possible by deriving a quantum kinetic equation, namely the relaxation of the one-spin reduced density matrix is determined, but this affords little insight and extension to two-spin quantities is difficult. We change our approach in Chapter 3, studying instead a stroboscopic version of the model using the formalism of quantum graphs. Here, an analytic evaluation of the form factor in the diagonal approximation is possible, which we find to be consistent with the universal random matrix theory (RMT) result in the ergodic regime. In Chapter 4, we replace the QREM's transverse field with a random kinetic term and present a diagrammatic calculation of the average density of states, exact in the large-N limit, and interpret the result in terms of the addition of freely independent random variables.

In the second part, we turn our attention to noisy quantum spins. Chapter 5 is concerned with noninteracting spins coupled to a common stochastic field; correlations arising from the common noise relax only due to the spins' differing precession frequencies. Our key result is a mapping of the equation of motion of n-spin correlators onto the (integrable) non-Hermitian Richardson-Gaudin model, enabling exact calculation of the relaxation rate of correlations. The second problem, addressed in Chapter 6, is that of the dynamics of operator moments in a noisy Heisenberg model; qualitatively different behaviour is found depending on whether or not the noise conserves a component of spin. In the case of nonconserving noise, we report that the evolution of the second moment maps onto the Fredrickson-Andersen model – a kinetically constrained model originally introduced to describe the glass transition. This facilitates a rigorous study of operator spreading in a continuous-time model, providing a complementary viewpoint to recent investigations of random unitary circuits.

Preface

The first chapter of this dissertation provides an introduction to the main concepts and methods we shall encounter in later chapters, whilst concluding remarks are contained in the final chapter. The intermediate chapters contain original material that is either published or in preparation for submission to peer review as follows:

Chapters 2 & 4: Daniel A. Rowlands and Austen Lamacraft. *Diagrammatic approaches to quantum random energy models*.
Chapter 3: *Stroboscopic quantum random energy model*. Whilst in preparation, the same result for the form factor appeared in (a preprint of) Ref. [1].
Chapter 5: Daniel A. Rowlands and Austen Lamacraft. *Noisy spins and the Richardson-Gaudin model*, Physical Review Letters 120 (9), 090401.
Chapter 6: Daniel A. Rowlands and Austen Lamacraft. *Noisy coupled qubits: operator spreading and the Fredrickson-Andersen model*. To appear in Physical Review B.

This dissertation is the result of my own work and includes nothing which is the outcome of work done in collaboration except as declared in the Preface and specified in the text. It is not substantially the same as any that I have submitted, or, is being concurrently submitted for a degree or diploma or other qualification at the University of Cambridge or any other University or similar institution except as declared in the Preface and specified in the text. I further state that no substantial part of my dissertation has already been submitted, or, is being concurrently submitted for any such degree, diploma or other qualification at the University of Cambridge or any other University or similar institution except as declared in the Preface and specified in the text. This dissertation does not exceed 60,000 words, including summary/abstract, tables, footnotes and appendices, but excluding table of contents, photographs, diagrams, figure captions, list of figures/diagrams, list of abbreviations/acronyms, bibliography and acknowledgements.

Daniel Alexander Rowlands
On the 6th of August, the Feast of the Transfiguration of the Lord, 2018

Acknowledgements

In the first place I express sincere gratitude to my supervisor Austen Lamacraft for his outstanding guidance over the last three years that has made this thesis possible; his remarkable insight and ingenuity have been an inspiration. The research contained here has also been facilitated by the financial support of the Engineering and Physical Sciences Research Council and the accommodation provided by Corpus Christi College.

The TCM group has provided an intellectually stimulating research environment. I thank in particular Gunnar Möller, Antonio García-García, David Khmelnitskii, and Michal Kwasigroch for useful discussions. I would also like to extend thanks to my fellow PhD students who could always be relied upon for engaging and diverse conversation, especially: Victor Jouffrey, Corentin Morice, Sam Smith, Lars Schonenberg, Bruno Loureiro, Tom Whitehead, Beñat Mencia, Philipp Verpoort, and Bart Andrews. Discussions with members of groups outside Cambridge have also been much appreciated: Sarang Gopalakrishnan, Alex Altland, Marko Žnidarič, and Roland Speicher come to mind in particular. My thanks extends also to my examiners, John Chalker and Andreas Nunnnenkamp, for their careful reading of my work and perceptive comments. In addition to research, it has been a pleasure to supervise numerous undergraduates – I am grateful to the students for challenging me with good questions.

Lastly, I thank all friends and family who have been of invaluable help through their willingness to listen, encourage, and advise; in particular, I am deeply thankful to my parents and sister for their constant support and love over the course of my life, and their particular generosity and patience during these years of doctoral study.

Contents

Preface **3**

Acknowledgements **5**

1 Introduction **11**
- 1.1 Disorder and localisation . . . 12
  - 1.1.1 Many-body localisation: a brief history . . . 13
  - 1.1.2 Weak localisation: semiclassical picture . . . 15
  - 1.1.3 Weak localisation: diagrammatics . . . 17
    - Disorder-averaged Green's function . . . 17
    - Born approximation . . . 18
    - Drude conductivity . . . 20
    - Diffusion . . . 21
    - Weak-localisation correction . . . 23
- 1.2 Random matrix theory . . . 25
- 1.3 Quantum graphs . . . 28
- 1.4 Operator spreading . . . 30

I Disordered spins **33**

2 Quantum random energy model: a diagrammatic approach **35**
- 2.1 Model . . . 35
  - 2.1.1 Hamiltonian and Hilbert space . . . 35
  - 2.1.2 Formal structure of the perturbation theory . . . 37
- 2.2 Disorder-averaged perturbation theory . . . 38
  - 2.2.1 Model of disorder . . . 38
  - 2.2.2 Born approximation . . . 39
  - 2.2.3 Self-consistent Born approximation . . . 42
  - 2.2.4 Diffusion ladder . . . 43
  - 2.2.5 Classical diffusion on the hypercube . . . 45
- 2.3 Transverse spin-spin correlations . . . 48
  - 2.3.1 Drude peak . . . 49
  - 2.3.2 Schwinger time . . . 49

2.3.3 Cooperon ladder in the diffusive regime . . . 53
2.4 Dynamics of the average density matrix . . . 54
2.4.1 Derivation of the quantum master equation . . . 55
2.4.2 Spectrum . . . 57
2.4.3 Permutation symmetry and dimensional reduction . . . 57
2.4.4 Reduced density matrix . . . 60
2.5 Conclusions . . . 61

3 Stroboscopic quantum random energy model as a quantum graph 63
3.1 Introduction . . . 63
3.2 Spectral statistics . . . 64
3.2.1 Numerics . . . 64
3.3 Spectral form factor in the diagonal approximation . . . 66
3.4 Conclusions . . . 71

4 Quantum random energy model with a random kinetic term 73
4.1 Model . . . 73
4.2 Spectral statistics . . . 74
4.3 Perturbation theory . . . 76
4.3.1 Noncrossing approximation . . . 76
4.4 Density of states . . . 78
4.5 Binary disorder . . . 78
4.6 Free probability . . . 80
4.6.1 Free independence . . . 80
4.6.2 Connection to random matrix theory . . . 82
4.7 Single-particle analogue . . . 84
4.7.1 Density of states . . . 84
4.8 Conclusions . . . 85

II Noisy spins 87

5 Noisy spins and the Richardson–Gaudin model 89
5.1 Background and model . . . 89
5.2 Density matrix and correlation functions . . . 91
5.3 Mapping to the Richardson–Gaudin model . . . 92
5.4 Equivalence to stochastic evolution . . . 93
5.5 Exact solution . . . 95
5.6 Conclusions and outlook . . . 98

6 Noisy coupled qubits: operator spreading and the Fredrickson–Andersen model 99
6.1 Motivation 100
6.2 Models and mapping 101
6.2.1 Models 101
6.2.2 Model C at strong noise: symmetric exclusion process for $\overline{O}$ 104
6.2.3 Model NC at strong noise: Fredrickson–Andersen model for $\overline{O \otimes O}$ 105
6.3 Phenomenology of fronts 107
6.3.1 Fronts in the FA model 107
6.3.2 Fronts in two dimensions 107
6.4 Details of the numerical simulation 109
6.5 Applied Phenomenology 110
6.5.1 Out-of-time-order correlation functions 110
6.5.2 Purity decay 111
6.6 Conclusions 113

7 Concluding remarks 115

A Harmonic analysis on $\mathbb{Z}_2^N$ 119

B Hamming scheme combinatorics 121

C Two-point correlators in the random kinetic quantum random energy model 123

D Effective Liouvillians for second-moment dynamics 129
D.1 Second-moment dynamics of Model C in the strong-noise limit 129
D.2 Effective Liouvillian for the second moment of model NC 130

Bibliography 133

Chapter 1

Introduction

"Esset etiam contra perfectionem universi... Esset [igitur] contra rationem providentiae, et perfectionis rerum, si non essent aliqua casualia [1]*."*

— St Thomas Aquinas, *Summa contra gentiles*, Bk 3, Ch 74

The unifying feature of the separate strands of work in this thesis is an attempt to develop analytical means of studying quantum many-body systems in which we have taken into account the unavoidable randomness present in real systems, either by the inclusion of 'quenched disorder' – reflecting our lack of knowledge of the heterogeneity in a system, caused for instance by defects and impurities – or 'dynamical noise', which tries to capture the influence of the coupling of the system to an external environment that is too large to be handled in a microscopically precise way. Understanding the physics displayed by even deterministic systems featuring a macroscopically large number of interacting particles impels us to consider highly simplified models that isolate only the essential elements required to exhibit the collective phenomenon of interest; ab initio simulations of course have a role to play too, but they are of more use in detecting the presence of exotic physics or establishing a realistic parameter regime for a model rather than identifying the relevant physical degrees of freedom. A quantum spin-1/2 model is just about the simplest abstraction of a quantum many-body system that we can conceive: a two-level system, the minimal nontrivial Hilbert space, on each site of a lattice and coupled by some interaction. By playing with the range of the interactions, external fields, lattice geometries, and disorder, virtually the whole gamut of condensed matter phenomenology can be elicited: from ferromagnetism and localisation, to fractionalised excitations and emergent gauge fields.

The first part of this thesis, dealing with disorder, takes the quantum random energy model (and some closely related derivatives) as a minimal model of a system with a many-body localisation transition. Most results in this field to date have concerned the localised phase, since the short localisation length there renders numerical studies of small systems quite informative, whilst analytical results have relied heavily on either the existence of an extensive number of local integrals of motion or else strong-disorder perturbation theory. Our principal aim will thus be to make progress by working from the delocalised (ergodic) side of the transition, drawing upon analogies to the study of single-particle disordered systems and few-body quantum chaos.

---

[1] "Moreover, it would be against the perfection of the universe . . . it would be contrary to the meaning of providence, and to the perfection of things, if there were no chance events."

When we turn to noisy systems in the second part, we consider two different problems. The first involves an investigation of how correlations relax in noninteracting spins when they experience a highly correlated noise: we find a decoherence-free subspace when the spin-1/2 degrees of freedom have identical energy splittings, but the presence of any quenched disorder (giving rise to inhomogeneous splittings) allows spin correlations to relax – the dynamics of the correlations are found to be described by an integrable model. In the final chapter, we turn to models of locally interacting spins in a stochastic field and exploit an exact mapping of the second operator moment to a classical stochastic model for strong-noise in order to study operator spreading via an out-of-time-order correlation function.

In the remainder of this introduction, we shall set out important background for the topics of localisation and operator spreading, as well as introducing some of the key concepts and methods we shall invoke: disorder-averaged diagrammatic perturbation theory, spectral statistics, random matrix theory, and quantum graphs.

1.1 Disorder and localisation

An elementary but fundamental prediction of solid state theory is that electrons can pass through a perfect crystal without resistance: the electronic wavefunctions take the form of Bloch waves that extend over the whole system. Notwithstanding the success of the band theory of solids, which is founded on single-particle Bloch wavefunctions, two features of real physical systems that are left out of this simple description, namely interactions and disorder, greatly enrich the range of collective phenomena that can be observed. The archetypal example of an interaction-driven metal-insulator transition is that which was first postulated by Mott in the 1940s, though it still remains to be fully understood [2]. As for the effect of disorder on a noninteracting system, the phenomenon of *Anderson localisation* stands at the heart of the field. In a seminal paper, Anderson argued that the elastic scattering of Bloch waves by a random potential can not only lead to the emergence of a finite resistivity, but can in fact dramatically modify the extended single-particle wavefunctions due to interference effects, rendering them exponentially localised in space with a resultant strong suppression of conductivity [3]. Disorder and interactions studied individually have led to a number of difficult problems of intense current interest, and so it goes without saying that the problem of studying their concerted effect is even more challenging. Current work on localisation in the presence of interactions — which we shall loosely call *many-body localisation* (MBL) — has yielded only a small number of analytical results, meaning that intuition is heavily guided by conjecture and numerical simulations. Much analysis of the Anderson metal-insulator transition has approached the transition from the insulating (strong disorder) side, however the development of a mature theory of *weak localisation* [4], in which the limit of weak disorder was studied, has also proved fruitful. Elegant qualitative insight into the connection between the weak- and strong-disorder regimes is provided by the scaling theory [5], which was followed by the self-consistent theory of Vollhardt and Wölfle [6] — this captured both the "gang of four" [5] scaling and the correct limiting behaviour for strong and weak disorder.

The motivation for the work in Chapter 2 is to attempt to develop a corresponding theory of *weak MBL*. Relying on analogies to the single-particle problem, we endeavour to find incipient features of MBL, present when disorder is weak, and give them a firmer theoretical foundation. Ultimately, we will see that this programme is unsuccessful; however, it remains a useful exercise to chart precisely where the analogies to weak localisation work and where they break down. We shall also find that the diagrammatic language we develop, despite becoming unwieldy in attacking the problem we set out to address, does at least provide a novel way of describing diffusion in our model.

In order to see how our work fits in to the literature, we shall now formulate the concept of MBL a little more carefully, firstly by relating it to the theory of single-particle Anderson localisation, and then by qualitatively summarising some of the associated phenomenology that has emerged in recent years. In section 1.1.2, we give a qualitative overview of weak localisation, emphasising its physical interpretation in terms of diffusive trajectories. Owing to the fact that drawing an analogy with the theory of weak localisation is the bedrock of our approach in Chapter 2, we recapitulate the quantitative details in section 1.1.3, using the language of disorder-averaged Green's functions and the associated diagrammatic perturbation theory.

1.1.1 Many-body localisation: a brief history

The paradigmatic model encoding the physics of localisation of noninteracting particles is the Anderson model

$$H = -t \sum_{<ij>} (c_i^\dagger c_j + \text{h.c.}) + \sum_i \epsilon_i c_i^\dagger c_i, \tag{1.1}$$

which is simply a tight-binding model with random single-particle energies drawn from a uniform distribution in the interval $-W/2 \leq \epsilon_i \leq W/2$, with W thus setting the disorder strength. The key parameter controlling the phase behaviour is t/W; let us first examine the extreme cases. If $t = 0$, then the electrons occupy localised states of energy ϵ_i resulting in an insulating phase. The other extreme of $W = 0$ of course describes free electrons occupying Bloch states – a metal if the band is not fully filled. Classical intuition would suggest that strong enough disorder will always localise a particle; that is, a particle exploring a random potential landscape will always get trapped in a well that is locally very deep if disorder is much larger than its kinetic energy. In the quantum mechanical case we can consider a perturbation theory in the hopping

$$|i'\rangle = |i\rangle + \sum_j \frac{t_{ij}}{\epsilon_i - \epsilon_j} |j\rangle \,. \tag{1.2}$$

Since $\epsilon_i - \epsilon_j \sim W$, it looks like the localised state $|i\rangle$ is only weakly perturbed in the off-resonance scenario when disorder is strong ($W \gg t$). Whereas when the hopping is large enough, strong hybridisation may generate extended states. There are some caveats in handling the convergence of such a perturbation theory (locator expansion), but the conclusion can nonetheless be put on rigorous mathematical footing using alternative approaches: Anderson localisation is inevitable for strong enough disorder in arbitrary dimension [7]. A more interesting question is to pin down the transition: for what value of t/W does localisation occur? The scaling theory of localisation yields the surprising result that all states are localised in one and two dimensions for nonzero disorder (i.e. the transition is at $t/W \to \infty$), whilst in three dimensions there is a metal-insulator transition at finite t/W [5]. The case of one dimension was established mathematically (the one-dimensional Anderson model has a dense pure point spectrum) [8] prior to the development of the scaling theory, whereas the results for $d > 1$ lack mathematical proof but are widely accepted (on the grounds of the heuristic scaling arguments and extensive numerical evidence). In three dimensions, physical reasoning has further formed our understanding of the transition: Mott suggested that there is scope for coexistence of localised and delocalised states [9]. His argument is that localised and delocalised states cannot coexist at the same energy (since they would hybridise, leaving only delocalised states), but they can exist as distinct energy bands separated by a mobility edge. One can think about the Anderson transition in terms of fixing the disorder and tuning the carrier density to move the chemical potential through the mobility edge, or alternatively, as fixing the chemical potential and tuning disorder strength to shift the mobility edge. The wavefunction of localised states, $\psi_i(r) \sim \exp(-|r - r_i|/\xi)$, is characterised by a localisation length ξ, which is expected to exhibit power law scaling typical of critical phenomena, $\xi \sim |\epsilon - \epsilon_c|^{-\nu}$, approaching the metallic phase.

Having set the scene for the single-particle problem, we can begin to explore how this picture is affected by the presence of interactions. A useful insight emerges if we consider electron-phonon coupling. In the regime of localised states, when the hopping is off-resonance with the energy mismatch of neighbouring states, the states may nonetheless be coupled by phonons. Since electrons can hop between any two localised states by scattering inelastically off phonons, we anticipate finite conductivity at nonzero temperature – this is Mott's variable-range hopping mechanism [10]. By analogy, electron-hole pairs could provide a bath of excitations and so the issue to resolve is whether the electron-electron interaction will impart a finite hopping conductivity. Fleishman and Anderson proposed the answer that, if the temperature is low enough and the interaction sufficiently short-ranged (the Coulomb interaction in 3d being a marginal case), the electron-electron interaction does not destabilise the localised phase [11]. Complementary to this result are the Altshuler-Aronov corrections (due to the electron-electron interaction) to the conductivity [12]. Weak localisation will be introduced in the next section, but for now it suffices to note that it is the precursor to localisation that is observable as a reduction in conductivity in the metallic phase; Altshuler, Aronov, and Khmelnitskii demonstrated that at high temperature, electron-electron scattering results in a dephasing[2] that reduces the magnitude of the weak localisation effect [13].

---

[2] Altshuler and Aronov also noted that, in addition to the direct effect of the electron-electron interaction on inelastic scattering, it is also responsible for renormalising elastic impurity scattering by virtual electron-hole excitations. This is responsible for a negative correction to the conductivity at low temperature [12].

A more complete analysis of the effect of the electron-electron interaction on localisation was that of Basko, Aleiner, and Altshuler [14]. Their central claim (on the basis of perturbation theory in the interaction) is that there is a finite-temperature metal-insulator transition – the MBL transition – for which the DC conductivity vanishes below T_c (in the absence of coupling to a thermal bath that would lead to the phonon-assisted hopping discussed above). The interaction can be seen to generate a hopping in the many-body Fock space, giving rise to the interpretation of MBL as Anderson localisation in Fock space.

We shall give here only the tersest of outlines of the phenomenology of MBL that has emerged in recent years, but for a fuller account of the literature we refer to the recent review articles Refs. [15–17] and the references therein.

Instead of asking whether interactions are able to generate a finite conductivity, we can rephrase the question and ask whether interactions are able to act as a thermal bath by means of which a closed system can come to thermal equilibrium under unitary time evolution [18]. This leads us to characterise the MBL transition as an ergodicity-breaking transition demarcating an ergodic phase from an MBL phase. The ergodic (thermal) phase has the property that, for any small subsystem, the coupling to the remainder of the system replicates that of coupling to a thermal reservoir such that the subsystem attains thermal equilibrium at long times. In such a phase, all information about the initial state is locally inaccessible (encoded in the large-scale entanglement structure) and the state is fully described by only a few parameters (the Lagrange multipliers associated with extensive conserved quantities: temperature, chemical potential etc.). In the MBL phase, thermalisation does not occur and information about the initial state remains present in a small subsystem as $t \to \infty$, a clear indicator of the invalidity of the ergodic hypothesis and equilibrium statistical mechanics. The origin of ergodicity-breaking has been found in the existence of an extensive number of conserved quantities – local integrals of motion (LIOMs) – developing in the MBL phase; this is a novel kind of emergent integrability that has led to a rigorous proof of MBL in a one-dimensional spin chain, and motivated the construction of the phenomenological l-bit model of the MBL phase [19–21]. In section 1.4, we note how MBL integrability manifests itself in dynamical properties, such as the dynamics of entanglement growth. We end this section by noting that the MBL transition itself is not yet well understood, but phenomenological strong-disorder renormalisation group approaches in one dimension have shed some light [22–24].

1.1.2 Weak localisation: semiclassical picture

Localisation can be studied perturbatively in the disorder by approaching the localised state from the extended eigenstates of the clean system. The presence of disorder can be seen to induce an effective attractive interaction (a fact most clearly discerned by using the replica method to treat disorder, but also apparent in the diagrammatics of the next section), which leads to the onset of new collective phenomena of the electrons. Early signs of localisation manifest themselves in the weakly disordered metallic phase, the classic example being a reduction in the conductivity. We shall now offer a qualitative interpretation of this correction, before providing a more quantitative account in the next section.

The semiclassical understanding of electronic transport in a weakly disordered medium is that of electrons scattering off impurities, with a characteristic scattering rate τ^{-1}, giving rise to a concept of electronic trajectories (i.e. electron motion can be described classically on time scales larger than τ). Quantum mechanically, the probability P for an electron to propagate between two points r_1 and r_2 is given by the square modulus of the sum of the probability amplitudes A_p associated with the possible paths p connecting r_1 and r_2

$$P(r_1 \to r_2) = \sum_p |A_p|^2 + \sum_{p \neq q} A_p A_q^*. \tag{1.3}$$

In general, the second (interference) term vanishes due to the fact that the many possible paths of different length give rise to a strongly fluctuating phase of the amplitudes A_p. That said, there exist special trajectories where interference is crucial. If we consider a path with a self-intersection, then the amplitudes for the two trajectories traversing the loop in opposite directions (denoted + an −) have the same phase provided time-reversal symmetry is not broken. As a result, the probability of returning to the same point (backscattering) is enhanced by constructive interference: $P(r_1 \to r_1) = |A_+ + A_-|^2 = 4|A_+|^2$. We show in section 1.1.3 that the corresponding reduction in conductivity has a strong dependence on spatial dimension. Using this observation, we can make a rough estimate of the effect on conductivity by noticing that the relative magnitude of the correction is set by the probability of a self-intersection [25]. On long time scales ($t \gg \tau$), electron motion is diffusive and so the volume accessible to an electron is $\sim (Dt)^{3/2}$. Due to the quantum nature of the electron, we do not imagine a point-particle trajectory but instead a tube of width $\sim \lambda$ (de Broglie wavelength), whose volume increases in an interval dt by $\sim \lambda^2 v_F \, dt$ (where v_F is the Fermi velocity). In three dimensions we find

$$\Delta\sigma^{3\mathrm{d}}/\sigma_{\mathrm{Drude}} \sim \int_{\tau}^{\tau_\phi} dt \, \frac{\lambda^2 v_F}{(Dt)^{3/2}} \sim -\left(\frac{\lambda}{l}\right)^2 + \frac{\lambda^2}{l L_\phi}, \tag{1.4}$$

where the scattering time τ fixes the short-time cutoff below which electron motion is ballistic, and the upper cutoff is determined by the phase coherence time τ_ϕ (or the escape time defined by the sample size, if it is less than τ_ϕ) above which interference effects are not possible due to phase relaxation by inelastic scattering mechanisms. In light of the definitions $D = \frac{1}{3} v_F^2 \tau$, $l = v_F \tau$, $L_\phi = v_F \tau_\phi$, and $\lambda \sim k_F^{-1}$ (we adopt $\hbar = 1$ throughout), the relative magnitude of the correction estimated in (1.4) matches the result of the full calculation reported in (1.34) for the three-dimensional case.

The weak localisation correction was first explained in terms of the interference of time-reversed trajectories by Larkin and Khmelnitskii [26], and later developed more rigorously in terms of a semiclassical path-integral approach by Chakravarty and Schmid [27]. We can establish the relationship between the trajectory approach and the upcoming diagrammatics by formulating the interference term using real-space propagators [28]. The amplitude associated with propagation around a closed loop L (and its time reversal $\bar{L}$) can be expressed as a product of the transition amplitudes between impurity-scattering events (occurring at space coordinates r_i). If we take a contribution for scattering from n impurities, we have

$$A_L = \int dr_2 \dots dr_{n-1}\, G^{(R)}(r_1, r_2) \dots G^{(R)}(r_{n-1}, r_n) \tag{1.5}$$

$$A_{\bar{L}} = \int dr_2 \dots dr_{n-1}\, G^{(R)}(r_n, r_{n-1}) \dots G^{(R)}(r_2, r_1) \tag{1.6}$$

where $G^{(R)}(r_1, r_2; i\omega_n)$ is the retarded Green's function, $r_1 = r_n$ (closed loop), and the frequency variable has been dropped for clarity. Recalling that the complex conjugate of the retarded Green's function is the advanced counterpart ($[G^R(r_1, r_2)]^* = G^A(r_2, r_1)$), then the interference term (dropping the spatial integrals for brevity) is of the form

$$A_L A_{\bar{L}}^* = \prod_i^{n-1} G^{(R)}(r_i, r_{i+1}) G^{(A)}(r_i, r_{i+1}). \tag{1.7}$$

Diagrammatically, this can be described by the cooperon ladder diagram that appears, albeit in momentum space, in section 1.1.3 (see Figure 1.4).

1.1.3 Weak localisation: diagrammatics

Disorder-averaged Green's function

The conductivity of a free-electron gas is infinite. In order to make contact with the finite conductivity predicted by the semiclassical picture of electron transport we must develop a microscopic theory that accounts for the acquisition of a finite scattering time for the electron quasiparticles due to impurity scattering; this can be done by perturbing the noninteracting Hamiltonian, $H_0 = \sum_{\boldsymbol{k}} \epsilon_{\boldsymbol{k}} \psi_{\boldsymbol{k}}^\dagger \psi_{\boldsymbol{k}}$, with a random impurity potential V. We begin by computing the basic element of the diagrammatic expansion, the disorder-averaged Matsubara Green's function. We refer to the literature for more thorough treatments of the diagrammatic impurity-averaging technique [29–32].

Beginning in a very general fashion, one can write down the full Matsubara Green's function[3] in the presence of an impurity potential $V(r) = \sum_{i=1}^{N_{\text{imp}}} v(r - r_i)$, which is the potential induced by N_{imp} impurities each generating a potential $v(r)$,

$$\begin{aligned} G(\boldsymbol{k}, \boldsymbol{k'}; i\omega_n) = {} & G^0(\boldsymbol{k}, i\omega_n)\delta_{\boldsymbol{k},\boldsymbol{k'}} + G^0(\boldsymbol{k}, i\omega_n) V(\boldsymbol{k} - \boldsymbol{k'}) G^0(\boldsymbol{k'}, i\omega_n) + \\ & \int d\boldsymbol{k}_1\, G^0(\boldsymbol{k}, i\omega_n) V(\boldsymbol{k} - \boldsymbol{k}_1) G^0(\boldsymbol{k}_1, i\omega_n) V(\boldsymbol{k}_1 - \boldsymbol{k'}) G^0(\boldsymbol{k'}, i\omega_n) + \dots \end{aligned} \tag{1.8}$$

---

[3] We point out that this is both a 'Green's function' in the language of many-body theory (a time-ordered average of field operators [33, 34]) as well as a bona fide Green's function of the single-particle Schrödinger equation, which in turn is equal to a matrix element of the resolvent operator for the Hamiltonian. In Chapter 2, the presence of interactions in the Hamiltonian mean that the Green's functions of many-body theory no longer coincide with resolvents; we are thus careful to exclusively use the latter terminology in that section.

Figure 1.1 illustrates how this perturbation series can be depicted using Feynman diagrams.

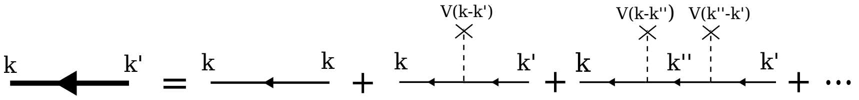

FIGURE 1.1: Full Green's function for a particle scattered by an impurity potential $V(r)$.

It is clear that the Fourier components of the potential depend on the positions of all the impurities, information which is inaccessible in practice, and thus we instead take a quenched disorder average over the position of all the impurities. Without further approximations, this would require the calculation of disorder averages of products of the potential, $\langle V(k_1)\dots V(k_n)\rangle$, to arbitrary order. This would enable us to account for all possible multiple scattering processes that appear at a given order in the impurity potential [31] . However, we shall instead adopt a minimal model for the sake of performing the disorder averages more efficiently. The disorder potential $V(r)$ shall be considered to be a random function with Gaussian distribution $P[V] = \exp\left(-\frac{1}{2\gamma}\int d\boldsymbol{r}\ V(r)^2\right)$: a disorder average now corresponds to a functional average with measure $P[V]\mathfrak{D}V$. The distribution is completely described by its first two moments

$$\mathbb{E}[V(\boldsymbol{r})] = 0 \quad \text{and} \quad \mathbb{E}[V(\boldsymbol{r})V(\boldsymbol{r'})] = \gamma\delta(\boldsymbol{r}-\boldsymbol{r'}), \tag{1.9}$$

where γ is the parameter encoding the disorder strength. We shall rewrite γ in terms of the density of states at the Fermi energy, $g(0)$, and another parameter, τ, which shall turn out to be the scattering time (i.e. momentum relaxation time due to impurity scattering),

$$\gamma = \frac{1}{2\pi g(0)\tau}, \tag{1.10}$$

in order to simplify future results. This is the Gaussian white noise model of disorder [35, 36]: we have obviated the need to specify higher-order moments of the potential (by assuming the potential fluctuations are purely Gaussian), and furthermore, we have assumed that the impurity potential fluctuations are delta-function correlated, implying that the potential of a single impurity has a flat Fourier spectrum (white noise).

Born approximation

Upon disorder averaging (1.8) (note that this restores translation invariance), the series can be resummed in terms of a self-energy to give the Dyson equation

$$\mathbb{E}[G(\boldsymbol{k}, i\omega_n)] = G^0(\boldsymbol{k}, i\omega_n) + G^0(\boldsymbol{k}, i\omega_n)\Sigma(\boldsymbol{k}, i\omega_n)\,\mathbb{E}[G(\boldsymbol{k}, i\omega_n)], \tag{1.11}$$

where the self-energy $\Sigma(\boldsymbol{k}, i\omega_n)$ is the sum of one-particle irreducible diagrams; the corresponding diagrammatic representation is given in Figure 1.2. Evaluating the lowest-order (nonvanishing) diagram, corresponding to the first Born approximation [31]

$$\Sigma_{\mathrm{BA}}(i\omega_n) = \gamma \sum_{\boldsymbol{k}} G^0(\boldsymbol{k}, i\omega_n) = \gamma \sum_{\boldsymbol{k}} \frac{1}{i\omega_n - \xi_{\boldsymbol{k}}} \tag{1.12}$$

$$= \gamma g(0) \int_{-\infty}^{\infty} \frac{d\epsilon}{i\omega_n - \epsilon}, \tag{1.13}$$

where in the second line we have replaced the momentum summation by a sum over energy weighted by the density of states, which we have approximated by its value at the Fermi energy, $g(0)$. Moreover, we have made the approximation of taking the limits of the integral to infinity, allowing us to innocuously shift the integration variable by the chemical potential ($\xi_k = \epsilon_k - \mu$ being the single-particle energy relative to the chemical potential). The (formally divergent) real part of the integral constitutes a renormalisation of the chemical potential and is therefore not of interest, whereas the imaginary part of the integrand is a nascent delta function (in the limit of small ω_n, according to the Sokhotski-Plemelj formula), hence

$$\mathrm{Im}[\Sigma_{\mathrm{BA}}(i\omega_n)] = -\frac{1}{2\tau}\,\mathrm{sgn}(\omega_n). \tag{1.14}$$

For the rest of this section we shall drop the $\mathrm{Im}[\ldots]$ notation and use $\Sigma(i\omega_n)$ as a shorthand for $i\,\mathrm{Im}[\Sigma(i\omega_n)]$. We can upgrade the calculation by repeating it within the self-consistent Born approximation (SCBA) [28, 31]. The bare propagator in the wigwam diagram for the first Born approximation can be replaced with the full propagator in (1.8), thus accounting for all the rainbow diagrams

$$\Sigma_{\mathrm{SCBA}}(i\omega_n) = \gamma g(0) \int \frac{d\epsilon}{i\omega_n - \epsilon - \Sigma_{\mathrm{SCBA}}(i\omega_n)}. \tag{1.15}$$

Provided that the disorder is weak enough (such that the imaginary part of the self-energy is small), one can check by substitution that self-consistency can be achieved by asserting that Σ_{SCBA} is unchanged from the self-energy computed in (1.14). Solving the Dyson equation (1.11) for the full SCBA Green's function we find

$$\mathbb{E}[G(\boldsymbol{k}, i\omega_n)] = \frac{1}{i\omega_n - \xi_k + \frac{i}{2\tau}\,\mathrm{sgn}(\omega_n)}. \tag{1.16}$$

The SCBA is sometimes alternatively known as the noncrossing approximation (diagrammatically, no impurity lines cross in the rainbow diagrams). It is important to be able to justify why the crossed diagrams can be neglected (at a given order) in the self-energy. For instance, at second order in γ we find that the ratio of uncrossed to the crossed diagram (see Figure 1.2) is $k_F l$, where k_F is the Fermi wavevector and $l = v_F \tau$ the mean free path. This can be ascertained by considering the volume of momentum space for which the Green's functions energy arguments are approximately at the Fermi surface; the uncrossed diagram has two momentum integrals that independently range over the Fermi surface whereas the crossing imposes a constraint (due to momentum conservation) that restricts the domain on which the integrand is large.

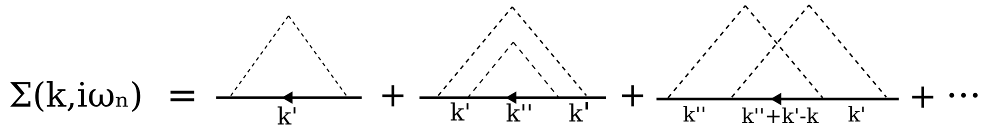

FIGURE 1.2: Self-energy for the disorder-averaged Green's function. The first term is the wigwam diagram that yields the (first) Born approximation. The second and third diagrams illustrate the uncrossed (rainbow) and crossed diagrams, which are respectively included and excluded in the self-consistent Born approximation. Note that the Green's function lines in this figure are 'bare'.

Drude conductivity

The Kubo formula expresses the electrical conductivity in terms of a retarded current-current correlation function [37]

$$\sigma_{ab}(q,\omega) = \frac{i}{\omega}\Pi^R_{ab}(q,\omega) - \frac{ne^2}{im\omega}\delta_{ab}, \tag{1.17}$$

defining n as the electron number density. To facilitate diagrammatic analysis we study the imaginary-time[4] correlator $\Pi_{ab}(q,\tau-\tau') = -\frac{1}{V}\langle \mathrm{T}_\tau[j_a(q,\tau)j_b(-q,\tau')]\rangle$, which can be written in terms of electron operators as

$$\begin{aligned}\Pi_{ab}(q,\tau-\tau') = -\frac{1}{V}\left(\frac{e}{2m}\right)^2 &\sum_{k\sigma,k'\sigma'}(2k_a+q_a)(2k'_b-q_b)\\ &\times\left\langle \mathrm{T}_\tau[\psi^\dagger_\sigma(k,\tau)\psi_\sigma(k+q,\tau)\psi^\dagger_{\sigma'}(k',\tau')\psi_{\sigma'}(k'-q,\tau')]\right\rangle.\end{aligned} \tag{1.18}$$

We can express this exactly in terms of the full Matsubara Green's function (1.8) using Wick's theorem, owing to the absence of an interaction term in the Hamiltonian. Performing the summation over spin indices σ, σ' and transforming to bosonic Matsubara frequency (Ω_n) space gives

$$\Pi_{ab}(q,i\Omega_n) = \frac{e^2}{2m^2\beta V}\sum_{k,k',\omega_n}(2k_a+q_a)(2k'_b+q_b)G(k+q,k'+q;i\omega_n+i\Omega_n)G(k',k;i\omega_n). \tag{1.19}$$

Carrying out the Gaussian white noise disorder average generates the diagrammatic expansion in the disorder strength. We shall work with skeleton diagrams built from the dressed SCBA Green's function (instead of the free Green's function), thus accounting for the leading-order effect of disorder on electron propagation. At the lowest order of approximation, we compute the bare conductivity bubble without vertex corrections (first diagram in Figure 1.3). To proceed we first perform the Matsubara summation over ω_n in the conventional way by expressing it as a contour integral

$$\Pi_{ab}(q,i\Omega_n) = \frac{1}{2\pi i V}\int_C dz\sum_{\boldsymbol{k}}\frac{e(2k_a+q_a)}{2m}\frac{e(2k_b+q_b)}{2m}\,\mathbb{E}[G(k,z)]\,\mathbb{E}[G(k{+}q,z{+}i\Omega_n)]\tanh\left(\frac{\beta z}{2}\right), \tag{1.20}$$

---

[4] Context will distinguish between the elastic scattering time, τ, and the imaginary-time variable also denoted τ.

where the disorder averaged Green's function (1.16) has been analytically continued to the complex z-plane, and the contour C enclosing the poles of the auxiliary function at $z = i\omega_n$ is inflated to infinity, excluding the branch cuts at $\mathrm{Im}[z] = 0$ and $\mathrm{Im}[z + i\Omega_n] = 0$ on which the two Green's functions are respectively singular. Parameterising the integral around the branch cuts by a real parameter, analytically continuing to real frequency ($i\Omega_n \to \omega + i\eta$ with $\eta \to 0^+$) to obtain the retarded correlator, and then taking the $q \to 0$ limit

$$\Pi^R_{ab}(q = 0, \omega) = \frac{e^2}{2\pi i m^2 V} \sum_{\boldsymbol{k}} k_a k_b \int_{-\infty}^{\infty} dE \, \Big(\bar{G}^R(k, E)\bar{G}^R(k, E + \omega) - \bar{G}^A(k, E)\bar{G}^R(k, E + \omega) + \\ \bar{G}^A(k, E - \omega)\bar{G}^R(k, E) - \bar{G}^A(k, E - \omega)\bar{G}^A(k, E)\Big) \tanh\left(\frac{\beta E}{2}\right), \tag{1.21}$$

where the shorthand $\bar{G}^R(k, E)$ and $\bar{G}^A(k, E)$ denote the retarded and advanced averaged Green's functions arising from the respective analytic continuations $z \to \omega + i\eta$ and $z \to \omega - i\eta$ of $\mathbb{E}[G(k, z)]$. After integrating by parts, the E-integral can be readily evaluated by making the approximation that $\mathrm{sech}^2(\frac{\beta}{2}(E - \mu)) \to \frac{4}{\beta}\delta(E - \mu)$ at low temperature — that is, only energies close to the Fermi energy contribute to the integral. The remaining $\boldsymbol{k}$-summation can be replaced by an integral over energy together with an angular average over $\boldsymbol{k}$, the latter giving $\frac{1}{4\pi} \int \sin(\theta) d\theta d\phi \; k_a k_b = \frac{1}{3}k^2\delta_{ab}$. Evaluating the remaining energy integral by Taylor expanding the logarithmic integrand to leading order in ω (we are interested in $\lim_{\omega\to 0} \lim_{q\to 0} \sigma_{ab}(q, \omega)$), we obtain, upon substitution into the Kubo formula (1.17), the conductivity

$$\sigma(q = 0, \omega \ll \tau^{-1}) = \frac{ne^2\tau}{m} \frac{1}{1 - i\omega}. \tag{1.22}$$

In the zero-frequency limit this immediately yields the semiclassical Drude formula

$$\sigma(\omega \to 0) = \frac{ne^2\tau}{m}. \tag{1.23}$$

The obvious follow-up question is to ask about the effect of vertex corrections to the conductivity bubble. The simplest correction is to dress the current vertex with the ladder diagrams (first line of Figure 1.3): it turns out that this correction vanishes in the $q \to 0$ limit for the Gaussian white noise model of disorder [35]. For the case of a more microscopically realistic impurity potential, the simplest effect of the ladder diagrams is to renormalise the scattering time τ to a new transport time τ_{tr}.

Diffusion

Semiclassical electronic transport theory presupposes the idea of diffusive electron motion, however no evidence of this has appeared in either the single-particle Green's function or the transverse conductivity. However, we shall find that diffusive modes emerge when considering the charge susceptibility, the density-density correlator controlling the longitudinal

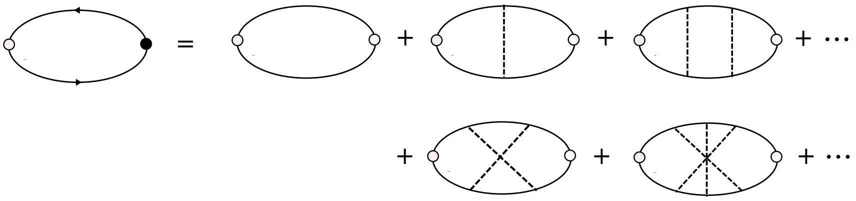

FIGURE 1.3: Diagrammatic expansion of a two-particle correlation function (conductivity or charge susceptibility in this chapter). Empty and filled circles represent bare and dressed vertices respectively. The first diagram on the right-hand side is the bare pair-bubble, the whole first line constitutes the ladder diagrams, and the second line is the series of maximally-crossed diagrams.

conductivity, and it is this to which we now turn. We proceed as before by working with the imaginary-time correlator

$$\chi(q,\tau) = -\frac{e^2}{V} \sum_{k\sigma,k'\sigma'} \left\langle \mathrm{T}_\tau[\psi^\dagger_\sigma(k,\tau)\psi_\sigma(k+q,\tau)\psi^\dagger_{\sigma'}(k',0)\psi_{\sigma'}(k'-q,0)] \right\rangle, \tag{1.24}$$

the only difference being that the bare charge vertex lacks the momentum-dependent factor of the bare current vertex in (1.18). This difference is crucial, for now the charge vertex is nontrivially renormalised by the series of ladder diagrams in Figure 1.3, the so-called diffuson,

$$\mathcal{D}(q;i\omega_n,i\Omega_n) = \left(1 - \frac{1}{2\pi g(0)\tau V}\sum_k \mathbb{E}[G(k+q,i\omega_n+i\Omega_n)]\,\mathbb{E}[G(k,i\omega_n)]\right)^{-1}. \tag{1.25}$$

Computation of the pair-bubble

$$\begin{aligned}\Pi(q;i\omega,i\omega_n+i\Omega_n) &= \frac{1}{2\pi g(0)\tau}\int\frac{dS_k}{4\pi}\int d\xi\; g(\xi)\\ &\times\left(\frac{1}{i(\omega_n+\Omega_n)-\xi_{k+q}+\frac{i}{2\tau}\operatorname{sgn}(\omega_n+\Omega_n)}\right)\left(\frac{1}{i\omega_n-\xi_k+\frac{i}{2\tau}\operatorname{sgn}(\omega_n)}\right),\end{aligned} \tag{1.26}$$

can be done by once again taking a constant density of states $g(\xi) \approx g(0)$, and then linearising the dispersion in q according to $\xi_{k+q} \approx \xi_k + \boldsymbol{v_F}\cdot\boldsymbol{q}$. The ξ-integral can be evaluated by the residue theorem, before the final average over solid angle (S_k) can be completed by expanding the integrand to leading order in Ω_n and q ($\Omega_n\tau \ll 1, qv_F\tau \ll 1$). Observing that the aforementioned contour integral trivially vanishes for $\operatorname{sgn}(\omega_n+\Omega_n) = \operatorname{sgn}(\omega_n)$, we find for the diffuson

$$\mathcal{D}_{++} = \mathcal{D}_{--} = 1 \qquad \mathcal{D}_{-+} = \frac{1}{(Dq^2+\Omega_n)\tau} \qquad \mathcal{D}_{+-} = \frac{1}{(Dq^2-\Omega_n)\tau}, \tag{1.27}$$

where the subscript is the ordered pair $(\mathrm{sgn}(\omega_n), \mathrm{sgn}(\omega_n + \Omega_n))$, and the diffusion constant has been defined as $D = \frac{1}{3}v_F^2\tau$. The charge susceptibility

$$\chi(q, i\Omega_n) = \frac{2e^2}{\beta V}\sum_{k,\omega_n}\mathbb{E}[G(k+q, i\omega_n + i\Omega_n)]\,\mathbb{E}[G(k, i\omega_n)]\mathcal{D}(q; i\omega_n, \Omega_n), \tag{1.28}$$

can now be dealt with in the same way as (1.20), thus establishing the diffusive form of the retarded charge susceptibility

$$\chi^R(q, w) = \frac{2e^2 g(\epsilon_F)Dq^2}{Dq^2 - i\omega}. \tag{1.29}$$

Weak-localisation correction

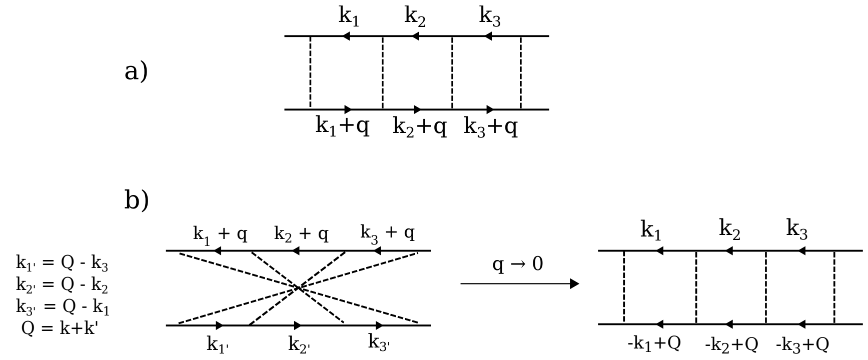

FIGURE 1.4: a) An example of a 'particle-hole' ladder diagram of which the diffuson is comprised. b) On the left is a maximally crossed diagram of which the cooperon is comprised, and on the right the diagram has been 'unfolded' (by reversing the direction of the advanced Green's function lines) to transform it into a 'particle-particle' ladder diagram. The propagator lines denote SCBA Green's functions (for aesthetic reasons they have not been emboldened to differentiate them from bare Green's functions, as done in Figure 1.1).

We now have all the elements we need to reproduce the classic result that, in one and two spatial dimensions, the first quantum correction to the Drude conductivity is negative – the so-called weak localisation phenomenon. Although we argued that diagrams with a pair of crossed impurity lines are suppressed by a factor of $(k_F l)^{-1}$ relative to their uncrossed counterpart at the same order, we shall find that an infinite subset of crossed diagrams are responsible for a correction to the conductivity that can become large at low temperature. Crossed diagrams were first analysed in the context of electron transport in the 1960s by Langer and Neal [38], but it was not until the work of Gor'kov, Larkin, and Khmelnitskii that the series of maximally crossed diagrams was related to weak localisation [4] and interpreted in terms of the interference of time-reversed diffusive trajectories [26], as discussed in section 1.1.2. The maximally crossed vertex correction (we shall continue to neglect crossed diagrams in the self-energy) to the conductivity bubble is known as the cooperon and is shown on the second line of Figure 1.3; by reversing the direction of one of the Green's function lines (see Figure 1.4) we can sum the geometric series analogously to the diffuson,

$$C(q;i\omega_n,i\Omega_n)=\frac{\gamma^2\sum_k\mathbb{E}[G(q-k,i\omega_n+i\Omega_n)]\,\mathbb{E}[G(k,i\omega_n)]}{1-\gamma\sum_k\mathbb{E}[G(q-k,i\omega_n+i\Omega_n)]\,\mathbb{E}[G(k,i\omega_n)]}. \tag{1.30}$$

Owing to the relations $\xi_k=\xi_{-k}$ and $\xi_{k+q}\approx\xi_k+\boldsymbol{v}\cdot\boldsymbol{q}$, the pair-bubble is identical to that of (1.26) to leading order in Ω_n and q. Hence, the cooperon is

$$C(q;i\omega_n,i\Omega_n)=\frac{1}{2\pi g(0)\tau V}\left(\frac{\theta[-\omega_n(\omega_n+\Omega_n)]}{(Dq^2+|\Omega_n|)\tau}\right). \tag{1.31}$$

Dressing the current vertex with the cooperon, we can write down the correction to the current-current correlator in the $q\to 0$ limit (note that the momentum flow through the cooperon is $q'=k+k'+q$)

$$\begin{aligned}\Delta\Pi_{ab}(q=0,i\Omega_n)=\frac{2e^2}{\beta m^2V^2}&\sum_{k,k',\omega_m}k_ak'_b\,\mathbb{E}[G(k,i\omega_n)\,\mathbb{E}[G(k,i\omega_n+i\Omega_n)\\&\times C(k+k',i\Omega_n)\,\mathbb{E}[G(k',i\omega_n)]\,\mathbb{E}[G(k',i\omega_n+i\Omega_n)].\end{aligned} \tag{1.32}$$

Setting $k'=-k+K$ and rewriting the momentum sums in terms of k and K, we can see that the $K=0$ sector dominates (where the cooperon has an infrared divergence). Since we are only interested in the most singular part of the quantum correction, we can neglect the K dependence of the Green's functions, thus enabling the k-integral to be evaluated as a contour integral in the complex energy plane as before. In addition, the frequency dependence of the Green's functions can be safely ignored, thereby trivialising the Matsubara summation. The conductivity correction that emerges is, in arbitrary dimension,

$$\Delta\sigma_{ab}(q=0,\omega\to 0)=-\frac{2e^2}{\pi V}\sum_{\boldsymbol{K}}\frac{\delta_{ab}}{K^2}. \tag{1.33}$$

In the case of one, two, and three dimensions, we have

$$\Delta\sigma^{1d}_{ab}=-\frac{e^2}{\pi^2}\delta_{ab}\,(L-l)\qquad\Delta\sigma^{2d}_{ab}=-\frac{e^2}{\pi^2}\delta_{ab}\ln\left(\frac{L}{l}\right)\qquad\Delta\sigma^{3d}_{ab}=-\frac{e^2}{\pi^3}\delta_{ab}\left(\frac{1}{l}\right). \tag{1.34}$$

In 3d, the momentum-space integral has an ultraviolet divergence, which can be controlled by applying a cutoff at $K_{\max}=l^{-1}$, with $l=v_F\tau$ the mean free path. Recall that (1.27) was obtained in the diffusive limit $ql\ll 1$. As a result, the weak localisation correction is small in 3d: $\sigma_{\text{Drude}}/\Delta\sigma^{3d}\approx(k_Fl)^2$. Now, in 1d and 2d the integral has both ultraviolet and infrared divergences, the latter being regulated by a low-momentum cutoff set by the inverse of the length scale of the system L (or the phase coherence length L_ϕ, in the case $L_\phi<L$). At low temperatures (L_ϕ is large) and large system sizes, weak localisation gives rise to a large and negative correction to the conductivity. This is a signature of the result that in low dimensions (d < 3) and at low temperature, metals become insulating for arbitrarily weak disorder.

1.2 Random matrix theory

The analysis of statistical properties of the spectrum has been a staple technique for decades in the study of integrable-chaotic crossovers in single-particle disordered systems, and in recent years has become similarly widespread in the context of MBL. We shall now introduce these methods – the main idea being that the spectral properties of the ergodic phase fall into the universality class of certain ensembles of random matrices – as they will be of use to us in our study of the quantum random energy model and its variants.

Confronted with the complicated, nonintegrable Hamiltonians of heavy nuclei in the 1950s, physicists – led by Wigner and Dyson – were forced to adopt a statistical approach in an attempt to understand the resonance spectra they observed. Assuming particular details of the system to be irrelevant, Wigner made the step of replacing the Hamiltonian by a random (Hermitian) $n \times n$ matrix ensemble in which the matrix elements were independent random variables drawn from some distribution [39]: this marked the first application of random matrix theory (RMT) in physics. The corresponding density of states and nearest-neighbour level spacing distribution that he derived from this assumption in the large-N limit, the celebrated Wigner semicircle and Wigner surmise respectively [40], were extremely successful in capturing the universal properties of nuclear Hamiltonians and have since been found to have widespread applications. Dyson later added mathematical precision by establishing how the symmetry properties of the Hamiltonian, most importantly time-reversal symmetry, had to be encoded in the ensembles, leading to the Wigner-Dyson Gaussian orthogonal (GOE), unitary (GUE), and symplectic (GSE) ensembles [41–43].

Although well motivated, and its success spoke for itself, it was a few decades before a more satisfying explanation emerged for *why* RMT worked. This came in a landmark paper in the field of few-body quantum chaos in which Bohigas, Giannoni, and Schmidt (BGS) conjectured, albeit with only numerical support, that the RMT limit is attained in the spectral statistics of quantum systems whose underlying classical dynamics is chaotic [44]. The BGS conjecture was a natural complement to the earlier conjecture of Berry and Tabor that the eigenvalues of systems whose corresponding classical dynamics are integrable (i.e. nonchaotic) are uncorrelated, that is, they obey Poisson statistics. [45]. Although both conjectures remain without general, rigorous proofs, a great weight of numerical evidence has been amassed together with some analytic results for certain limits. Indeed, spectral statistics quickly became a standard tool in the context of disordered metals to study the insulating (integrable) and metallic (chaotic) phases on either side of the Anderson transition [46, 47] as well as the region of scale-invariant, critical statistics close to the transition [48]. In recent years, analogous diagnostic techniques have been applied to systems exhibiting many-body localisation [49–51]. There is a slight subtlety in the latter case owing to the possibility for a localisation-delocalisation transition to coexist (without coinciding) with a nonergodic-ergodic transition [5], resulting in distinct nonergodic and ergodic metal phases on the delocalised side of the transition [55, 56]. Although signs of the nonergodic metal may be seen in the spectrum, in particular, a deviation from the RMT limit, the more pronounced signature is in fact in the eigenvector statistics, where multifractality is found. We shall say nothing further of the nonergodic metal, which shall not appear in this present work.

---

[5] Whilst such a transition has been shown to occur in random regular graphs [52, 53] and random matrix models [54], it has yet to be definitively demonstrated in a system that undergoes bona fide MBL.

Let us now provide a short précis of results concerning spectral statistics that we shall refer to in later chapters; the results can be found in Refs. [57, 58] together with derivations and further exposition. The models we shall consider are time-reversal invariant and thus the relevant Wigner-Dyson ensemble is the GOE: the ensemble of real, symmetric matrices whose entries are independent identically distributed Gaussians ($H_{ii} \sim N(0,2)$ and $H_{ij} \sim N(0,1)$, with the symmetry constraint $H_{ij} = H_{ji}$). The use of the term 'orthogonal' pertains to the fact that the GOE can also be defined as the unique ensemble of independent-entry $n \times n$ real symmetric (i.e. 'Wigner') matrices whose distribution is invariant under orthogonal conjugation – these conditions uniquely specify (up to normalisation) the Gaussian density $e^{-\frac{1}{2}\operatorname{tr} H^2}$ with respect to the Lebesgue measure $dH = \prod_{i<j} dH_{ij}$ on the space of $n \times n$ real symmetric matrices.

The nearest-neighbour level-spacing distribution, denoted $P(s)$ where s is the level spacing scaled by the mean level spacing $\bar{\delta}$, has the following behaviour for the GOE and for a totally uncorrelated (Poissonian) spectrum

$$P(s) = \begin{cases} e^{-s} & \text{Poisson} \\ \frac{\pi}{2} s e^{-\frac{\pi s^2}{4}} & \text{GOE.} \end{cases} \tag{1.35}$$

$P(s)$ is a measure of short-range (with respect to $\bar{\delta}$) correlations in the spectrum, and its vanishing as $s \to 0$ is an indicator of the property known as level repulsion. This terminology is vividly illustrated by noticing that the joint probability density of the eigenvalues can be written as the partition function of a two-dimensional Coulomb gas in an external potential; the so-called Dyson or log-gas [41, 59].

In order to probe longer-range correlations, one can look at the two-level correlation function (or more accurately, the two-point level-density correlator) $R(s) = \bar{\delta}^2 \,\mathbb{E}\left[\rho(\epsilon + s\bar{\delta})\rho(\epsilon)\right] - 1$ (where the expectation is over the random matrix distribution; averaging over an energy window around ϵ is left implicit) and its Fourier transform, the form factor $K(\tau)$. The form factor has the universal forms

$$K(\tau) = \begin{cases} 1 & \text{Poisson} \\ 2\tau - \tau \ln(1 + 2\tau) & \text{GOE } (\tau < 1) \\ 2 - \tau \ln\left(\frac{2\tau+1}{2\tau-1}\right) & \text{GOE } (\tau \geq 1), \end{cases} \tag{1.36}$$

when the scaled time $\tau = t/t_{\mathrm{H}}$ is introduced. The time t is the Fourier dual to s, and the Heisenberg time $t_{\mathrm{H}} = 2\pi/\bar{\delta}$. The linear growth of the GOE form factor at short times (corresponding to level spacings of many times $\bar{\delta}$) describes what is referred to as spectral rigidity. A second measure of the same property is the number variance $\Sigma^2(n)$, which is the variance in the number of energy levels within an energy window $n\bar{\delta}$ and has the behaviour

$$\Sigma^2(n) = \begin{cases} n & \text{Poisson} \\ \frac{2}{\pi^2}\left(\ln n + \ln 2\pi + \gamma + 1 - \frac{\pi^2}{8}\right) & \text{GOE,} \end{cases} \tag{1.37}$$

where $\gamma \approx 0.577$ is the Euler-Mascheroni constant. The suppression of fluctuations in the number of energy levels as the energy window grows (in the GOE) makes it easier to see why the spectrum is described as more rigid than the Poissonian spectrum.

As well as the Gaussian ensembles, Dyson also defined ensembles of random unitary matrices: the circular ensembles. The group $U(n)$ of $n \times n$ unitary matrices forms a compact Lie group and thus by Haar's theorem possesses a unique translation-invariant measure (Haar measure): $U(n)$ with the Haar measure defines the circular unitary ensemble (CUE). The other two circular ensembles are the orthogonal and symplectic subspaces of $U(n)$ with the measure induced by the Haar measure on $U(n)$; for instance, the COE is generated by the mapping $U \mapsto U^T U$ on Haar unitaries. In Chapter 3, it will be helpful to note that in the large-n limit, the spectral statistics for the GOE that we have quoted above coincide with that of the COE.

Spectral statistics can be used as more than a simple indicator of what phase (localised or ergodic) we are looking at; they can also be sensitive to the onset of weak localisation. Diagrammatic perturbation theory first uncovered the existence of a correction to the correlator $R(s)$ [47], but it took the application of the nonperturbative supersymmetric nonlinear sigma model approach to compute the full oscillatory form of the correction [60, 61]

$$R(s) = \overbrace{1 - \frac{\sin^2(\pi s)}{(\pi s)^2}}^{\text{GOE}} + \frac{4a_d}{s_T^2}\sin^2(\pi s), \tag{1.38}$$

where a_d is a constant depending on dimensionality d and boundary conditions, and s_T is the Thouless energy [6] scaled by $\bar{\delta}$. To find such a correction in a many-body localised system – evidence of 'weak MBL' – was a motivating factor for developing the diagrammatic approach to the quantum random energy model in Chapter 2. Although we don't succeed, in Chapter 3 we at least manage to analytically establish the emergence of the RMT limit in the ergodic phase for a stroboscopic variant of the same model. To arrive at this result, we resorted to the methods developed in the study of semiclassical quantum chaos and quantum graphs, a topic which we briefly review in the next section of the introduction.

Lastly, we introduce extreme value statistics, that we touch on directly in Chapter 5 and indirectly in Chapter 5. Given the expansive nature of the subject, we only point out the results we shall make us of and defer to the literature for details [62, 63]. By extreme values, we mean that rather than looking at properties of the bulk of the spectrum, we shall zoom in and focus on the microscopic structure (i.e. on the scale of $\bar{\delta}$) of the edges of the spectrum. If we denote the maximal eigenvalue (of an $n \times n$ random matrix) $\lambda_{\max}$, then we can define a shifted and rescaled maximal eigenvalue

---

[6] The Thouless energy is the inverse of the time for electrons to diffuse across a system; from a quantum-mechanical point-of-view, more relevant here, it is also the energy scale below which spectral statistics approach the RMT limit.

$$s = \lim_{n\to\infty} \frac{\lambda_{\max} - \sqrt{2n}}{2^{-1/2} n^{-1/6}}, \tag{1.39}$$

whose cumulative distribution function in the case of the GUE is the Tracy-Widom distribution [64, 65] given by the Fredholm determinant $F_2(s) = \det(\mathbb{1} - A_s)$ (similar determinantal formulae for the GOE and GSE also exist [66, 67]), where the Airy kernel on the space $L^2(s, \infty)$ expressed in terms of the Airy function and its first derivative is

$$A_s = \frac{\mathrm{Ai}(x)\,\mathrm{Ai}'(y) - \mathrm{Ai}'(x)\,\mathrm{Ai}(y)}{x - y}. \tag{1.40}$$

Tracy and Widom also showed that this distribution, together with those of the GOE and GSE [66], can be written as an integral over Painlevé transcendents.

On the other hand, the cumulative distribution function of the largest eigenvalue for a Poissonian spectrum is the generalised extreme value distribution [62]

$$G(\lambda_{\max}) = e^{-\left(1+\xi\frac{\lambda_{\max}-\mu}{\sigma}\right)^{-1/\xi}}, \tag{1.41}$$

with parameters ξ, μ, and σ.

1.3 Quantum graphs

As we mentioned in the previous section, the BGS conjecture which is the theoretical motivation for much of the use of spectral statistics remains without proof. A considerable step towards placing it on a firm theoretical foundation has been the use of periodic orbit theory, that began with the work of Berry [68], to show that in the semiclassical limit the form factor of quantum chaotic Hamiltonians exactly matches that of RMT [69]. Being a semiclassical approximation however, its application is only justified in the short-time ($\tau \ll 1$) regime. If we allow ourselves to move to less realistic toy models, then there do exist a class of system for which periodic-orbit expansion for the density of states is exact, thus enabling rigorous proof of the BGS conjecture [70, 71]: quantum graphs [7] (see Refs. [72, 73] for a more thorough introduction than contained here).

The study of quantum graphs is concerned with quantised one-dimensional Schrödinger operators defined on metric graphs. Quantisation, and thus the computation of the spectrum, is most conveniently carried out by way of scattering theory as is done for dynamical billiards for instance [74]; let us now demonstrate this procedure (we follow [72, 75]). Consider a metric graph $G = (V, B)$ consisting of a set of bonds (edges) B, vertices V, and bond lengths L_b for all $b \in B$; an order is defined on V such that the coordinate x_b can be assigned to the bond, with $x_b = 0$ defined to be at the vertex i in a bond $b = (i, j)$ where $i < j$. The solution of the time-independent Schrödinger equation on a given bond can be written as forward and backward propagating plane waves

---

[7] We return to discuss which classes of quantum graph are quantum chaotic in the sense that they show (or are expected to show) RMT statistics in Chapter 3.

$$\psi_b(x_b, k) = a_{b,+1}e^{i(kx_b+A_bx_b)} + a_{b,-1}e^{-i(kx_b-A_bx_b)}, \tag{1.42}$$

for amplitudes $a_{b,\nu}$ where $\nu = \pm 1$ is a direction index, and A_b are magnetic fluxes. Various boundary conditions are employed in the literature, but after making a suitable choice, we obtain an equation

$$\vec{a} = \mathsf{U}\vec{a}, \tag{1.43}$$

where $\vec{a}$ is a $2|B|$-component vector and $\mathsf{U}_B(k)$ a square matrix decomposed as

$$\mathsf{U}_B(k) = T(k)S, \tag{1.44}$$

for diagonal bond propagation matrix $T(k)_{b\nu,b'\nu'} = \delta_{bb'}\delta_{\nu\nu'}e^{i(k+\nu A_b)L_b}$ and scattering matrix S, with nonzero matrix elements $S_{b\nu,b'\nu'}$ whenever the head of the directed bond (b', ν') coincides with the tail of (b, ν), with a value set by the boundary conditions. The evolution operator for m scattering events on the quantum graph is evidently $\mathsf{U}_B(k)^m$; as we shall see in Chapter 3, the Floquet operator for a periodically driven system will play an analogous role to $\mathsf{U}_B(k)$.

We are thus able to write down the spectrum of G in terms of the secular equation

$$\mathrm{spec}(G) = \{\, k_n > 0 \mid \det(\mathbb{1} - \mathsf{U}_B(k)) = 0 \,\}\,. \tag{1.45}$$

Importantly, we can also consider the spectrum of $\mathsf{U}_B(k)$ (at fixed k), or rather its eigenphase spectrum $\{\, \theta_i \,\}$, as it is a unitary operator. In the $|B| \to \infty$ limit and for the case of incommensurate bond lengths that we shall discuss presently, it transpires that correlation functions of k_n and θ_i are equivalent.

When we compute correlators, what is the analogue of disorder-averaging? One option is the incommensurability condition on bond lengths: $\{\, L_b \mid p_b \in \mathbb{Z}, \sum_b p_b L_b = 0 \iff p_b = 0 \ \forall b \,\}$. In this case, the bond propagation matrix is ergodic in the sense that the torus $\mathbb{T}^{|B|}$ is dense in the image of the map $k \mapsto \{\, e^{ikL_b} \,\}$. Hence, it is unsurprising that an ergodic theorem exists: 'time' (i.e. k) averaging and 'phase' averaging (i.e. the phases kL_b appearing in $T(k)$) are equivalent. This fact, together with the correspondence between eigenphase and k_n statistics, implies that the spectra of large-$|B|$ quantum graphs can be considered equivalent to random matrix theory of certain unitary ensembles.

We conclude this subsection on quantum graphs with a brief account of periodic-orbit theory. The density of eigenphases can be written in terms of the periodic Dirac delta function as $\rho(\theta) = \delta_{2\pi}(\theta - \theta_j)$, which upon inserting the Fourier series for the periodic delta function (equivalently thought of as applying the Poisson summation formula) gives

$$\rho(\theta) = \frac{1}{2\pi}\sum_j \sum_{m=-\infty}^{\infty} e^{im(\theta-\theta_j)}. \tag{1.46}$$

Recognising the exponential of the eigenphases as just the eigenvalues of U_B, we can replace the sum over them by a trace

$$\begin{aligned}\rho(\theta) &= \frac{1}{2\pi}\sum_{m=-\infty}^{\infty} \operatorname{tr}\left(\mathsf{U}_B^m\right) e^{im\theta} \\ &= \frac{2|B|}{2\pi} + \frac{1}{\pi}\operatorname{Re}\sum_{m=1}^{\infty} \operatorname{tr}\left(\mathsf{U}_B^m\right) e^{im\theta}. \end{aligned} \tag{1.47}$$

The traces of $\mathsf{U}_B(k)$ can be written as periodic-orbit summations

$$\operatorname{tr}(\mathsf{U}_B(k)^m) = \sum_{p\in\mathcal{P}_m} n_p \mathcal{A}_p^r e^{ir(kL_p+\Phi_p)} \tag{1.48}$$

where $p = \{\beta_1, \dots, \beta_{n_p}\}$ is a primitive periodic orbit (a periodic orbit is a closed trajectory of directed bonds on the graph modulo cyclic permutations; primitive periodic orbits are those which cannot be written as a repetition of a shorter orbit) of length $n_p = |p|$ dividing m; the orbit lengths are $L_p = \sum_{b\in p} L_b$, $\Phi_p = \sum_{b\in p} \nu_b A_b$ is the total magnetic flux through the orbit p, the number of repetitions (of a primitive orbit) is $r = m/n_p$, and the amplitudes are given by $\mathcal{A}_p = \prod_{i=1}^m S_{\beta_i\beta_{i+1}}$ such that $p = \{\beta_i\}$. After inserting (1.48) into the expression for the density of states (1.47), we obtain a trace formula (à la Gutzwiller's semiclassical trace formula in quantum chaos [76]) for quantum graphs.

1.4 Operator spreading

As well as the spectral signatures described above that distinguish many-body quantum chaotic from integrable systems, there has been growing interest in recent years in characterising many-body systems in terms of the quantum information dynamics that they may display. In general, localised quantum information spreads out under unitary dynamics: if one follows the evolution of an initially local operator in the Heisenberg picture, its support in a suitable local operator basis occupies a growing spatial region in time. This process of operator spreading is captured by the behaviour of the out-of-time-order correlation function (OTOC) [77–79]

$$C(x,t) \equiv \frac{1}{2}\langle [O_0(t), O_x(0)]^\dagger [O_0(t), O_x(0)]\rangle, \tag{1.49}$$

where O_x is a local operator at position x, and $O_0(t)$ is initially localised at the origin. Initially, one can see that the commutators will vanish, but as O_0 spreads in space over time it overlaps with $O_x(0)$ giving a nonzero value to the commutators. Since the quantum information encoded in the initial condition is eventually distributed over a large region, inaccessible to local measurements, this process describes so-called scrambling of information; no scrambling is possible in an Anderson localised phase whilst an MBL phase scrambles slowly: the operator radius grows logarithmically ('logarithmic light cone') in time rather than ballistically (i.e. linearly) for the ergodic phase [80–83]. Unsurprisingly, these scrambling results for MBL and chaotic systems are close cousins of the numerically justified lore that entanglement entropy grows logarithmically in time [84] in an MBL phase, rather than ballistically as in generic nonintegrable systems [85].

As well as the interest in OTOCs from the perspective of lattice models, they have also been used as a diagnostic of many-body quantum chaos in the context of certain quantum field theories where OTOCs have been found to exhibit exponential growth [86–88], in the same spirit as the exponential divergence of trajectories set by the Lyapunov exponent (λ_L) in classically chaotic systems [89]. Black holes are expected to be maximally fast scramblers in that they scramble in a time logarithmic in the system size and saturate a conjectured bound (attained in large-N conformal field theories holograpically dual to Einstein gravity) on the coefficient of the logarithm, $t_* = \lambda_L^{-1} \log N^2$, with $\lambda_L = \frac{2\pi}{\beta}$ [86, 90].

The behaviour of OTOCs that is emerging in lattice models with local interactions is that of a ballistic front, propagating at what has been dubbed the butterfly velocity, that broadens diffusively – much of the evidence for this has come from the analysis of discrete-time random unitary circuit models [91–94]. A continuous-time random circuit model, the Brownian coupled cluster model, has been found to interpolate between a Lyapunov regime of exponential growth of the OTOC in the large-N (i.e. large cluster size) limit as seen in large-N quantum field theories, and a diffusively broadening front for finite N [95]. In Chapter 6, we take up this problem and establish operator growth phenomenology in line with that of random circuit models by studying the continuous time evolution of quantum spin models with local interactions in the presence of a classical stochastic field.

Part I

Disordered spins

Chapter 2

Quantum random energy model: a diagrammatic approach

The motivation for this chapter was elaborated in section 1.1: to make analytic progress in the study of MBL by developing a perturbation theory starting from the ergodic side of the transition, in analogy to the theory of weak localisation for a single particle. However, it remains to illustrate why we considered our choice of model, the quantum random energy model (QREM), to be a promising starting point for such an enterprise. The QREM is a mean-field model of a quantum spin glass whose thermodynamic phase diagram, consisting of a first-order transition between a classical random energy model regime and a quantum paramagnetic regime, has been known since the 1990s [96]. In recent years, following a surge of interest in MBL, exact diagonalisation and strong-disorder perturbative approaches have provided convincing evidence of distinct ergodic and localised phases separated by a mobility edge, making the QREM a useful mean-field toy model of the MBL transition [97, 98]. Furthermore, as we shall see shortly, the QREM can be interpreted as an Anderson model on a hypercube: this observation motivates our analogy to the single-particle problem and is therefore our principal reason for selecting the model. In the same way that MBL can be viewed as Anderson localisation in Fock space [14, 55], we sought to identify something akin to weak-localisation on the hypercube – the configuration space of N spin-1/2 objects.

2.1 Model

2.1.1 Hamiltonian and Hilbert space

We will study the quantum random energy model (QREM), a model of N interacting spin-1/2 degrees of freedom with Hamiltonian

$$H = h\sum_{i=1}^{N}\sigma_i^x + \sum_{z\in\mathbb{Z}_2^N}\mathcal{V}(z), \tag{2.1}$$

where $\mathbb{Z}_2^N = \{-1, 1\}^N$, such that $z = \{z_1, \ldots, z_N\}$ with $z_i \in \{1, -1\}$ and[1]

$$\mathcal{V}(z) = V(z) \left|z\right\rangle \left\langle z\right|, \tag{2.2}$$

where $V(z)$ are i.i.d. Gaussian random variables with zero mean and covariance γ_z

$$\mathbb{E}\left[V(z)\right] = 0, \qquad \mathrm{Cov}\left[V(z_1)V(z_2)\right] = \gamma_z \delta_{z_1, z_2}. \tag{2.3}$$

This is a Gaussian white noise disorder model, as is used in the theory of a single particle in a random potential. The notation z reflects the natural bijection between elements of $\mathbb{Z}_2^N$ and the eigenstates $\left|z\right\rangle$ of $\sigma_1^z \ldots \sigma_N^z$, which form a basis for the Hilbert space. If we consider points in $\mathbb{Z}_2^N$ to be the vertices of a graph, and let arbitrary vertices z^A and z^B be connected by an edge if they are separated by unit Hamming distance (i.e. $z_i^A \neq z_i^B$ for exactly one value of i), then the graph is isomorphic to the N-dimensional hypercube. This is the graph structure induced by the Hamiltonian: the transverse-field terms generate nearest-neighbour hopping on the hypercube, meaning that the problem can thus be thought of as the Anderson model on a hypercube. Models of this type have been studied in the context of many-body localisation (MBL) in the recent papers Refs. [97, 98] and also of adiabatic quantum optimisation in Ref. [99]. The analytical MBL results for this model are obtained starting from the localised state, using the forward scattering approximation to develop a perturbation expansion to leading order in the transverse field h; our work is complementary in that we start from the extended state.

To relate this Hamiltonian to a microscopic model, we note in passing that Derrida has established that the p-spin Sherrington-Kirkpatrick model

$$H_{\mathrm{SK}} = \sum_{I=\{i_1, \ldots, i_p\}} J_I \, \sigma_{I_1}^z \ldots \sigma_{I_p}^z, \tag{2.4}$$

tends to a random energy model (REM) in the thermodynamic limit when $p \to \infty$ [100, 101]. The REM, which is the second term in (2.1), is a model defined by 2^N energy levels described by a Gaussian white noise process (i.e. independent and identically distributed Gaussian random variables). The QREM can thus be seen to arise from a generalised Sherington-Kirkpatrick model, containing all possible p-spin interactions (for some large p), in the presence of a transverse field.

We are going to consider the limit where the second term in (2.1), the random potential, is small (in a sense that shall be made more precise) compared to the first, the hopping term. Thus, our starting point for perturbation theory is the eigenbasis of the hopping term. We write these basis states as

$$\left|x\right\rangle = \bigotimes_{i=1}^{N} \left|\sigma^x = x_i\right\rangle_i \tag{2.5}$$

---

[1] We will sometimes use $\mathbb{Z}_2^N$ to denote the (N-fold direct product) of the Abelian group of $\{0, 1\}$ under modulo 2 addition, and sometimes to denote the isomorphic group $\{-1, 1\}$ under multiplication (in fact, the only nontrivial irreducible representation of $\mathbb{Z}_2$).

where $x = \{x_1, \dots x_N\}$, $x_i = \pm 1$, gives the assignment of the eigenvalues of σ_i^x. We denote states in the Hilbert space of the i^{th} spin by $|\dots\rangle_i$, and $|\sigma^a = \pm 1\rangle$ denotes the eigenstates of σ^a ($a = x, y, z$). We can think of $|x\rangle$ as analogous to the plane wave state $|\mathbf{k}\rangle$ in single-particle quantum mechanics. To make this clearer, note that in the z-basis

$$|\sigma^x = \pm 1\rangle = \frac{1}{\sqrt{2}} \left[|\sigma^z = 1\rangle \pm |\sigma^z = -1\rangle \right], \tag{2.6}$$

which is analogous to a plane wave in 1D where the wavevector can take only the values $\{0, \pi\}$. Expressing states in the basis $|x\rangle$ amounts to doing Fourier analysis on the hypercube (see appendix A and Ref. [102] for a more formal development of this idea). A recent work has developed a field-theoretic approach to MBL in random-field XXZ spin chains by similarly approaching the problem as an analogue of Anderson localisation in a high-dimensional configuration space and taking inspiration from the single-particle problem [103]. Their approach, which provides an effective description of the ergodic and MBL phases, differs considerably from ours in that they work in the z-basis and adopt the supersymmetric method of disorder averaging. Although it is already quite clear on the basis of numerics that the localisation behaviour shown by the QREM is distinct from true MBL, their field-theoretic analysis is helpful in explicitly demonstrating that the transition in the QREM appears to lie in the Anderson universality class whilst the MBL transition does not.

2.1.2 Formal structure of the perturbation theory

Our approach is to develop a perturbation theory for the resolvent,

$$R(z) = \frac{1}{z - H} \quad \text{for } z \in \mathbb{C} \setminus \sigma(H), \tag{2.7}$$

where $\sigma(H)$ is the spectrum of the Hamiltonian H. Since the Hamiltonian is Hermitian, $\sigma(H) \subset \mathbb{R}$ and so we are motivated to introduce related objects that are everywhere defined on a real ('energy') domain, the retarded resolvent ('resolvent' will henceforth refer to the retarded resolvent)

$$R(\epsilon) := R(z \to \epsilon + \overbrace{i\delta}^{\delta \to 0^+}) = \frac{1}{\epsilon - H + i\delta}, \tag{2.8}$$

as well as the advanced resolvent $R^\dagger(\epsilon)$. We will later find it helpful to make use of the fact that the retarded resolvent is the Fourier transform of the time-evolution operator, the imaginary infinitesimal assuring the convergence of the inverse transform. On account of the disorder, the resolvent is a random quantity; we will need to average products of resolvents over disorder accordingly in order to extract disorder-averaged quantities, just as in the single-particle problem.

Splitting the Hamiltonian

$$H = \overbrace{h\sum_{i=1}^{N}\sigma_i^x}^{T} + \overbrace{\sum_{Z\in\mathbb{Z}_2^N}\mathcal{V}(z)}^{V}, \tag{2.9}$$

expansion with respect to the 'potential' V yields the usual Born series

$$R(\epsilon) = R^{(0)} + R^{(0)}VR^{(0)} + \ldots, \tag{2.10}$$

where

$$R^{(0)}(\epsilon) = \frac{1}{\epsilon + i\delta - T} \tag{2.11}$$

is the 'bare' resolvent. $R^{(0)}(\epsilon)$ has the spectral representation

$$R^{(0)}(\epsilon) = \sum_{x\in\{-1,1\}^N} \overbrace{\frac{1}{\epsilon + i\delta - h\xi(x)}}^{R^{(0)}(x,\epsilon)} |x\rangle\langle x|, \tag{2.12}$$

where $\xi(x) \equiv \sum_{i=1}^{N} x_i$. As in the single-particle problem, we intend to routinely switch from 'momentum' summations over X to 'energy' summations over ξ, weighted by the appropriate density of states (which turns out to be just a binomial coefficient – see (2.19) below).

2.2 Disorder-averaged perturbation theory

2.2.1 Model of disorder

Since our perturbation theory is formulated in the x-basis, the crucial matrix elements that appear in the diagrammatic expansion are $\widetilde{V}(x_1, x_2) = \langle x_1|V|x_2\rangle$, and are given by

$$\widetilde{V}(x_1,x_2) = \langle x_1|V|x_2\rangle = \sum_z V(z)\langle x_1|z\rangle\langle z|x_2\rangle = \frac{1}{2^{N/2}}\sum_z V(z)\langle z|x_1x_2\rangle := \widetilde{V}(x_1x_2). \tag{2.13}$$

These will then need to be disordered averaged using the result

$$\mathbb{E}[V(x)] = 0, \qquad \mathrm{Cov}[V(x_1)V(x_2)] = \frac{\gamma_z}{2^N}\delta_{x_1,x_2} = \gamma\delta_{x_1,x_2}, \tag{2.14}$$

which follows directly from the z-basis definition given in (2.3); note that we have now dropped the tilde used to identify quantities in the Fourier basis. For consistency with the REM (and also QREM) literature [98, 100], we fix the variance γ_z to be $N/2$ and thus

$$\gamma = 2^{-N}\left(\frac{N}{2}\right)\Gamma^2, \tag{2.15}$$

with the consequence that the relative disorder strength is now set solely by the transverse field strength h (n.b. Γ is a bookkeeping parameter with dimensions of energy; its magnitude can later be set to unity).

Our next task will be to compute expectation values of products of the resolvent, starting with the average of the resolvent itself.

2.2.2 Born approximation

The disorder-averaged resolvent can be expressed in terms of a self-energy operator $\Sigma(\epsilon)$

$$\mathbb{E}\left[R(\epsilon)\right] = \frac{1}{\epsilon - T - \Sigma(\epsilon)}. \tag{2.16}$$

The lowest-order contribution to $\Sigma(\epsilon)$ ('first Born approximation') is once again represented by the first diagram in Figure 1.2 (n.b. in this chapter the diagrams that appear are the same as those in section 1.1.3, with the exception that x replaces k) and given by

$$\Sigma^{(2)}(\epsilon) = \gamma \operatorname{tr}\left[R^{(0)}(\epsilon)\right]. \tag{2.17}$$

Expressing the trace in (2.17) in the $|x\rangle$ basis gives

$$\begin{aligned} \Sigma^{(2)}(\epsilon) &= \sum_{x\in\{-1,1\}^N} \frac{1}{\epsilon - h\xi(x) + i\delta} \\ &= \sum_{\substack{-N\le\xi\le N \\ \xi\equiv N \bmod 2}} \frac{g\left(\xi\right)}{\epsilon - h\xi + i\delta}, \end{aligned} \tag{2.18}$$

where in the second line we have introduced the binomial density of states

$$g\left(\xi\right) = \binom{N}{\frac{1}{2}\left(N-\xi\right)} \xrightarrow{N\to\infty} g(0)e^{-\frac{\xi^2}{2N}}. \tag{2.19}$$

Since $g(\xi)$ is strongly peaked around $\xi(x) = 0$ for large N, we make the approximation of setting the density of states to be a constant equal to its maximum value $g(0)$ [2], which can be evaluated by Stirling's approximation to give the asymptotic form

$$g(0) = \binom{N}{\lfloor N/2\rfloor} \sim \frac{2^{N+\frac{1}{2}}}{\sqrt{\pi N}}. \tag{2.20}$$

Approximating the sum in (2.18) by an integral and invoking the Sokhotski-Plemelj formula, we obtain

$$\operatorname{Im}\left\{\Sigma^{(2)}(\epsilon))\right\} = \frac{-\pi\gamma g(0)}{2h}, \tag{2.21}$$

recalling that the real part can be absorbed by a renormalisation of the energy levels, as for a single particle in a random potential.

---

[2] Elsewhere, we use $g(N/2)$ for the same quantity – this is when we use $x_i \in \{0,1\}$ rather than the $x_i \in \{-1,1\}$ notation that we have used thus far.

Expanding the self-energy to the next order (fourth order in V, or second order in γ), we now additionally have the second and third diagrams in Figure 1.2. We shall now argue, as in the single-particle problem, that the second (uncrossed) diagram exceeds the third (crossed) by a factor that can taken to be large ($k_F l \gg 1$ in the single-particle case).

Both diagrams have three bare resolvents. In the uncrossed diagram, there is a free summation over the momentum of the middle resolvent (say, x_2) together with one further free summation over the remaining two momenta, which are constrained to be equal ($x_1 = x_3$) by momentum conservation. In the third (crossed) diagram, there is a summation over x_1, x_2, x_3 subject to the constraint $x_1 x_2 x_3 = x_0$ (for incoming momentum x_0).

Explicitly, the crossed diagram is

$$\gamma^2 \sum_{\substack{x_1,x_2,x_3 \\ x_1x_2x_3=x_0}} R^{(0)}(x_1)R^{(0)}(x_2)R^{(0)}(x_3). \tag{2.22}$$

What kind of constraint does $x_1x_2x_3 = x_0$ give rise to? Since $R^{(0)}(x_\alpha)$ in (2.22) depends only on $\xi(x_\alpha)$, it is helpful to compute the moment-generating function for $\xi(x_\alpha)$ over all states subject to the constraint. By rewriting the constraint as $x_0x_1x_2x_3 = \mathbb{1}$, we can see that for each site (indexed by $i = 1, \ldots, N$), an even number of x_α^i must be equal to -1 for the constraint to be satisfied. This enables us to directly write down the moment-generating function as

$$\begin{aligned} M_{\xi(x_\alpha)}(\lambda_\alpha) &= \mathcal{N} \sum_{\substack{x_1,x_2,x_3 \\ x_0x_1x_2x_3=\mathbf{1}}} \prod_{\alpha=0}^{3} e^{\lambda_\alpha \xi(x_\alpha)} && (2.23) \\ &= \left(\prod_{\alpha=0}^{3} \left[\frac{e^{-\lambda_\alpha} + e^{\lambda_\alpha}}{2} \right] + \prod_{\alpha=0}^{3} \left[\frac{e^{-\lambda_\alpha} - e^{\lambda_\alpha}}{2} \right] \right)^N, && (2.24) \end{aligned}$$

where $\mathcal{N}$ is the normalisation to ensure $M_{\xi(x_\alpha)}(0) = 1$. Taking the logarithm affords the cumulant-generating function,

$$\begin{aligned} \ln M_{\xi(X_\alpha)}(\lambda_\alpha) &= N \ln \left(\prod_{\alpha=0}^{3} \left[\frac{e^{-\lambda_\alpha} + e^{\lambda_\alpha}}{2} \right] + \prod_{\alpha=0}^{3} \left[\frac{e^{-\lambda_\alpha} - e^{\lambda_\alpha}}{2} \right] \right) && (2.25) \\ &= \sum_\alpha \lambda_\alpha \kappa_\alpha + \sum_{\alpha,\beta} \frac{1}{2!} \lambda_\alpha \lambda_\beta \kappa_{\alpha\beta} + \ldots, \end{aligned}$$

where in the second line we have simply written down the general form of a cumulant expansion, with the n^{th} cumulant denoted $\kappa_{\alpha_1 \ldots \alpha_n}$. If we consider the affine transformation

$$\tilde{\xi}(x_\alpha) = \frac{\xi(x_\alpha) - \mathbb{E}[\xi(x_\alpha)]}{\mathrm{Var}[\xi(x_\alpha)]}, \tag{2.26}$$

then the n^{th} cumulants of x_α transform according to

$$\tilde{\kappa}_{\alpha_1\ldots\alpha_n} = \prod_{i=1}^{n} \frac{1}{\sqrt{\mathrm{Var}[\xi(x_{\alpha_i})]}} \kappa_{\alpha_1\ldots\alpha_n}. \tag{2.27}$$

Now, (2.25) indicates that all the cumulants of $\xi(x_\alpha)$ are of order N, and therefore $\tilde{\kappa}_{\alpha_1\ldots\alpha_n}$ are of order $N^{1-\frac{n}{2}}$. We conclude that in the large-N limit the distribution $\tilde{\xi}(x_\alpha)$ is well-approximated by its first two cumulants (i.e. $\tilde{\xi}(x_\alpha)$ tends to a multivariate Gaussian), and consequently, so is $\xi(x_\alpha)$, being related to $\tilde{\xi}(x_\alpha)$ by an affine transformation.

Expanding the cumulant-generating function in (2.25) to second order in λ_α

$$N^{-1} \ln M_{\xi(X_\alpha)}(\lambda_\alpha) = \ln\left(\prod_\alpha \cosh\lambda_\alpha\right) + \ln\left(1 + \prod_\alpha \tanh\lambda_\alpha\right) \tag{2.28}$$

$$= \sum_\alpha \frac{1}{2!}\lambda_\alpha^2 + O(\lambda^4), \tag{2.29}$$

reveals that $\mathbb{E}[\xi(x_\alpha)] = 0$ and $\mathrm{Cov}[\xi(x_\alpha), \xi(x_\beta)] = N\delta_{\alpha\beta}$, and so we have established the key result that the distributions of the four energies $\xi(x_\alpha)$ ($\alpha = 0, 1, 2, 3$) are independent Gaussians in the limit of large N. We note that the proof we have presented of this result is of the same spirit as the proofs of central limit theorems using the method of moment-generating functions (or more generally, the method of characteristic functions, to handle the scenario when some moments are not well defined), and its various special cases, such as the de Moivre–Laplace theorem [104].

Using this result, we can compute the ratio of the imaginary parts of the crossed to the uncrossed self-energy diagram at second order

$$r = \frac{\Sigma_C}{\Sigma_{UC}} = \frac{2^{-N}\,\mathrm{Im}\left[\gamma^2 \sum_{x_1,x_2,x_3} R^{(0)}(x_1)R^{(0)}(x_2)R^{(0)}(x_3)\right]}{\mathrm{Im}\left[\gamma^2 \sum_{x_1,x_2} \left(R^{(0)}(x_1)\right)^2 R^{(0)}(x_2)\right]}. \tag{2.30}$$

A normalisation factor of 2^{-N} has been inserted into the numerator because the number of terms in the sum is still 2^{2N}, due to the constraint, even though the distributions for $\xi(x_1)$, $\xi(x_2)$ and $\xi(x_3)$ are independent for large N. The momentum summations can be converted to energy integrals and then evaluated by approximating the binomial density of states as a Gaussian; the basic results we require are firstly the Stieltjes transform of the Gaussian

$$\sum_x R^{(0)}(x) = g(0)\int_{-\infty}^{\infty} \frac{d\xi}{2h}\, \frac{e^{-\frac{\xi^2}{2Nh^2}}}{\epsilon - \xi + i\delta} = \frac{1}{2\tau\gamma}\left(\frac{2}{\sqrt{\pi}}F(y) - ie^{-y^2}\right), \tag{2.31}$$

where $y := \frac{\epsilon}{h\sqrt{2N}}$ and $F(y)$ is the Dawson function, and also

$$\sum_x \left(R^{(0)}(x)\right)^2 = g(0)\int_{-\infty}^{\infty} \frac{d\xi}{2h}\, \frac{e^{-\frac{\xi^2}{2Nh^2}}}{(\epsilon-\xi+i\delta)^2} \tag{2.32}$$

$$= \frac{1}{2\tau\gamma}\frac{1}{h\sqrt{2N}}\left(-\frac{2}{\sqrt{\pi}} + y[-ie^{-y^2} + \frac{2}{\sqrt{\pi}}F(y)]\right). \tag{2.33}$$

The parameter $\tau = \frac{h}{\pi g(0)\gamma}$ is discussed in the next section and we have used the Gaussian approximation to the binomial distribution given in (2.19). These results can now be used to calculate the ratio in (2.30)

$$r(y) = \frac{\sqrt{\pi}}{2h^2N}\left(\frac{\frac{6}{\sqrt{\pi}}F(y)^2 - \frac{\sqrt{\pi}}{2}e^{-2y^2}}{2yF(y)-1}\right). \tag{2.34}$$

Since $r(y) \sim O(N^{-1})$, we can neglect the crossed diagrams in the self-energy in the large-N limit.

2.2.3 Self-consistent Born approximation

Having justified the noncrossing approximation for the self-energy, we are able to evaluate it in the self-consistent Born approximation as in the single-particle case: the uncrossed self-energy diagrams ('rainbow diagrams') can be summed to infinite order by replacing the bare resolvent in the leftmost diagram of Figure 1.2 with a dressed resolvent and then solving self-consistently for the self-energy,

$$\Sigma_{\text{SCBA}}(\epsilon) = \gamma\sum_{\xi}\frac{g\,(\xi)}{\epsilon - h\xi - \Sigma_{\text{SCBA}}(\epsilon)}. \tag{2.35}$$

It is clear that if we make the ansatz of replacing $\Sigma_{\text{SCBA}}(\epsilon)$ on the right-hand side by $\Sigma^{(2)}(\epsilon)$ computed in (2.18), then self-consistency is achieved provided that the magnitude of $\text{Im}\left\{\Sigma^{(2)}(\epsilon))\right\}$ is small (relative to the bandwidth $h\sqrt{N}$). This motivates us to parameterise the self-energy such that this is more transparent

$$\text{Im}\,\Sigma_{\text{SCBA}}(\epsilon) = \frac{-\pi\gamma g(0)}{2h} = -\frac{1}{2\tau}, \tag{2.36}$$

which is the familiar form of the self-energy in the single-particle theory. Inserting the definition of γ, the parameter τ is therefore given by

$$\tau = \frac{h\sqrt{2}}{\Gamma^2\sqrt{\pi N}} \tag{2.37}$$

Demanding that the Born self-energy is small (such that it also solves the self-consistent equation) identifies an appropriate weak disorder limit,

$$\frac{1}{\tau} \ll h\sqrt{N} \implies h^2\Gamma^{-2}\sqrt{\frac{2}{\pi}} \gg 1. \tag{2.38}$$

2.2.4 Diffusion ladder

We now move on to consider diffusion, which demands the consideration of two-particle quantities. The probability for the system to propagate between vertices $z_\mathrm{i}, z_\mathrm{f} \in \mathbb{Z}_2^N$ is given by

$$P(z_\mathrm{f}, z_\mathrm{i}; t) = |\langle z_\mathrm{f}|U(t)|z_\mathrm{i}\rangle|^2, \tag{2.39}$$

where $U(t) = \exp(-iHt)$ is the time-evolution operator. As previously mentioned, this can be expressed as the Fourier transform of the resolvent

$$U(t) = \int \frac{d\epsilon}{2\pi i} R(\epsilon)e^{-i\epsilon t}, \tag{2.40}$$

which one can also interpret as a consequence of the generalisation of Cauchy's integral formula to holomorphic functional calculus. Inserting this definition into (2.39) and averaging gives

$$\mathbb{E}\left[P(z_\mathrm{f}, z_\mathrm{i}; t)\right] = \int \frac{d\epsilon_1}{2\pi}\frac{d\epsilon_2}{2\pi}\,\mathbb{E}\left[\langle z_\mathrm{f}|R(\epsilon_1)|z_\mathrm{i}\rangle\langle z_\mathrm{i}|R^\dagger(\epsilon_2)|z_\mathrm{f}\rangle\right]e^{-i(\epsilon_1-\epsilon_2)t}. \tag{2.41}$$

The long-time (low-frequency) behaviour will be determined by the contribution with close energy arguments, as can be seen by taking the Fourier transform with respect to time

$$\mathbb{E}\left[P(z_\mathrm{f}, z_\mathrm{i}; \omega)\right] = \int \frac{d\epsilon}{2\pi}\,\mathbb{E}\left[\langle z_\mathrm{f}|R(\epsilon+\omega)|z_\mathrm{i}\rangle\langle z_\mathrm{i}|R^\dagger(\epsilon)|z_\mathrm{f}\rangle\right]. \tag{2.42}$$

As in the single-particle case, translational invariance is restored by the average, making it convenient to work in the Fourier (i.e. $|x\rangle$) basis.

As we did in section 1.1.3, we can proceed to calculate the diffuson

$$\mathcal{D}(x_q, \omega) = \frac{\gamma}{1 - \gamma\sum_x R(x, \epsilon+\omega)R^\dagger(xx_q, \epsilon)}, \tag{2.43}$$

where $x_q = x_{i'}x_f = x_{f'}x_i$ is the fixed 'momentum' flow through the diffusion ladder (product of the momenta of the resolvents between adjacent rungs of the ladder). Note that $R(x,\epsilon)$ here denotes the SCBA resolvent, $\mathbb{E}[R(x,\epsilon)]$, and not the full resolvent that appears in (2.42); it shall henceforth be clear which we mean from the context. We must first compute the pair-bubble in the denominator

$$\pi(x_q, \epsilon, \omega) = \gamma\sum_x\left(\frac{1}{\epsilon+\omega-h\xi(x)+\frac{i}{2\tau}}\right)\left(\frac{1}{\epsilon-h\xi(xx_q)-\frac{i}{2\tau}}\right). \tag{2.44}$$

Let $N^{\pm}$ be the numbers of up (+1) and down (-1) spins in x, and let F^{+} (F^{-}) be the number of down spins in x_q for which the corresponding spin in x is up (down). Then (2.44) may be written

$$\begin{aligned}\pi(x_q,\epsilon,\omega) = \gamma \sum_{\substack{N^{+}+N^{-}=N\\ F^{+}+F^{-}=F}} &\frac{F!}{F^{+}!F^{-}!}\frac{(N-F)!}{(N^{+}-F^{+})!(N^{-}-F^{-})!}\\ &\times\left(\frac{1}{\epsilon+\omega-h(N^{+}-N^{-})+\frac{i}{2\tau}}\right)\left(\frac{1}{\epsilon-h(N^{+}-N^{-}+2[F^{-}-F^{+}])-\frac{i}{2\tau}}\right).\end{aligned} \tag{2.45}$$

Here $\xi(x_q) = N - 2F$, and we shall be interested in F small ($1 \ll F \ll N$).

In the large-N limit we are justified in making the Gaussian approximation to the binomial distribution,

$$\frac{(N-F)!}{(N^{+}-F^{+})!(N^{-}-F^{-})!} \approx \frac{2^{(N-F)}}{\sqrt{\pi(N-F)/2}}\exp\left(-\frac{(N^{+}-N^{-}-F^{+}+F^{-})^2}{2(N-F)}\right). \tag{2.46}$$

For large N we can shift the region of integration over $n = N^{+} - N^{-}$ by $f = F^{+} - F^{-}$ without altering the limits of the integral, giving

$$\begin{aligned}\pi(x_q,\epsilon,\omega) =& \frac{\gamma 2^{(N-F+\frac{1}{2})}}{\sqrt{\pi(N-F)}}\int_{-F}^{F}\frac{df}{2}\int_{-\infty}^{\infty}\frac{dn}{2}\frac{F!}{F^{+}!F^{-}!}\exp\left(-\frac{n^2}{2(N-F)}\right)\\ &\times\left(\frac{1}{\epsilon+\omega-h(n+f)+\frac{i}{2\tau}}\right)\left(\frac{1}{\epsilon-h(n-f)-\frac{i}{2\tau}}\right).\end{aligned} \tag{2.47}$$

Taking the Gaussian density of states as constant, in the large-N limit when it is very broad ($\sigma \approx \sqrt{N-F}$) on the scale of the decay of the resolvents, the n integral in (2.47) can be evaluated using the residue theorem

$$\pi(x_q,\epsilon,\omega) = 2^{-F-2}\int_{-F}^{F} df\,\frac{F!}{F^{+}!F^{-}!}\left(\frac{1}{\omega\tau-2hf\tau+i}\right), \tag{2.48}$$

where we have used the definition of τ in (2.37) and also noted that $\frac{2^{N+\frac{1}{2}}}{\sqrt{\pi(N-F)}} \approx g(0)$. Replacing the binomial coefficient with its large-F Gaussian approximation (the integral approximation to the f summation demands $F \gg 1$), and also expanding the residue to second order in $hf\tau$ (we have imposed the small-F condition $h\sqrt{F}\tau \ll 1$), we find

$$\pi(X_q,\epsilon,\omega) = 1 + i\omega\tau - 4h^2\tau^2F, \tag{2.49}$$

which upon insertion into (2.43) gives us the form of the diffuson

$$\mathcal{D}(F,\omega) = \frac{\gamma}{(DF-i\omega)\,\tau}, \tag{2.50}$$

where the diffusion constant has been defined as $D = 4h^2\tau$. It is worth clarifying the hierarchy of approximations that restricts the value of F to show that a diffusive regime may exist and that our small- and large-F approximations are compatible:

$$1 \overset{\sum_f \to \int_f}{\ll} F \overset{\text{diffusive}}{\ll} \left(\frac{1}{h\tau}\right)^2 \overset{\substack{\text{weak}\\ \text{disorder}}}{\ll} N. \tag{2.51}$$

The form of the diffuson in (2.50) is consistent with what we would expect for classical diffusion on a hypercube; in the next section (2.2.5), we illustrate this by considering a random walk on $\mathbb{Z}_2^N$. Firstly, we show that the Fourier transform (x-basis representation) of the Laplacian is proportional to F (recalling that $\xi(x) = N - 2F$), and secondly that the evolution from the initial to the stationary distribution takes the form of a sharp transition – this is known as the cutoff phenomenon and we shall give a precise description of it below [105, 106]. We can interpret the latter observation in terms of a thermalisation time: if the initial state has its weight localised at a single vertex, it remains concentrated there until a transition time at which the system's state vector suddenly becomes distributed over the whole hypercube. 'Diffusion' on the hypercube is therefore associated with this rather pathological behaviour, as opposed to the more gradual spreading out we come to associate with diffusive processes.

2.2.5 Classical diffusion on the hypercube

The Laplacian of a simple graph can be defined as

$$\Delta = \mathbb{1} - d^{-1}\mathrm{A}, \tag{2.52}$$

where d and A are the degree and adjacency matrices respectively. The particular normalisation, known as random walk normalisation, is chosen such that the Laplacian coincides with the transition rate matrix of a random walk (other choices are possible, but the cutoff phenomenon that we find is universal). Specialising to the hypercube graph we have

$$\Delta = \mathbb{1} - N^{-1} \sum_i \sigma_i^x. \tag{2.53}$$

We can also introduce the diffusion operator $d(t) = e^{-t\Delta}$, together with its spectral representation

$$d(t) = \sum_x e^{-\mathcal{E}_x t} \left|x\right\rangle \left\langle x\right|, \tag{2.54}$$

with $\mathcal{E}_x = 1 - N^{-1}\xi(x)$. We endeavour to analyse diffusion probabilities between vertices of the hypercube, and so compute the matrix elements of the diffusion kernel

$$d(z', z''; t) = \sum_x e^{-\mathcal{E}_x t} \langle z'|x\rangle \langle x|z''\rangle = \frac{1}{2^{N/2}} \sum_x e^{-\mathcal{E}_x t} \langle x|z'z''\rangle \tag{2.55}$$

$$d(z = z'z''; t) = \frac{1}{2^{N/2}} \sum_x e^{-2\mathcal{F}(x)t} \langle x|z\rangle, \tag{2.56}$$

where $\mathcal{F}(x)$ is the normalised Hamming distance $(F(x)/N)$ between x and $x' = \mathbb{1}$. Inserting the form of the matrix element $\langle x|z\rangle$

$$d(z = z'z''; t) = \frac{1}{2^N} \sum_x \prod_i \left(1 - \frac{1}{2}(1 - x_i)(1 - z_i)\right) e^{-2\mathcal{F}(x)}, \tag{2.57}$$

we note that the x-summation factorises into a product over x_i sums

$$d(z = z'z''; t) = e^{-t} \prod_{i|z_i=1} \sum_{x_i=\pm 1} e^{\frac{x_i t}{N}} \prod_{i|z_i=-1} \sum_{x_i=\pm 1} x_i e^{\frac{x_i t}{N}}, \tag{2.58}$$

thus giving

$$d(z = z'z''; t) = e^{-t} \cosh\left(\frac{t}{N}\right)^N \tanh\left(\frac{t}{N}\right)^{F(z)}. \tag{2.59}$$

Where the F-dependence at long times is set by

$$\tanh\left(\frac{t}{N}\right)^{F(z)} \approx e^{-2F(z)e^{-\frac{2t}{N}}}. \tag{2.60}$$

By setting $F = 0$, we also obtain the exact form of the diagonal part of the diffusion kernel

$$d(z, z; t) = e^{-t} \cosh\left(\frac{t}{N}\right)^N. \tag{2.61}$$

Now, the cutoff phenomenon we mentioned earlier refers to the following behaviour of the total variation distance $D(t) = \sup_{S \subset \mathbb{Z}_2^N} ||P(S; t) - \pi(S)||$ between the probability distribution $P(z, t)$ of a Markov chain and its stationary distribution $\pi(z)$

$$\lim_{c\to\infty} \lim_{N\to\infty} D(t^{(N)}_{\text{mix}} - c w_N) \to 1 \tag{2.62}$$

$$\lim_{c\to\infty} \lim_{N\to\infty} D(t^{(N)}_{\text{mix}} + c w_N) \to 0, \tag{2.63}$$

where w_N is some N-dependent window function. In words, the cutoff phenomenon is describing a situation in which the convergence of a Markov chain to its stationary distribution takes place entirely within a window of width $\sim w_N$ around the mixing time t_{mix}.

Let us begin with a rough calculation of the mixing time. The total variation distance can be written as an L^1 norm and upper bounded according to

$$D(t) = \frac{1}{2}\sum_z |d(z_0, z; t) - 2^{-N}| < \frac{1}{2} \times 2^N |d(z, z; t) - 2^{-N}|, \tag{2.64}$$

where we have inserted the uniform distribution corresponding to the stationary distribution of the process. The term inside the modulus can be evaluated using (2.61)

$$d(z, z; t) - 2^{-N} = 2^{-N}\left[\left(1 + e^{-\frac{2t}{N}}\right)^N - 1\right] \approx 2^{-N} N e^{-\frac{2t}{N}}, \tag{2.65}$$

and substituted into the right-hand side of (2.64) to give

$$D(t) \approx \frac{1}{2} N e^{-\frac{2t}{N}}, \tag{2.66}$$

thus implying a mixing time scaling as

$$t_{\text{mix}} \sim \frac{1}{2} N \ln N, \tag{2.67}$$

which is the correct N-dependence but is larger than the exact result by a factor of 2. However, we have all we need for a precise calculation, which for completeness we shall present here (following the analysis of Diaconis et al. [105]). We can explicitly express the required supremum in the definition of the total variation distance as

$$\begin{aligned} D(t) &= \sum_{z|d(z_0;z)>2^{-N}} \left(d(z_0, z; t) - 2^{-N}\right) && (2.68)\\ &= \sum_{F<F_*} \binom{N}{F} \left(e^{-t}\cosh\left(\frac{t}{N}\right)^{N-F} \sinh\left(\frac{t}{2}\right)^F - 2^{-N}\right) && (2.69)\\ &= \sum_{F<F_*} 2^{-N}\binom{N}{F}\left[\left(1 + e^{-2t/N}\right)^{N-F}\left(1 - e^{-2t/N}\right)^F - 1\right], && (2.70)\end{aligned}$$

where $d(z_0, z; t) > 2^{-N}$ implies $\xi(zz_0) = F < F_*$, and we have used the result (2.59) in the second line. The last line can be written in terms of cumulative probabilities

$$D(t) = P\left(X \le \lfloor F_* \rfloor\right) - P\left(Y \le \lfloor F_* \rfloor\right), \tag{2.71}$$

where $X \sim \text{Bin}(N, (1 - e^{-2t/N})/2)$ and $Y \sim \text{Bin}(N, \frac{1}{2})$. In the large-$N$ limit, we can use the Gaussian approximation to the binomial. To find F_*, we can straightforwardly solve $d(z_0, z; t) = 2^{-N}$ to obtain

$$F_* = N\ln(1 + e^{-2t/N})\left[\ln\left(\frac{1 + e^{-2t/N}}{1 - e^{-2t/N}}\right)\right]^{-1} \sim \frac{N}{2}\left(1 - \frac{1}{2}e^{-2t/N}\right). \tag{2.72}$$

If we now parameterise time in terms of a window around the mixing time as $t = \alpha N \ln N + \beta N$, the final result can be expressed in terms of the cumulative distribution function of the standard normal distribution $\Phi(z) = (2\pi)^{-1/2}\int_{-\infty}^{z} e^{-\frac{x^2}{2}}\, dx = (1/2)\left(1 + \operatorname{erf}\left(z/\sqrt{2}\right)\right)$

$$D(\alpha,\beta) \sim \Phi(\frac{1}{2}N^{\frac{1}{2}-2\alpha}e^{-2\beta}) - \Phi(-\frac{1}{2}N^{\frac{1}{2}-2\alpha}e^{-2\beta}) = 2\Phi(\frac{1}{2}N^{\frac{1}{2}-2\alpha}e^{-2\beta}) - 1. \tag{2.73}$$

It is now clear that we have a cutoff phenomenon (within a window of size N) occuring around the mixing time $t_{\mathrm{mix}} \sim \frac{1}{4}N\ln N$ (i.e. $\alpha = 1/4$) and with a functional form given by the error function

$$D(\beta) = \operatorname{erf}\left(\frac{e^{-2\beta}}{2\sqrt{2}}\right) + \mathcal{O}(1). \tag{2.74}$$

2.3 Transverse spin-spin correlations

If we were to continue in analogy to the single-particle calculations, the naive next step would be to compute the cooperon ladder, in search of a weak-localisation correction. However, there are two obstacles to contend with: firstly, we need to check whether the two-particle crossed diagrams are parametrically smaller than the uncrossed diagrams of the same order, and secondly, we need to consider whether Hikami boxes are required. We begin by considering the latter, more subtle point. In the single-particle calculation, the cooperon can be simply inserted with impunity into the conductivity bubble to compute the weak-localisation correction – this is due to the fact that for isotropic scattering (as is the case for the white noise disorder model), the ladder diagrams vanish (for $q \to 0$; the uniform part of the conductivity). When the ladder diagrams do not vanish, it is necessary to connect diffuson modes to the cooperon through Hikami boxes [4, 107]; a complication we shall attempt to avoid. We are therefore motivated to introduce the analogous observable, one in which a 'momentum' factor appears in the vertices of the bubble, in the hope that the ladder diagrams will vanish in this case too.

The aforementioned observable is the infinite-temperature transverse spin-spin correlator (for total transverse spin $\sigma_{\mathrm{tot}} = \sum_i \sigma_i^x$)

$$C^x(t) = 2^{-N}\langle\sigma^x_{\mathrm{tot}}(t)\sigma^x_{\mathrm{tot}}(0)\rangle = 2^{-N}\sum_{i,j}\operatorname{tr}(\sigma_i^x(t)\sigma_j^x(0)) \tag{2.75}$$

$$= 2^{-N}\sum_{i,j}\int\frac{d\epsilon_1}{2\pi}\frac{d\epsilon_2}{2\pi}\ \operatorname{tr}\left(R^\dagger(\epsilon_1)\sigma_i^x R(\epsilon_2)\sigma_j^x\right)e^{-i(\epsilon_1-\epsilon_2)t}. \tag{2.76}$$

After taking the temporal Fourier transform and disorder averaging we obtain

$$\mathbb{E}[C^x(\omega)] = 2^{-N}\sum_{i,j}\int\frac{d\epsilon}{2\pi}\sum_x \mathbb{E}\left[\langle x|R^\dagger(\epsilon)\sigma_i^x R(\epsilon+\omega)\sigma_j^x|x\rangle\right], \tag{2.77}$$

which is a quantity whose diagrammatic structure is analogous to conductivity, in particular the counterpart of the factors of momentum in the current vertex in (1.20) are factors of x_i (eigenvalues of σ_i^x).

2.3.1 Drude peak

The bare bubble corresponds to the clean limit when the Hamiltonian reduces to solely a transverse field; this can be dealt with explicitly in the Heisenberg picture because all operators are diagonal in the x-basis

$$\begin{aligned} C^x(\omega;\gamma\to 0) &= 2^{-N}\int dt\, e^{i\omega t}\sum_{i,j}\sum_x \langle x|e^{iHt}\sigma_i^x e^{-iHt}\sigma_j^x|x\rangle \\ &= 2^{-N}\delta(\omega)\sum_{i,j}\sum_x x_i x_j = 2^{-N}\delta(\omega)\sum_i\sum_x x_i^2 \\ &= N\delta(\omega). \end{aligned} \tag{2.78}$$

This describes a 'Drude peak'; all the spectral weight (given by (2.78)) is concentrated at zero frequency. Switching on the disorder broadens the delta-function as the disorder term (off-diagonal in the x-basis) will induce relaxation of the transverse spin components.

To see this, one can compute the averaged two-particle bubble in the presence of disorder, which is just a minor modification of the case above

$$\mathbb{E}[C^x(\omega)] = 2^{-N}\sum_{i,j}\int\frac{d\epsilon}{2\pi}\sum_x\left(\frac{x_i}{\epsilon - h\xi(x) - \frac{i}{2\tau}}\right)\left(\frac{x_j}{\epsilon+\omega-h\xi(x)+\frac{i}{2\tau}}\right), \tag{2.79}$$

the only difference is that a finite (as opposed to infinitesimal) imaginary part appears in the resolvent denominators, since they now account for disorder averaging (through the SCBA). We can evaluate the integral over ϵ as a contour integral: if we choose a semicircular contour in the complex-ϵ plane, closed in either the upper or lower half-plane, the integral over the semicircular arc vanishes by the estimation lemma, thence the result follows from the residue theorem

$$\mathbb{E}[C^x(\omega)] = \left(\frac{i\omega+\tau^{-1}}{\omega^2+\frac{1}{\tau^2}}\right)2^{-N}\sum_{i,j}\sum_x x_i x_j. \tag{2.80}$$

$$= \frac{N}{-i\omega+\tau^{-1}} \tag{2.81}$$

We can see from this that in the low-frequency limit the only consequence is to replace the Dirac delta by a Lorentzian whose full-width at half-maximum is controlled by the scattering rate τ^{-1}.

2.3.2 Schwinger time

We now need to compute the ladder diagrams, to ascertain whether or not they vanish. Unfortunately, the integrals can no longer be evaluated by contour methods: if the integration over ϵ is performed first, the ξ-integrals diverge; if we try to integrate over ξ first, we find that we cannot invoke the residue theorem because the integrand decays too slowly with $|\xi|$.

One way to circumvent this difficulty is to move into the time domain: or in the high-energy theorists' language, the Schwinger proper-time representation. This technique is not convenient for resumming infinite subsets of diagrams, but it will enable us to check whether a given ladder diagram vanishes, and also to compare the magnitude of the crossed and uncrossed two-particle diagrams at a given order.

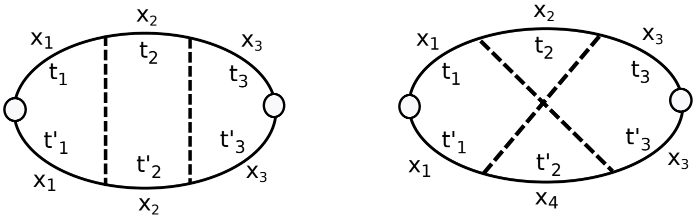

FIGURE 2.1: (Left) Ladder diagram of order γ^2 and (right) the crossed diagram of the same order; the crossed diagram also has the additional momentum constraint $x_1x_2x_3x_4 = \mathbb{1}$, but we can neglect it at large N due to the argument in section 2.2.2.

Beginning with the two-line (order γ^2) ladder (left figure in Fig. 2.1), we find

$$\begin{aligned}\mathbb{E}[C^x_{\text{Ladder, 2}}(\omega=0)] = \frac{\gamma^2}{2^N}\int_{-\infty}^{\infty}\frac{d\epsilon}{2\pi}\int_0^{\infty}\prod_{i=1}^{3}dt_idt'_i\sum_{\{x_k\}}\sum_{i,j} x_1^ix_3^j\, e^{i\epsilon(t_1+t_2+t_3-t'_1-t'_2-t'_2)} \\ \times R(x_1,t_1)R^\dagger(x_1,t'_1)R(x_2,t_2)R^\dagger(x_2,t'_2)R(x_3,t_3)R^\dagger(x_3,t'_3),\end{aligned} \tag{2.82}$$

where $t_i > 0$ and

$$R(x,t) = -ie^{-(ih\xi(X)+\frac{1}{2\tau})t}, \tag{2.83}$$

such that after integrating over ϵ we have

$$\begin{aligned}\mathbb{E}[C^x_{\text{Ladder, 2}}(\omega=0)] = \frac{\gamma^2}{2^N}\int_0^{\infty}\prod_{i=1}^{3}dt_idt'_i\ \delta(t_1+t_2+t_3-t'_3-t'_2-t'_1) \\ \times\sum_{\{x_k\}}\sum_{i,j}x_1^ix_3^j\ e^{ih(\xi(x_1)(t'_1-t_1)+\xi(x_2)(t'_2-t_2)+\xi(x_3)(t'_3-t_3))}e^{-\frac{1}{2\tau}(t_1+t_2+t_3+t'_3+t'_2+t'_1)}.\end{aligned} \tag{2.84}$$

We now note that the momentum-dependent part of the integrand is related to the moment-generating function (for the distribution of $\xi(x_i)$ subject to the constraint $\prod_i x_i = \mathbb{1}$) that we introduced in (2.23); in particular, if we replace the time argument coupled to $\xi(x_i)$ by dummy variables λ_i, the momentum vertices can be generated by differentiation as follows

$$\mathbb{E}[C^x_{\text{Ladder, 2}}(\omega=0)] = -\frac{\gamma^2}{2^N}\int_0^{\infty}\prod_{i=1}^{3}dt_idt'_i\ \delta(t_1+t_2+t_3-t'_3-t'_2-t'_1)\frac{\partial^2\phi(\vec{\lambda})}{\partial\lambda_1\partial\lambda_3}\Big|_{\vec{\lambda}\to\vec{t}}e^{-\frac{1}{2\tau}\sum_{i=1}^{3}t_i+t'_i}, \tag{2.85}$$

where we have defined the characteristic function $\phi(\vec{\lambda}) = M_{\xi(x_\alpha)}(i\vec{\lambda})$ by analytic continuation of the moment-generating function, and

$$\lambda_1 = h(t_1' - t_1), \qquad \lambda_2 = h(t_2' - t_2), \quad \text{and} \quad \lambda_3 = h(t_3' - t_3). \tag{2.86}$$

Inserting the large-N form for the characteristic function (cf. (2.28)), that is, a product of independent Gaussians

$$\phi(\vec{\lambda}) = 2^{3N} e^{-N \sum_i \frac{1}{2}\lambda_i^2}, \tag{2.87}$$

where the normalisation $\phi(\vec{\lambda} = \mathbf{0}) = 2^{3N}$ arises from the fact that there are 2^{3N} terms in the sum over x_i, and recalling that $\gamma = 2^{-N}(N/2)$ we arrive at

$$\begin{aligned} \mathbb{E}[C^x_{\text{Ladder, 2}}(\omega)] = -\frac{1}{4}h^2N^4 \int_{-\infty}^{\infty} \frac{d\epsilon}{2\pi} \int_0^{\infty} \prod_{i=1}^{3} dt_i dt_i' \, e^{i\epsilon \sum_{j=1}^3 \left(t_j - t_j'\right)} e^{i\frac{\omega}{2} \sum_{j=1}^3 \left(t_j + t_j'\right)} \\ \times (t_1 - t_1')(t_3 - t_3') e^{\frac{Nh^2}{2} \sum_{j=1}^3 \left(t_j - t_j'\right)^2} e^{-\frac{1}{2\tau} \sum_{j=1}^3 \left(t_j + t_j'\right)}, \end{aligned} \tag{2.88}$$

which after changing variables to the sum and difference variables $T_j = t_j + t_j'$ and $\bar{t}_j = t_j - t_j'$ can be written

$$-\frac{1}{4}h^2N^4\mathcal{J} \int_{-\infty}^{\infty} \frac{d\epsilon}{2\pi} \int_{-\infty}^{\infty} \prod_{i=1}^{3} d\bar{t}_i \int_{|\bar{t}_i|}^{\infty} \prod_{i=1}^{3} dT_i \; \bar{t}_1 \bar{t}_3 \, e^{-\frac{Nh^2}{2} \sum_{j=1}^3 \bar{t}_j^{\,2} - \frac{1}{2\tau} \sum_{j=1}^3 T_j + i\epsilon \sum_{j=1}^3 \bar{t}_j + i\frac{\omega}{2} \sum_{j=1}^3 T_j}, \tag{2.89}$$

where the Jacobian is given by $\mathcal{J} = 2^{-3}$. Since the integrals factorise, we are able to consider them separately (they are identical for each i, with the exception that an extra t_i from the vertex is present for $i = 1, 3$). Beginning with $i = 1$, and after performing the T_1 integral immediately, we are left with

$$\begin{aligned} \left(\frac{2}{\tau^{-1} - i\omega}\right) \int_{-\infty}^{\infty} d\bar{t}_1 \; \bar{t}_1 \, e^{-\frac{Nh^2}{2}\bar{t}_1^{\,2}} e^{-\frac{|\bar{t}_1|}{2}(\tau^{-1} - i\omega)} e^{i\epsilon \bar{t}_1} = \left(\frac{2}{\tau^{-1} - i\omega}\right) \left(\frac{\sqrt{\pi}}{4h^4 N^{\frac{3}{2}}}\right) \times \\ \left[e^{\frac{(\sqrt{2}w + 4ih\epsilon)^2}{32h^4N}} (w + 2\sqrt{2}ih\epsilon) \operatorname{erfc}\left(\frac{w + 2\sqrt{2}ih\epsilon}{4h^2\sqrt{N}}\right) - e^{\frac{(\sqrt{2}w - 4ih\epsilon)^2}{32h^4N}} (w - 2\sqrt{2}ih\epsilon) \operatorname{erfc}\left(\frac{w - 2\sqrt{2}ih\epsilon}{4h^2\sqrt{N}}\right) \right], \end{aligned} \tag{2.90}$$

where for convenience we have defined

$$w = \Gamma^2\sqrt{N\pi} - i\sqrt{2}h\omega. \tag{2.91}$$

The $i = 2$ integrals are analogous, with the exception of the missing vertex factor, and yield

$$\left(\frac{2}{\tau^{-1} - i\omega}\right) \int_{-\infty}^{\infty} d\bar{t}_2 \, e^{-\frac{Nh^2}{2}\bar{t}_2^{\,2}} e^{-\frac{|\bar{t}_2|}{2}(\tau^{-1} - i\omega)} e^{i\epsilon \bar{t}_2} = \left(\frac{2}{\tau^{-1} - i\omega}\right) \left(\frac{\pi}{h\sqrt{2N}}\right) \times \tag{2.92}$$

$$\left[e^{\frac{w + 2\sqrt{2}ih\epsilon)^2}{16h^4N}} \left(1 - \operatorname{erf}\left(\frac{w + 2\sqrt{2}ih\epsilon}{4h^2\sqrt{N}}\right)\right) + e^{\frac{(w - 2\sqrt{2}ih\epsilon)^2}{16h^4N}} \left(1 - \operatorname{erf}\left(\frac{w - 2\sqrt{2}ih\epsilon}{4h^2\sqrt{N}}\right)\right)\right] \tag{2.93}$$

The scaling of the first-order (in γ) ladder diagram can be determined from (2.90) and is found to be

$$\mathbb{E}[C^x_{\text{Ladder, 1}}] \sim h^2N^2 \times N \times \left(\frac{h}{\sqrt{N}}\right)^2 \left(\frac{1}{h^4N^{3/2}}\right)^2 \times h^2 \times (h^2N)^{3/2} \tag{2.94}$$

$$\sim h\sqrt{N}. \tag{2.95}$$

The first factor (h^2N^2) comes from the derivative of the generating function; the next (N) is from γ; each factor of $hN^{-\frac{1}{2}}$ is from $\frac{1}{\tau^{-1}-i\omega}$, which arose from the T_i integration; $h^{-4}N^{-\frac{3}{2}}$ is the prefactor that emerged from the $\bar{t}_i$ integration; finally, $h^2(h^2N)^{\frac{3}{2}}$ is the scaling of the ϵ-integral (that is, the integral over ϵ of the square of the right-hand side of (2.90)). This scaling can be extracted by ignoring the complementary error function (i.e. approximating it by an $\mathcal{O}(1)$ constant in a region of width $h\sqrt{N}$ around $\epsilon = 0$) and considering the dominant terms in the remaining integrand,

$$\int_{-\infty}^{\infty} (h\epsilon e^{-\frac{\epsilon^2}{h^2N}})^2 \, d\epsilon \sim h^2(h^2N)^{3/2}, \tag{2.96}$$

a result which is borne out by numerical evaluation of the full integral.

In fact, all ladder diagrams exhibit the same $h\sqrt{N}$ scaling. We can see this from (2.92), which is the only additional contribution of an additional line (as the ϵ-integral is unchanged), which scales as

$$\overbrace{N}^{\gamma} \times \overbrace{\frac{h}{\sqrt{N}}}^{\frac{1}{\tau^{-1}-i\omega}} \times \overbrace{\frac{1}{h\sqrt{N}}}^{\int d\bar{t}} \sim 1. \tag{2.97}$$

Despite our attempt to construct an observable analogous to the conductivity in the single-particle calculation, we have found that the ladder diagrams do not vanish in this case and we will thus need to account for the renormalisation of the spin vertices that they induce.

Exact integration in the Schwinger proper-time representation is also a convenient way for us to check the scaling of crossed diagrams. Taking the example of the $\mathcal{O}(\gamma^2)$ crossed diagram (right figure in Fig. 2.1): the $i = 1, 3$ integrals are identical to the ladder case, whilst the t_2 and t'_2 can now be evaluated to give

$$\int_0^\infty \int_0^\infty dt_2 dt'_2 \, e^{-\frac{Nh^2}{2}(t_2^2+{t'_2}^2)} e^{-\frac{t_2+t'_2}{2\tau}} e^{i\epsilon(t_2-t'_2)} e^{i\frac{\omega}{2}(t_2+t'_2)} = \tag{2.98}$$

$$\frac{\pi}{2h^2N} e^{-\frac{4\epsilon^2+\frac{(\omega\tau+i)^2}{\tau^2}}{4h^2N}} \left(\operatorname{erfi}\left(\frac{2\epsilon\tau-\omega\tau-i}{\sqrt{8}h\sqrt{N}\tau}\right)+i\right)\left(\operatorname{erfi}\left(\frac{2\epsilon\tau+\omega\tau+i}{\sqrt{8}h\sqrt{N}\tau}\right)-i\right), \tag{2.99}$$

meaning that the diagram thus scales as

$$\mathbb{E}[C^x_{\text{Crossed, 2}}] = \overbrace{h\sqrt{N}}^{\int \prod_{i=1,3} dt_i dt'_i} \times \overbrace{N}^{\gamma} \times \overbrace{\frac{1}{h^2N}}^{\int dt_2 dt'_2}, \tag{2.100}$$

where we have also used the fact that the ϵ-integral is unchanged by the additional Gaussian factor. Unlike at the level of the resolvent, where the crossed diagrams were a factor of N smaller, here the suppression is only by a factor of h^{-2}. It is also clear (from the second and third terms above, which together contribute a factor of h^{-2}) that the maximally crossed diagram of order $O(\gamma^m)$ will scale as $\sqrt{N}/h^{2m-3}$. Since we are working in the weak-disorder regime where $h \gg 1$ (cf. (2.38)), this motivates us to consider the leading correction coming from the maximally crossed diagrams as in the weak-localisation calculation.

2.3.3 Cooperon ladder in the diffusive regime

The maximally crossed diagrams can be untwisted as in the single-particle case (cf. Figure 1.4); however, on the hypercube no minus sign appears, which can be traced back to a momentum conservation condition governed by the $\mathbb{Z}_2^N$ as opposed to the $(\mathbb{R}, +)$ group structure of the single-particle problem. Consequently, the cooperon can be immediately evaluated from the results in section 2.2.4 without invocation of time-reversal symmetry

$$C(x_q, \omega) = \frac{\gamma^2 \sum_{x_1} R(x_1) R^\dagger(x_1 x_q)}{1 - \gamma \sum_{x_2} R(x_2) R(x_2 x_q)} \tag{2.101}$$

$$= \frac{\gamma}{(DF - i\omega)\tau}, \tag{2.102}$$

recalling that $\xi(x_q) = N - 2F$.

We now can compute the corresponding correction to the two-point transverse spin correlator

$$\Delta\,\mathbb{E}[C^x(\omega)] = \frac{1}{2^N} \int \frac{d\epsilon}{2\pi} \sum_{\substack{x,x' \\ i,j}} x_j \left(\frac{1}{\epsilon - h\xi(x) - \frac{i}{2\tau}} \right) \left(\frac{1}{\epsilon + \omega - h\xi(x) + \frac{i}{2\tau}} \right) \frac{\gamma}{(DF - i\omega)\tau} \tag{2.103}$$

$$x_i' \left(\frac{1}{\epsilon - h\xi(x') - \frac{i}{2\tau}} \right) \left(\frac{1}{\epsilon + \omega - h\xi(x') + \frac{i}{2\tau}} \right), \tag{2.104}$$

where $x_q = xx'$. Working in the low-frequency limit and noting that the $x_q \approx 1$ sector dominates, we follow the approach of section 1.1.3 and neglect the x_q-dependence of the summand everywhere except for the most singular part (i.e. the cooperon).This leaves us with

$$\begin{aligned} \Delta\,\mathbb{E}[C^x(\omega \to 0)] &= \frac{1}{2^N} \int \frac{d\epsilon}{2\pi} \sum_x \xi(x)^2 \left(R(x, \epsilon + \omega)^2 R^\dagger(x, \epsilon)^2 \right) \sum_{x_q} \frac{\gamma}{DF(x_q)\tau} \\ &= \frac{N}{2^N} \int \frac{d\epsilon}{2\pi} g(0) \int \frac{d\xi}{2} \xi^2 \left(\frac{1}{\epsilon + \omega - h\xi + \frac{i}{2\tau}} \right)^2 \left(\frac{1}{\epsilon - h\xi - \frac{i}{2\tau}} \right)^2 \sum_{x_q} \frac{\gamma}{DF\tau}. \end{aligned} \tag{2.105}$$

Focussing on the behaviour of the sum over x_q, we can express it as an integral over F

$$\begin{aligned} \frac{\gamma}{D\tau}\sum_{x_q}\frac{1}{F} &= \frac{\gamma}{D\tau}\int d\xi\,\frac{g(\xi)}{N-\xi} \\ &= -\frac{\gamma}{D\tau}\int_{F_{\min}}^{F_{\max}} dF\,\binom{N}{F}\frac{1}{F}, \end{aligned} \tag{2.106}$$

in which the cutoffs for the F-integral are determined by the conditions $F \gg 1, h\sqrt{F}\tau \ll 1$ defining the diffusive regime, together with the weak disorder condition $(h\tau)^{-1} \ll \sqrt{N}$. Since these limits are in the tail of the density of states (whose maximum is at $F = N/2$), we cannot approximate the density of states by a constant and must instead extract its leading F dependence. With recourse to Stirling's approximation, we obtain the large deviations form

$$\ln\binom{N}{F} = N\left(-\mathcal{F}\ln\mathcal{F} - (1-\mathcal{F})\ln(1-\mathcal{F})\right), \tag{2.107}$$

where we have defined $\mathcal{F} = F/N$. Keeping only the first term, which is larger over the domain of integration, we obtain

$$-\frac{\gamma}{D\tau}\int_{\mathcal{F}_{\min}}^{\mathcal{F}_{\max}} d\mathcal{F}\,\frac{e^{-N\mathcal{F}\ln\mathcal{F}}}{\mathcal{F}} = -\frac{\gamma}{D\tau}\int_{\ln\mathcal{F}_{\min}}^{\ln\mathcal{F}_{\max}} du\; e^{-Nue^{u}}. \tag{2.108}$$

The fact that the integrand is increasing in the interval $[\mathcal{F}_{\min}, \mathcal{F}_{\max}]$ suggests that the contribution from the cooperon may be dominant outside the diffusive regime we have restricted to. Despite this break down of the analogy to the single-particle calculation, a similar issue has appeared in the context of weak localisation in the presence of smooth (i.e. long-range) disorder and clean, quantum chaotic systems: ballistic weak localisation. In that case, progress can be made by working with kinetic equations for products of Green's functions in the Wigner representation; in this treatment averaging is only performed at the end, meaning that we can take into account correlations of classical trajectories [108]. Unfortunately, we have been unable to formulate an equivalent approach here, due to the absence of a corresponding classical dynamics. Part of the problem is the absence of a continuous phase space structure and associated Wigner functions; although Wigner functions can be defined in the case of discrete Hilbert spaces [109], they are awkward to work with and it remains to be seen whether they can be profitably deployed in the present scenario. Be that as it may, in Chapter 3 we are able to pursue a somewhat related approach by working with a stroboscopic QREM and studying its time evolution with inspiration from periodic-orbit theory; this allows us to detect the emergence of the RMT limit.

2.4 Dynamics of the average density matrix

Even without a means of studying nonaveraged quantum corrections to kinetic equations, we are at least able to describe the dynamics of the average density matrix in its own right; this we shall do before looking at modified versions of the QREM in later chapters. In this section, we derive a quantum master equation for the disorder-averaged density matrix and explore how it can be analysed numerically and analytically.

2.4.1 Derivation of the quantum master equation

The time evolution of the density matrix is described by the von Neumann equation

$$\partial_t \rho(t) = -i[H, \rho(t)]. \tag{2.109}$$

If we split up the Hamiltonian into its kinetic and potential part as before, $H = T + V$, we can reexpress (2.109) in the interaction representation in which V is treated as a perturbation,

$$\partial_t \rho_I(t) = -i[V_I(t), \rho_I(t)], \tag{2.110}$$

where the interaction picture density matrix and potential are related to their Schrödinger picture counterparts by $\rho_I(t) = e^{iTt}\rho(t)e^{-iTt}$ and $V_I(t) = e^{iTt}Ve^{-iTt}$ respectively. Formal solution of (2.110) is a Volterra integral equation of the second kind given by

$$\rho_I(t) = \rho_I(0) - i\int_0^t dt_1\,[V_I(t_1), \rho_I(t_1)]. \tag{2.111}$$

Iterating once, averaging over V, and differentiating with respect to t gives us the (exact) equation of motion for $\mathbb{E}[\rho_I(t)]$

$$\partial_t\,\mathbb{E}[\rho_I(t)] = -\int_0^t dt_1\;\mathbb{E}\left[[V_I(t), [V_I(t_1), \rho_I(t_1)]]\right]. \tag{2.112}$$

Transforming back to the Schrödinger picture gives us a term describing unitary evolution (or the streaming term, in the classical language of kinetic equations) equal to the Liouvillian of T, plus a decoherence term (or collision integral) described by the double commutator. Expanding the double commutator reveals the division of the collision integral into so-called "out-" and "in-scattering" terms

$$\begin{aligned}
\partial_t\bar{\rho} =& -i[T, \bar{\rho}] && (2.113)\\
&-\int_0^t dt'\;\mathbb{E}\Big[\overbrace{VU_0(t-t')V\rho(t')U_0^\dagger(t-t') + U_0(t-t')\rho(t')VU_0^\dagger(t-t')V}^{\text{"Out"}}\Big] && (2.114)\\
&+\int_0^t dt'\;\mathbb{E}\Big[\overbrace{VU_0(t-t')\rho(t')VU_0^\dagger(t-t') + U_0(t-t')V\rho(t')U_0(t-t')V}^{\text{"In"}}\Big], && (2.115)
\end{aligned}$$

where $U_0(t) = e^{-iTt}$. We must now consider how to handle the integration over t' of terms of the form

$$\sum_{x,x'} \int_0^t dt' \, |x\rangle \langle x|V\rho(t)|x'\rangle \langle x'| \, e^{-ih(\xi(x)-\xi(x'))(t-t')}, \tag{2.116}$$

where we have inserted the spectral representation of the free evolution operators $U_0(t)$. If we make the approximation that $\rho(t)$ is slowly varying compared to the rapidly oscillating complex exponentials (i.e. we can replace $\rho(t)$ by its average $\bar{\rho}$), we need only integrate over the latter "fast" terms. In the long-time limit, this just amounts to the Fourier transform of the Heaviside step function

$$\int_0^t dt' \, e^{-ih(\xi(x)-\xi(x'))t'} \xrightarrow{t\to\infty} \frac{1}{h}\left(\mathcal{P}\left[\frac{i}{\xi(x')-\xi(x)}\right] + \pi\delta(\xi(x')-\xi(x))\right). \tag{2.117}$$

If we drop the imaginary part (analogous to dropping the real part of the self-energy for a particle in a random potential) and consider one of the "out" terms

$$-\frac{\pi}{h} \sum_{x_1,x_2,x_3,x_4} \mathbb{E}\left[|x_1\rangle \langle x_1|V|x_2\rangle \langle x_2|V|x_3\rangle \langle x_3|\bar{\rho}|x_4\rangle \langle x_4| \; \delta(\xi(x_2)-\xi(x_4))\right], \tag{2.118}$$

disorder averaging (making use of (2.14)) gives

$$\frac{\gamma\pi}{h} \sum_{x_1,x_2,x_3} |x_1\rangle \langle x_1|\bar{\rho}|x_3\rangle \langle x_3| \; \delta(\xi(x_2)-\xi(x_3)). \tag{2.119}$$

Recognising the sum $\sum_{x_2} \delta(\xi(x_2)-\xi(x_3))$ as the density of states $g(\xi(x_3))$, we can approximate it by a constant equal to its value in the middle of the band, $g(N/2)$, reducing the remaining summations to resolutions of the identity. Accounting for the other "out" term in the same fashion, we find the contribution of these terms is

$$\partial_t \bar{\rho}|_{\text{Out}} = -\frac{1}{\tau}\bar{\rho}, \tag{2.120}$$

where we have introduced a scattering rate $\tau^{-1} = 2\pi\gamma g(N/2)/h$. Turning to one of the "in" terms, it can be similarly averaged to yield

$$\frac{\gamma\pi}{h} \sum_{x_1,x_2,x_3} |x_1 \oplus x_3\rangle \langle x_1|\bar{\rho}|x_2\rangle \langle x_2 \oplus x_3| \; \delta(\xi(x_1)-\xi(x_2 \oplus x_3)). \tag{2.121}$$

If we make the approximation of neglecting the delta function and transform to the z-basis, we find that the "in" term becomes

$$\partial_t \bar{\rho}|_{\text{In}} = \frac{2^N}{g(N/2)\tau} \sum_z |z\rangle \langle z|\bar{\rho}|z\rangle \langle z|, \tag{2.122}$$

which simply describes dephasing in the z-basis. This approximation has introduced an error: the "out" and "in" scattering rates are not equal, giving an unphysical master equation that does not preserve the trace of the density matrix. We remedy this with the ad hoc replacement of the "in" scattering rate by τ^{-1} (a reduction by a factor of order $\sqrt{N}$, which we can attribute to the constraint in the sum in (2.121) that we did not account for).

The quantum master equation for $\bar{\rho}$ (we shall henceforth omit the bar on ρ) is thence

$$\partial_t \rho = -i[T, \rho] + \frac{1}{\tau}\left(\sum_z |z\rangle \langle z| \rho |z\rangle \langle z| - \rho\right) = \mathcal{L}[\rho]. \tag{2.123}$$

The density matrix can be regarded as an element of $\mathcal{H} \otimes \mathcal{H} \cong \mathbb{C}^{4^N}$ via the Choi isomorphism. In this representation, the Liouvillian in (2.123) can be recast as an effective Hamiltonian for a two-flavour system of $2N$ spins: σ_i^a, τ_i^a for $i = 1, \ldots, N$ and $a = x, y, z$. The effective Hamiltonian takes the form

$$H_{\text{eff}} = -ih \sum_{i=1}^{N} (\sigma_i^x - \tau_i^x) - \frac{1}{\tau}\mathbb{1} + \frac{1}{\tau} \prod_{j=1}^{N} \frac{1}{2}(\sigma_j^z \tau_j^z + 1). \tag{2.124}$$

2.4.2 Spectrum

We can make some sense of the spectrum of (2.124) (see Fig. 2.2) by perturbation theory in h. For $h = 0$, there are 2^N zero modes and the remaining $4^N - 2^N$ eigenvalues are equal to $-\tau^{-1}$. Second-order degenerate perturbation theory implies that the zero modes are split as soon as h becomes nonzero, with a spectral gap (i.e. eigenvalue with the most positive, nonzero real part) of $-4h^2\tau$. The spectrum, specifically the spectral gap or most slowly relaxing mode, controls the asymptotic behaviour – but we need to consider time evolution if we want to identify dynamical phenomena, such as the cutoff phenomenon. Numerical analysts have studied cutoff phenomena in Markov chains [110] by considering the norms of powers of the "decay matrix" ($\mathsf{P} - \mathsf{P}^\infty$, for transition matrix P; P^∞ is thus the projector onto the stationary eigenspace). This approach is made numerically feasible (i.e. systems large enough for the behaviour to be seen can be analysed) thanks to dimensional reductions possible in a number of problems, such as the reduction of the random walk on the hypercube to the Ehrenfest urn problem – a reduction of the state space from 2^N to $N + 1$. We now proceed to perform a dimensional reduction for the problem under consideration.

2.4.3 Permutation symmetry and dimensional reduction

The transverse field term of (2.124) is invariant under independent permutations of the σ_i and τ_i, which suggests that the natural basis for this term, i.e., the one respecting this symmetry, is $|h_1\rangle \otimes |h_2\rangle$, where $|h\rangle$ is the symmetric combination of $|z\rangle$ states with Hamming distance h from the fully polarised $|1 \ldots 1\rangle$ state. However, due to the collision integral, H_{eff} is only invariant under simultaneous permutations of σ_i, τ_i. Since the Hamiltonian has this permutation symmetry (described by the symmetric group, S_N), we are motivated to decompose the Hilbert space $\mathcal{H} \otimes \mathcal{H}$ into subspaces transforming as irreducible representations of S_N. We can readily identify the subspace transforming as the totally symmetric representation (i.e. each state is

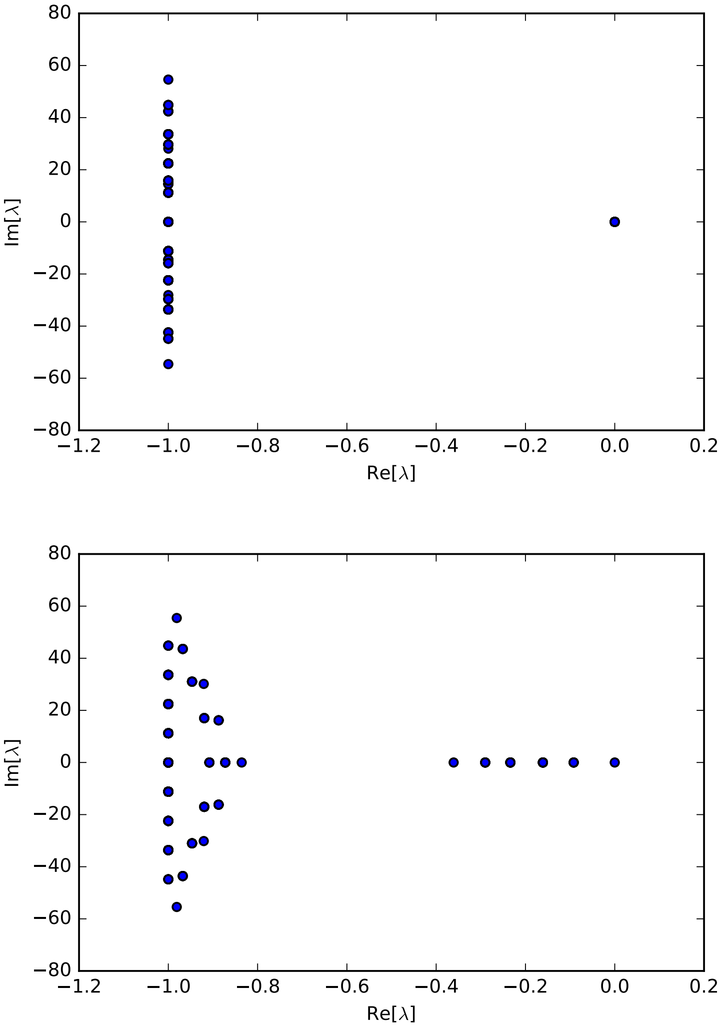

FIGURE 2.2: Spectrum of the effective Hamiltonian (2.124) obtained by exact diagonalisation ($N = 5$) for the cases $h = 0.1$ (top) and $h = 0.9$ (bottom), illustrating the splitting of the degenerate multiplet of zero modes.

invariant under all permutations of N spins) as containing states where the Hamming distance h_{12} between $|h_1\rangle$ and $|h_2\rangle$ is also fixed. We can write these as

$$|\boldsymbol{h}\rangle = |h_1, h_2, h_{12}\rangle = \frac{1}{\mathcal{N}_{h_1,h_2,h_{12}}} \sum_{\substack{\xi(z_1),\xi(z_2)=h_1,h_2 \\ \xi(z_1\oplus z_2)=h_{12}}} |z_1\rangle \otimes |z_2\rangle \,, \tag{2.125}$$

where $\mathcal{N}^{(N)}_{h_1,h_2,h_{12}} = \binom{N}{h_{12}}\binom{h_{12}}{\frac{h_1-h_2+h_{12}}{2}}\binom{N-h_{12}}{\frac{h_1+h_2-h_{12}}{2}}$. In passing, we note that the normalisation coefficients $\mathcal{N}_{\boldsymbol{h}}$ are related to the intersection parameters p^h_{ij} of a Hamming scheme, but we relegate their explicit computation to appendix B.

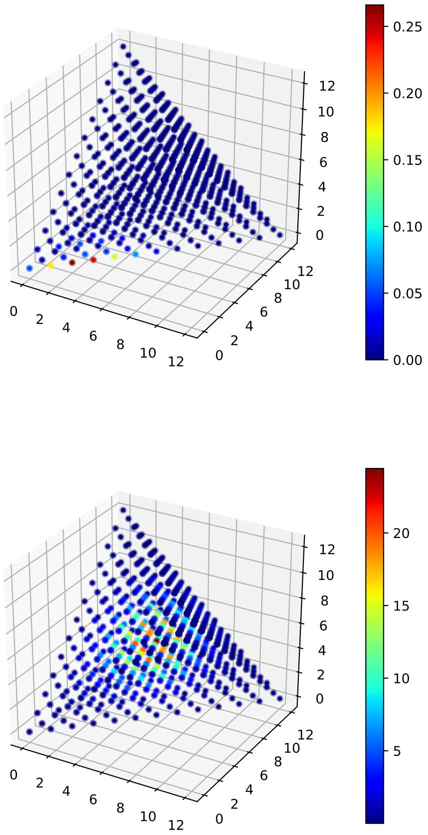

Figure 2.3: Time evolution of the master equation (2.126) in the permutation-invariant subspace for a) strong disorder ($h = 0.5$), in which strong dephasing results in a rapid collapse of probability density onto the diagonal, followed by drift towards the stationary state $(N/2, N/2, 0)$ and b) weak ($h = 2$) disorder in which there is a nontrivial drift and spreading of probability density, before it eventually concentrates on the stationary state.

A dimensional reduction is thus possible by projecting the master equation onto the $|\boldsymbol{h}\rangle$ basis, since it is an invariant subspace of H_{eff}. Performing this projection gives

$$\begin{aligned}
\partial_t \rho_{h_1,h_2,h_{12}} &= -\frac{1}{\tau}\left(1-\delta_{h_1,h_2}\delta_{h_{12},0}\right)\rho_{h_1,h_2,h_{12}} \qquad (2.126)\\
&- i(\alpha_{+0+}^{h_1-1,h_2,h_{12}-1}\rho_{h_1-1,h_2,h_{12}-1}+\alpha_{-0+}\rho_{h_1+1,h_2,h_{12}-1}+\alpha_{+0-}\rho_{h_1-1,h_2,h_{12}+1}+\alpha_{-0-}\rho_{h_1+1,h_2,h_{12}+1})\\
&+ i(\alpha_{0++}^{h_1,h_2-1,h_{12}-1}\rho_{h_1,h_2-1,h_{12}-1}+\alpha_{0-+}\rho_{h_1,h_2+1,h_{12}-1}+\alpha_{0+-}\rho_{h_1,h_2-1,h_{12}+1}+\alpha_{0--}\rho_{h_1,h_2+1,h_{12}+1})
\end{aligned}$$

where the α-coefficents are given by

$$\begin{aligned}
\alpha_{+0+}^{h_1-1,h_2,h_{12}-1} &= h\left(N - \frac{h_1+h_2+h_{12}-2}{2}\right)\\
\alpha_{+0-}^{h_1-1,h_2,h_{12}+1} &= \frac{h}{2}\left(h_2-h_1+h_{12}+2\right)\\
\alpha_{-0+}^{h_1+1,h_2,h_{12}-1} &= \frac{h}{2}\left(h_1+h_2-h_{12}+2\right)\\
\alpha_{-0-}^{h_1+1,h_2,h_{12}+1} &= \frac{h}{2}\left(h_1-h_2+h_{12}+2\right),
\end{aligned}$$

and satisfy $\alpha_{0ij}^{h_1,h_2,h_{12}} = \alpha_{i0j}^{h_2,h_1,h_{12}}$. The density matrix components in this basis are defined by

$$|\rho(t)\rangle = \sum_{\mathbf{h}} \rho_{h_1,h_2,h_{12}}(t)\,|\mathbf{h}\rangle\,, \tag{2.127}$$

where the normalisation is such that $\langle \boldsymbol{h}|\rho(t)\rangle = \mathcal{N}_{\mathbf{h}}^{-1}\rho_{\mathbf{h}}$, which ensures the preservation of the trace of the density matrix: $\mathrm{tr}(\rho) = \sum_{h=0}^{N}\rho_{h,h,0} = 1$. Numerical integration of (2.126) is straightforward and the resultant time evolution of (2.126) is displayed in Fig. 2.3.

2.4.4 Reduced density matrix

The $(N-k)$-spin reduced density matrix $\rho_{(N-k)} = \mathrm{tr}_k(\rho_N)$ satisfies the same kinetic equation as the full density matrix. Consider first the unitary part of the dynamics, and trace out a subset S of the spins

$$\partial_t\,\mathrm{tr}_S(\rho) = \partial_t\rho_{\bar{S}} = -ih\sum_{j=1}^{N}\mathrm{tr}_S([\sigma_j^x,\rho]). \tag{2.128}$$

If $j\notin S$, then $\mathrm{tr}_S([\sigma_j^x,\rho]) = [\sigma_j^x,\mathrm{tr}_S(\rho)]$. If $j\in S$, then $\mathrm{tr}_S(\sigma_j^x\rho) = \mathrm{tr}_S(\rho\sigma_j^x)$ and so the commutator vanishes. The corresponding evolution of $\rho_{\bar{S}}$ is thus the natural restriction of the unitary dynamics to $\bar{S}$.

Now we turn to the collision integral, $\hat{W}\rho = \frac{1}{\tau}\left(\sum_z |z\rangle\langle z|\rho|z\rangle\langle z| - \rho\right)$, which similarly preserves its form upon tracing out a subset of the spins

$$\mathrm{tr}_S(\hat{W}\rho) = \frac{1}{\tau}\left(\sum_{z\in\mathbb{Z}_2^{|\bar{S}|}} |z\rangle\langle z|\rho_{\bar{S}}|z\rangle\langle z| - \rho_{\bar{S}}\right). \tag{2.129}$$

The kinetic equation for the reduced density matrix is thus the same as that of the full density matrix, but restricted to the relevant subset of the spins.

We can hence explicitly solve the kinetic equation for the one-spin reduced density matrix, which we parameterise by the Bloch vector $\vec{n}$ as $\rho_1(t) = \frac{1}{2}\left(\mathbb{1} + \vec{n}(t)\cdot\vec{\sigma}\right)$. The equation of motion for $\vec{n}(t)$ is

$$\partial_t \vec{n} = \begin{pmatrix} -1/\tau & 0 & 0 \\ 0 & -1/\tau & -2h \\ 0 & 2h & 0 \end{pmatrix} \begin{pmatrix} n_x \\ n_y \\ n_z \end{pmatrix}, \tag{2.130}$$

with solution

$$\vec{n}(t) = \begin{pmatrix} n_x(0)e^{-t/\tau} \\ \frac{1}{2\lambda} e^{-t(1+\lambda)/2\tau} \left(-4n_z(0)h\tau(-1 + e^{-\lambda t/\tau}) + n_y(0)(1 + \lambda + e^{\lambda t/\tau}(-1+\lambda)) \right) \\ e^{-t/2\tau} \left(n_z(0)\cosh(\lambda t/2\tau) + \frac{n_z(0) - 4n_y(0)h\tau}{\lambda} \sinh(\lambda t/2\tau) \right) \end{pmatrix}, \tag{2.131}$$

where $\lambda = \sqrt{1 - 16h^2\tau^2}$. In Figure 2.4, the evolution of the one-spin reduced density matrix is shown on the Bloch sphere: a spiral trajectory follows from the combination of precession due to the kinetic term and decay towards the maximally mixed state due to the collision integral.

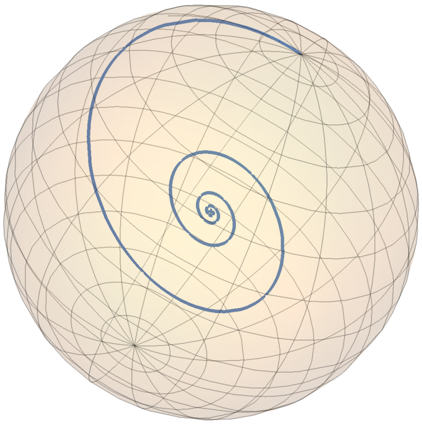

FIGURE 2.4: Time evolution of the one-spin reduced density matrix on the Bloch sphere.

2.5 Conclusions

In this chapter, our main objective was to study the QREM by means of an analogy to the disorder-averaged diagrammatic perturbation theory approach to the problem of single-particle weak localisation. Although the analogy held as far as the validity of the self-consistent Born approximation and subsequent computation of the diffuson was concerned, we found that the contribution of the cooperon (or diffuson) to two-particle correlation functions was dominant outside the diffusive regime in which they had been calculated. In contrast to the single-particle theory of a disordered metal, the diffusive regime was without physical motivation here, instead being defined on the basis of a mathematical analogy. We were unable to evaluate correlation functions in the relevant nondiffusive regime; analogies to the treatment of ballistic diffusons and cooperons were of no avail, so further work is called for if there is to be a conclusive answer to the question of whether weak-localisation-like corrections to the RMT limit appear in the QREM. Although not providing any insight into this question, we did manage to develop a master equation description for the dynamics of the disorder-average density matrix, from which we could find an analytic form for the single-spin reduced density matrix. It would be useful to also understand the two- and higher-spin reduced density matrix dynamics, which would provide information about multi-spin correlators, but more work will be required to obtain an intelligible form for these quantities. An avenue that might be worth exploring is to turn to the quantum de Finetti theorem [111]: permutation invariance of the average density matrix can be further exploited to show that the k-spin reduced density matrix can be expressed as the expectation (with respect to some distribution to be determined) of the k^{th} tensor power of a single-spin density matrix; the problem would then be to find a kinetic equation for the governing distribution.

Chapter 3

Stroboscopic quantum random energy model as a quantum graph

Here we interpret the quantum random energy model under stroboscopic evolution as a quantum graph, and so are able to make use of the semiclassical tool of periodic-orbit theory to study spectral correlations. As we discussed in Chapter 1, periodic-orbit theory enables the exact calculation of the form factor for quantum graphs. For certain classes of graph, the RMT result is precisely reproduced thereby providing a rigorous verification of the BGS conjecture for these special cases. Similarly, we explicitly compute the first-order term in the short-time expansion (diagonal approximation) of the form factor for the stroboscopic QREM and find agreement with GOE statistics (at large enough times) as expected. Based on our quantum graph interpretation that enables us to draw upon exact results as well as our numerics and analytic approximation, we are able to claim that the spectral statistics of the ergodic phase of the model will be precisely those of the GOE.

3.1 Introduction

The Hamiltonian of the stroboscopic QREM (of period $\mathcal{T}$) is given by

$$H(t) = V + T \sum_{j=0}^{\infty} \delta(t - j\mathcal{T}), \tag{3.1}$$

where V and T are the REM (of variance $\gamma_z = N/2$ as in Chapter 2) and kinetic terms respectively of the N-spin QREM defined in (2.1); this describes an REM that is periodically kicked by a uniform transverse field. The corresponding Floquet operator $\mathsf{F} := U(\mathcal{T})$, the time-evolution operator for a single period of the drive, factorises into a product of two unitary evolution operators according to

$$\mathsf{F} = \mathbb{T}\left[e^{-i\int_0^{\mathcal{T}} H(t)\, dt}\right] = e^{-iV\mathcal{T}} e^{-iT}. \tag{3.2}$$

If we work in the z-basis, the first factor (the exponential of the REM term) is a log-normal diagonal random matrix. We can immediately draw a parallel to the evolution map U_B for quantum graphs discussed in (1.44). In Chapter 2, we regularly made use of the bijection between the 2^N x- or z-basis states of the system and the vertices of the hypercube; it is thus more convenient to stay closer to this picture and consider the wavefunction to be defined on the vertices of a graph rather than the on edges as for quantum graphs. Since the S-matrix e^{-iT} (T, the kinetic term in (3.1), is not to be confused with the quantum graph bond propagation matrix in section 1.3) allows scattering between any two z-states (all matrix elements are nonzero), the appropriate graph structure is really the complete graph on 2^N vertices (though a hypercube can be seen to emerge in the small-h limit). To preserve the analogy when we move to this dual object, we note that the role of incommensurate bond lengths of the quantum graph can be seen to be played by the random phases (V) which we assign to each vertex [1].

3.2 Spectral statistics

3.2.1 Numerics

If we only observe the system stroboscopically, that is, at integer multiples of τ, then we can describe the evolution in terms of a time-independent effective ('Floquet') Hamiltonian H_{F}

$$U(m\mathcal{T}) = \mathsf{F}^m = e^{-iH_{\mathrm{F}}m\mathcal{T}} \quad (m \in \mathbb{Z}). \tag{3.3}$$

We can identify transition between a localised and ergodic phase as the transverse field strength h is increased by studying the spectral statistics of the Floquet Hamiltonian. Unlike for the Hamiltonian QREM, we expect no mobility edge in the periodically driven version – the drive couples localised states to distant extended states thereby delocalising them [114, 115]. The spectrum of the Floquet Hamiltonian (known as the quasienergy spectrum; a temporal analogue of the quasimomenta in the Bloch wavefunctions of translation-invariant systems) is most conveniently obtained by diagonalising the Floquet operator and extracting its eigenphases; since F is unitary its spectrum lies on the unit circle in the complex plane. In this chapter, unqualified use of the term 'spectrum' (and derivative terms) shall always refer to these eigenphases.

The most direct way in which the transition can be visualised is by plotting the eigenphases as a function of h for a single realisation, as shown in Fig. 3.1; for $h < h_c \approx 0.2$ one observes a significant density of level crossings, whilst for $h > h_c$ increasing level repulsion is apparent. Analogous behaviour can be seen in the Hamiltonian spectrum of the Anderson model [116], whilst the quantum kicked top shows no sign of an Anderson transition in its Floquet spectrum, with level repulsion apparent for all nonzero values of the kicking strength [117]. Since the eigenphases are only defined modulo 2π, we choose $\theta_i \in [-\pi, \pi)$; a consequence of this is that jumps appear in plots of the eigenphases whenever one of the θ_i reaches the boundary and emerges on the opposite end of the spectrum. In Fig. 3.1, we have eliminated these jumps by selecting a subset of eigenphases in the middle of the spectrum and performing circular shifts of the spectrum wherever jumps occur.

---

[1] Although we find it helpful to make this analogy to quantum graphs, we point out that a periodic-orbit theory for Floquet operators can be constructed without reference to quantum graphs, see for instance Refs. [112, 113].

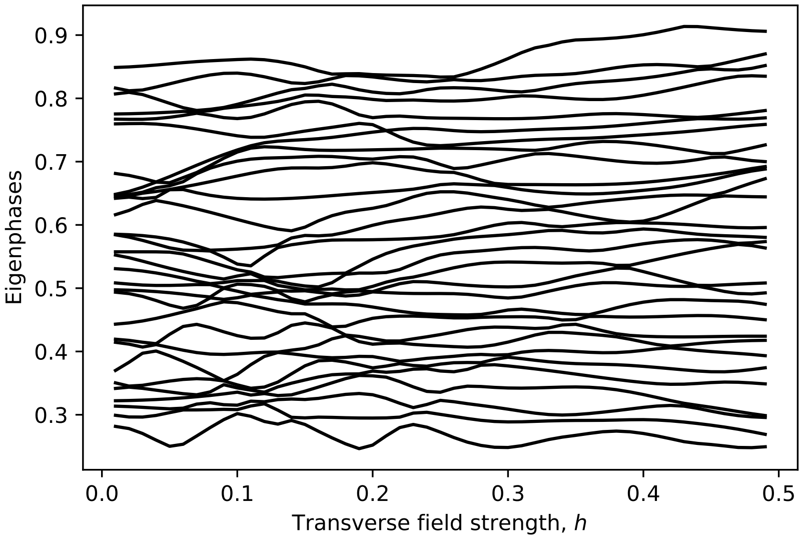

FIGURE 3.1: Parametric motion of a subset of the eigenphases ($N = 10$) as the transverse field strength is increased for a fixed disorder realisation. The localised-ergodic transition at around $h_c \approx 0.2$ can be seen in the form of the increased level repulsion visible at larger h.

As discussed in Chapter 1, the presence of level repulsion can be diagnosed more quantitatively by looking at the disorder-averaged distribution of the nearest-neighbour level spacing. In order to study this quantity in generic many-body systems, the spectrum must first be rescaled by the averaged local density of states such that it is everywhere equal to one; it is the so-called unfolded spectrum that exhibits universality in its spectral statistics [118]. One can alternatively account for a varying density of states by working with level spacing ratios, which have also been shown to take universal values [49]. However, here we enjoy a considerable simplification as the averaged density of states is uniform, obviating the need for an unfolding procedure, which is rather intricate to implement in practice [57]. This can be seen by appealing to the (proto) trace formula (1.47) for the eigenphase density (exact for quantum graphs) [72], from which we can see that $1/\bar{\delta} = \mathbb{E}\left[\rho(\theta)\right] = 2^N/2\pi$. In Fig. 3.2, we plot the averaged level-spacing distribution $\mathbb{E}\left[P(s)\right]$ (where $s = (\theta_{i+1} - \theta_i)/\bar{\delta}$) for two values of h on either side of the transition (but not close to it, where intermediate statistics can be observed).

As the level-spacing distribution is sensitive to short-range (compared to the mean level spacing $\bar{\delta}$) spectral correlations, the linearly vanishing probability density as $s \to 0$ in the regime of random matrix statistics being the signature of short-ranged level repulsion, we are able to complement this with a measure of long-range correlations: the number variance $\Sigma^2(n)$ (see Fig. 3.3). The $\Sigma^2(n)$ statistic is the variance in the number of levels within an energy window of length n (after rescaling the spectrum by $\bar{\delta}$) in the middle of the spectrum (in our case, it actually doesn't matter where we position the window as there is no many-body mobility edge). Sublinear growth of the number variance describes the feature known as spectral rigidity. As

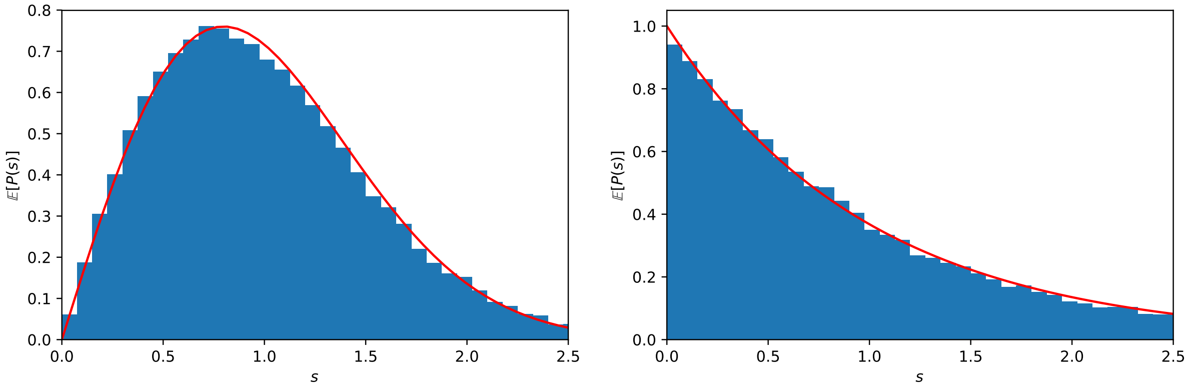

FIGURE 3.2: The averaged level-spacing distribution $\mathbb{E}[P(s)]$ ($N = 8$ and 200 disorder realisations) plotted for (left) $h = 0.5$ and (right) $h = 0.01$, to illustrate the two well-defined regimes: Dyson's circular orthogonal ensemble and Poisson statistics respectively (shown with red lines). It turns out that the level-spacing distributions for the circular ensembles in the large-N limit are the same as that of the Gaussian (Wigner-Dyson) ensembles of random Hermitian matrices, so it is in fact that the latter that we plot.

seen in Ref. [51], at small n we observe an upward deviation from the logarithmic growth expected in the regime of circular orthogonal ensemble (COE) statistics (see (1.37)) – a sign of a many-body Thouless energy in the system. Pinning down this Thouless energy more precisely is something that will be facilitated by turning our attention to the form factor, which has the advantage that it is also amenable to analytic calculation.

3.3 Spectral form factor in the diagonal approximation

The Fourier transform of the two-level correlation function

$$R(\phi;\theta) = \mathbb{E}\left[\rho(\theta)\rho(\theta+\phi)\right] \tag{3.4}$$

with respect to ϕ is known as the spectral form factor; if we use the density of states formula (1.47) and average over θ it can be written as

$$K_m = \mathbb{E}\left[\left|\mathrm{tr}\,(F^m)\right|^2\right], \tag{3.5}$$

for discrete time $m \in \mathbb{Z}$. In the quantum chaos literature, it is common to rescale the time by the Heisenberg time to identify universal features of the form factor, which in our case gives the quasicontinuous time $\tau = m/2^N$. Inserting the trace formula (1.48) for the traces of integer powers of the Floquet operator

$$\mathrm{tr}\,\mathsf{F}^m = \sum_{p\in\mathcal{P}_m} n_p \mathcal{A}_p^r e^{iS_p}, \tag{3.6}$$

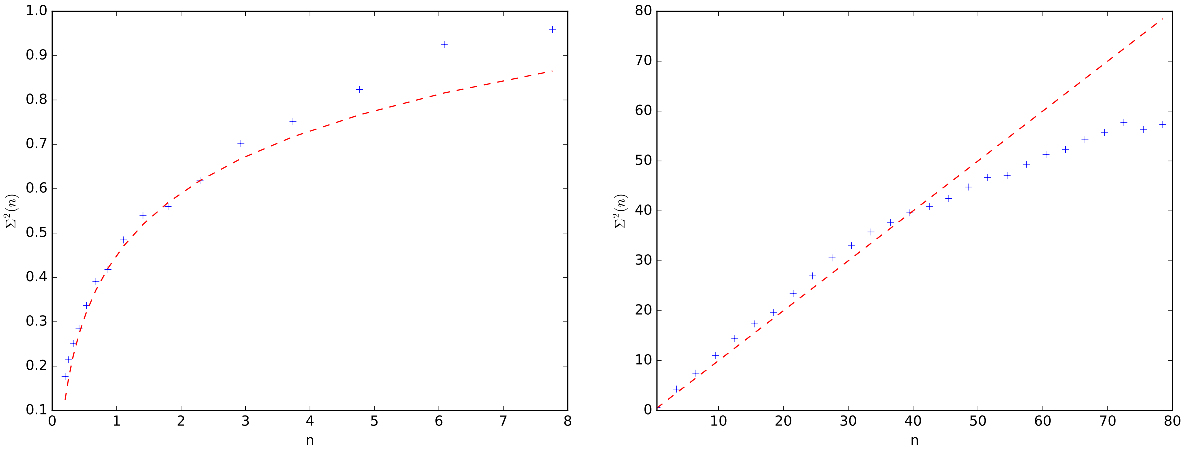

FIGURE 3.3: The number variance $\Sigma^2(n)$ plotted for (left) $h = 0.5$ (2000 realisations) and (right) $h = 0.01$ (1000 realisations). The dotted lines are (left) $\Sigma^2(n) = \frac{2}{\pi^2}\ln(n) + \text{const.}$ and (right) $\Sigma^2(n) = n$, illustrating the COE limit in which the logarithmic growth is a signature of spectral rigidity, and the Poissonian limit of linear growth indicating an absence of long-range correlations. The departure of the exact diagonalisation data from the fits with increasing n is a finite-size effect resulting from the small $N = 8$ system size.

where $\mathcal{P}_m$ is the set of primitive periodic orbits of length m and we have condensed the exponent into an action S_p since its details are unimportant here, gives the expression for the form factor

$$K_m = \sum_{p,p' \in \mathcal{P}_m} \mathbb{E}\left[\mathcal{A}_p \mathcal{A}^*_{p'} e^{i(S_p - S_{p'})}\right]. \tag{3.7}$$

If we make the diagonal approximation of keeping only the terms where $p = p'$ and exploiting the definition of $\mathcal{A}_p$ (given below (1.48)) as a product of matrix elements of the scattering matrix, we are left with

$$K_m^{\text{diag}} = 2m\,\text{tr}(\mathsf{P}^m), \tag{3.8}$$

where the factor of 2 in the numerator is a consequence of time-reversal symmetry, the factor of m accounts for orbits related by cyclic permutation, and $\mathsf{P} = |\mathsf{F}|^2$. In the diagonal approximation, we can see that time evolution of the form factor is completely controlled by the Peron–Frobenius operator (also known as the transfer or classical evolution operator) P, which describes a Markov process on the complete graph. To compute it, we note that in the z-basis T is a tensor product over sites of matrices of the form

$$\exp(-ih\sigma_x) = \cos(h)\mathbb{1} - i\sin(h)\sigma_x, \tag{3.9}$$

so that in this basis we can write down the Perron-Frobenius operator as

$$\mathsf{P} = \bigotimes_j \begin{pmatrix} \cos^2 h & \sin^2 h \\ \sin^2 h & \cos^2 h \end{pmatrix}_j. \tag{3.10}$$

The eigenvalues of P are given by $\lambda_j = (\cos^2(h) - \sin^2(h))^j$ for $j = \{0, 1, \cdots, 2^N\}$, resulting in a spectral gap $\Delta = 2\sin^2(h)$. The form factor for complete (i.e. fully connected) quantum graphs [71] with incommensurate bond lengths, and later all correlators [119], were first shown to attain RMT universality. Later, this has been extended to simply connected quantum graphs with a finite gap Δ for $|B| \to \infty$ [120]. Tanner has conjectured that the criterion for the attainment of random matrix universality is for the gap to vanish slowly enough with the dimension of the unitary map (equal to 2^N here), in our case this means specifically that $\Delta \sim 2^{-\alpha N}$ for $0 \leq \alpha < 1$, which we can see is trivially satisfied. This represents a refinement of an earlier suggestion that a sufficient condition is for the classical Markov process to be mixing (i.e. there is exactly one eigenvalue of unit modulus) [70], but for which counterexamples were quickly found, such as the Neumann star graph whose form factor fails to attain the RMT limit – a situation referred to as the absence of quantum ergodicity [121, 122]. For the problem at hand, since Δ is nonzero and independent of N for $h \neq 0$, on the basis of Tanner's conjecture [123] one may predict (in fact, since we can invoke the proof for gapped simply connected graphs, we can be quite confident of) a random matrix limit for large N in which the spectral statistics follow that of the circular orthogonal ensemble (COE). One point to note is that λ_j has degeneracy $\binom{N}{j}$, and so the density of modes with the lowest gap Δ scales with N. However, there is no reason to think that this should change the prediction for the case of a constant gap (if anything, one might speculate that a sufficiently rapid growth with N of the density of the slowest decay modes could compensate for a gap closing with N; the issue of competition between a growing density of states and a slowing decay rate is discussed in the context of the Sachdev–Ye–Kitaev (SYK) model in Ref. [124]).

Substituting the expression for P from (3.10) into (3.8) leaves us with [2]

$$K_m^{\text{diag}} = 2m(1 + \cos(2h)^m)^N, \tag{3.11}$$

which for large N indeed tends to the short-time random matrix result for the COE, $K_m^{\text{COE}} \approx 2m$, at sufficiently large times (but much shorter than the Heisenberg time, where the diagonal approximation breaks down). The (integer) time after which we expect the onset of the COE limit is thus m_c such that $N\cos(2h)^m \sim 1$, or

$$m_c = -\left\lceil \frac{\ln N}{\ln \cos(2h)} \right\rceil. \tag{3.12}$$

Just as we saw that the number variance deviated from the random matrix result for energy intervals larger than some cutoff, we see here in Fourier space the deviations occurring for times below the cutoff m_c (see Fig. 3.4), which is therefore a measure of the Thouless time. The single-particle Thouless time can be interpreted as the time for a particle to diffuse across the full length of a system; this leads one to suppose that the many-body Thouless time seen in the form factor might exhibit the same scaling as the cutoff time for diffusion on the hypercube discussed in Chapter 2, but the latter time scales as $N \ln N$ meaning that the connection between these two time scales is not clear at present. A similar result for the Thouless energy, namely logarithmic scaling with system size, has recently been obtained in a closely related model in the one-dimensional case – a random unitary circuit for which an exact calculation of the form factor is possible in the limit of $q \to \infty$ (where q is the local Hilbert space dimension) via a mapping to the Potts model [125]. The $\ln N$ time scale coincides with the scrambling time for 'fast scramblers', such as black holes or holographic models like the SYK model [3] that are highly nonlocal (like the QREM) [90, 126], so it is of particular interest that it nonetheless appears in the aforementioned unitary circuit model featuring local, indeed, solely nearest-neighbour coupling.

---

[2] As noted in the preface of this thesis, precisely this result appears in Ref. [1] via an interpretation of $K_{\text{diag}}(\tau)$ in terms of the partition function of a one-dimensional classical Ising model.

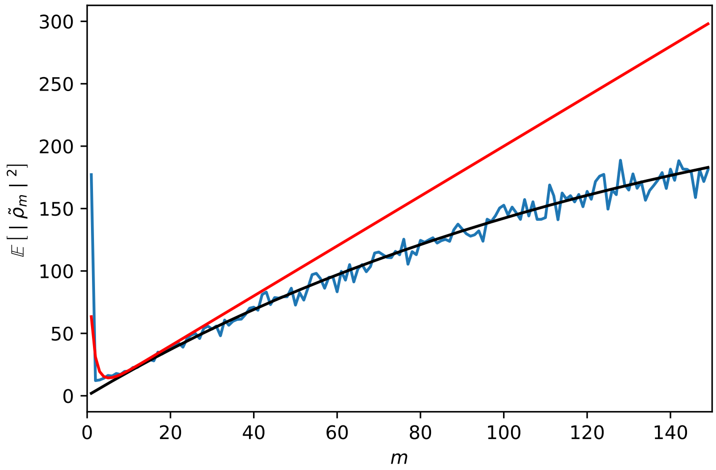

FIGURE 3.4: The disorder-averaged form factor is plotted as a function of the integer time ($m = 2^N \tau$) for $h = 0.5, N = 8$, and 400 disorder realisations. At times after the Thouless time but before the Heisenberg time, there is an excellent fit to the $N \to \infty$ limit of the COE form factor (black), whilst the form factor in the diagonal approximation is able to capture the upturn seen at short times. The value of h was chosen to ensure a finite Thouless time (there is a divergence at $h = \pi/2$) whilst also remaining in the ergodic regime, in order to demonstrate both the nonuniversal short-time behaviour as well as the convergence to the RMT limit at longer times.

Since the form factor is the Fourier transform of the two-level correlation function, the easiest way to access it numerically is to exploit the Wiener-Khinchin theorem: the Fourier transform of the autocorrelation function of a process is equal to the power spectrum of that process. The form factor is therefore given by the power spectrum of the density of states, which we can

---

[3] In Ref. [124], the form factor of the SYK model is studied in the same spirit as our approach in Chapter 2 – identifying the analogue of the diffusion modes in disordered metals – but the Thouless time is found to scale as $\sqrt{N} \ln N$. A clear explanation for the origin of this discrepancy has yet to emerge.

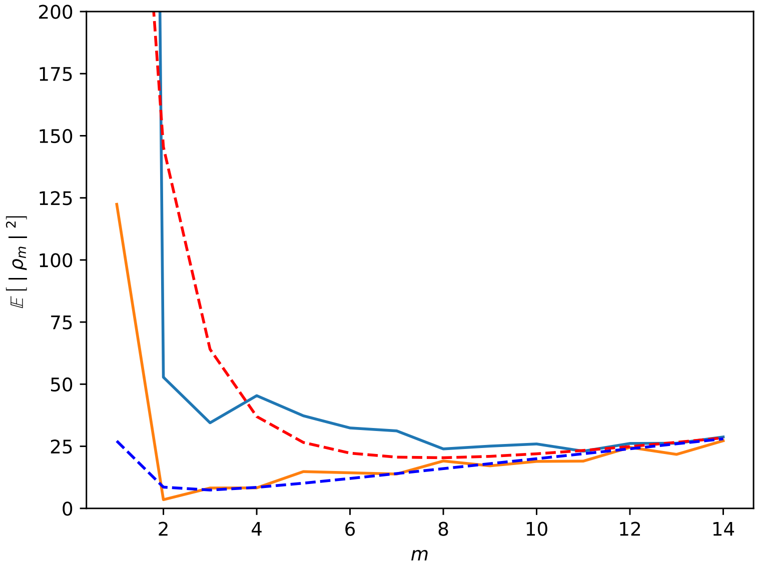

FIGURE 3.5: An expanded view of the short time region of the form factor for $h = 0.45$ (blue) and $h = 0.65$ (orange) shown in Fig. 3.4; we have used a larger system size $N = 11$ (50 realisations) to make the change in position of the minima with h more pronounced; the shift is well described by the form factor in the diagonal approximation ((3.11)) at the corresponding values of h (dashed lines).

explicitly verify from the definition of the density of states $\rho(\theta)$ as follows,

$$\rho(\theta) = \sum_j \delta_{2\pi}(\theta - \theta_j) \tag{3.13}$$

$$= \frac{1}{2\pi} \sum_j \sum_{m=-\infty}^{\infty} e^{im(\theta-\theta_j)} \tag{3.14}$$

$$= \frac{1}{2\pi} \sum_{m=-\infty}^{\infty} \tilde{\rho}_m e^{im\theta} \tag{3.15}$$

where in the second line we have inserted the Fourier series representation of the 2π-periodic Dirac delta $\delta_{2\pi}(\theta)$, and in the third we have recognised the appearance of the Fourier components of the density of states $\tilde{\rho}_m = \sum_j e^{im\theta_j}$ evaluated at integer times m. After writing down the two-level correlation function

$$\mathbb{E}[\rho(\theta)\rho(\theta+\phi)] = \left(\frac{1}{2\pi}\right)^2 \sum_{m_1,m_2} \mathbb{E}\left[\tilde{\rho}_{m_1}\tilde{\rho}_{m_2}\right] e^{im_1\theta} e^{im_2(\theta+\phi)}, \tag{3.16}$$

it follows upon averaging over θ that the form factor, given by the Fourier components (conjugate to the level difference ϕ) of the above correlator, is given by power spectrum of the the density of states $\tilde{\rho}_m\tilde{\rho}_{-m} = |\tilde{\rho}_m|^2$ (up to normalisation). The form factor computed by exact diagonalisation is shown in Figs. 3.4 and 3.6, for the ergodic and localised regimes respectively.

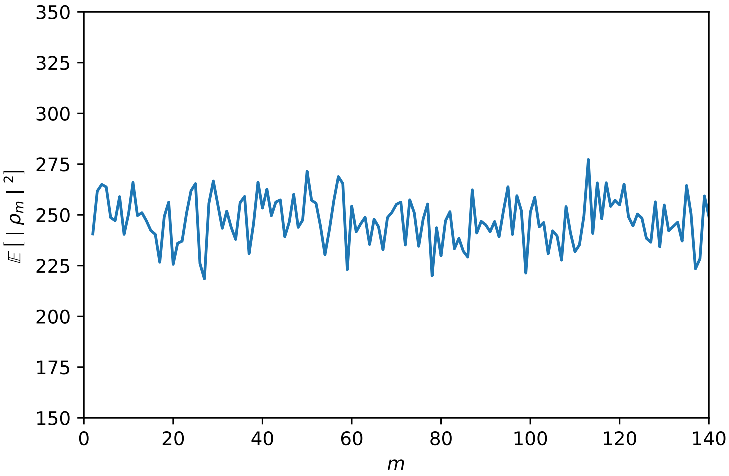

FIGURE 3.6: The disorder-averaged form factor for $h = 0.01$, $N = 8$, and 400 disorder realisations, illustrating the localised phase with its flat form factor indicative of Poisson statistics.

3.4 Conclusions

We have verified that the short-time expansion of the form factor for the ergodic phase of the stroboscopic QREM is in agreement with that of RMT. Based on the analogy with quantum graphs, we would expect that higher-order terms in the expansion to also match those of RMT, since the form factor calculation for quantum graphs has been extended to all orders [120, 127]. The work of Kos et al. [1] is consistent with this, where the second-order term in τ was also found, essentially a calculation of the Sieber-Richter orbit pairs [128], and found to be in accordance with the RMT result. One caveat we have yet to mention is that although it is true to say that quantum graphs are 'semiclasically exact' in that their exact density of states is given by a trace formula, the periodic-orbit calculation (or rather, the approximation known as the 'loop expansion' that identifies a well-defined set of periodic orbits [72]) still suffers from the restriction that it breaks down at the Heisenberg time $\tau = 1$; one practical way around this is to make t_{H} arbitrarily large by considering larger $|B|$, but a more elegant answer comes from the application of the supersymmetric nonlinear sigma model, the same in spirit as the ballistic sigma model mentioned in Chapter 1 that enabled the computation of the weak-localisation correction to RMT spectral statistics [61], which is capable of reproducing the exact RMT form factor for arbitrary τ [75, 120, 129]. Lastly, we might wonder whether we can push periodic-orbit theory further and describe weak localisation in the same fashion – unfortunately, given its failure to do so in the semiclassical approach to quantum chaotic Hamiltonians, the same problems (in particular, how to account for Hikami boxes in this framework is unknown [4]) can be expected to arise [131].

---

[4] The first-order correction to the conductance can be obtained semiclassically owing to the fact that no Hikami box is required [130].

Chapter 4

Quantum random energy model with a random kinetic term

In Chapter 2, diagrammatic calculations for simple observables in the QREM quickly became intractable: unlike the conductivity calculation for a single particle in a random potential discussed in Chapter 1, we found that we had to consider Hikami boxes, admittedly only an inconvenience, and more seriously, that diffuson-cooperon diagrammatics break down in the diffusive regime. Although weak localisation for a single-particle has been tackled in nondiffusive regimes, there was no natural way to extend these approaches to the QREM.

One way to proceed was to seek a new method of attack; this was our approach in Chapter 3 where we adopted semiclassical techniques developed in the context of quantum chaos. Here we reprise our original formalism of diagrammatic perturbation theory, but do so for a simplified version of the QREM for which the physically relevant subset of diagrams can be comfortably handled analytically for a kinetic term of arbitrary strength. The model is still a QREM in the sense that it consists of an REM plus a term generating quantum dynamics on the hypercube of 2^N spin states, but with the difference that the kinetic term, a uniform transverse field, is replaced by a *random* kinetic term, that is, an REM in a rotated basis. Averaging over both terms in the Hamiltonian facilitates a greatly simplified diagrammatic analysis; integrals over resolvents are eliminated and we are left with an essentially combinatorial problem – this gives us good reason to anticipate that an exact calculation is possible, which we indeed find to be the case.

4.1 Model

The model we shall study consists of N spin-1/2 degrees of freedom with Hamiltonian

$$H = \overbrace{\sum_{z\in\mathbb{Z}_2^N} V(z)\left|z\right\rangle\left\langle z\right|}^{V} + \overbrace{\sum_{x\in\mathbb{Z}_2^N} T(x)\left|x\right\rangle\left\langle x\right|}^{T}, \tag{4.1}$$

where, adopting the notation of Chapter 2, $|z\rangle$ are the eigenstates of $\bigotimes_{i=1}^N \sigma_i^z$ and similarly for $|x\rangle$, and $V(z), T(x)$ are uncorrelated zero-mean Gaussian random variables with respective variances γ_V, γ_T. This is the sum of two random energy models, where one has been rotated into the Fourier basis by Walsh-Hadamard transform.

4.2 Spectral statistics

Unlike the stroboscopic model considered in the preceding chapter, the average density of states is not a constant and so to explore level statistics, we must either unfold the spectrum or else use ratios of level spacings. To quickly assess the behaviour of the model, it suffices for our purposes to use the latter approach and calculate the ratios

$$r^n = \frac{\min(\delta^n, \delta^{n+1})}{\max(\delta^n, \delta^{n+1})}, \tag{4.2}$$

where $\delta^n = E_n - E_{n-1}$ are the nearest-neighbour level-spacings, which we then average over both an energy window and multiple disorder realisations to give the quantity we denote $[\bar{r}]$. This statistic has been shown to take the value $[\bar{r}] \approx 0.39$ in the localised phase, and $[\bar{r}] \approx 0.53$ in an ergodic phase with unbroken time-reversal symmetry. In Fig. 4.1 we evaluate $[\bar{r}]$ from $N = 10$ exact diagonalisation data and for fixed γ_z identify ergodic and localised phases as γ_x is varied, as well as quite a wide crossover region (expected for the small system size we use) of intermediate statistics. If we look at a larger energy interval (rather than only close to the band centre as in Fig. 4.1), we are just about able to see evidence of the many-body mobility edge (see Fig. 4.2).

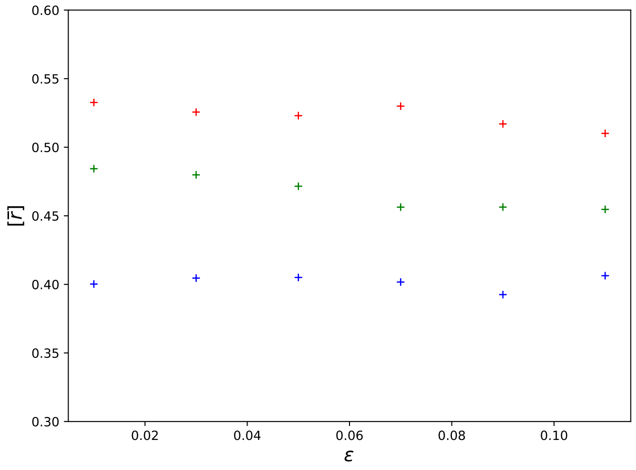

FIGURE 4.1: The energy-resolved (ϵ is the energy density) averaged level-spacing ratio for $\chi = 4$ (red), 0.3 (green), and 0.01 (blue) calculated for $N = 10$ and 50 realisations, revealing GOE, intermediate, and Poisson statistics respectively. The parameter χ controls the scales of the x and z variances according to: $\gamma_z = 1$ and $\gamma_x = 2^{-N}\chi\gamma_z$. Due to the symmetry between x and z in the Hamiltonian, if χ was sufficiently increased, Poisson statistics would once again be observed (localisation in the x-basis rather than the z-basis).

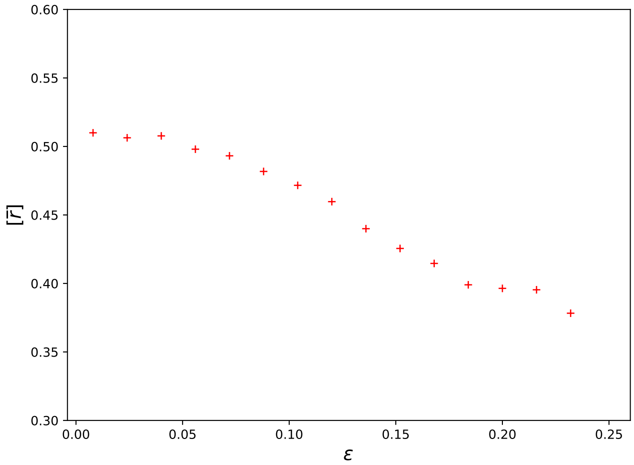

FIGURE 4.2: The averaged level-spacing ratio is plotted for $\chi = 1$ (notation as in Fig. 4.1) for $N = 12$ and 100 realisations over a larger energy interval, revealing an interpolation between GOE at the centre and Poisson statistics at the edge of the band.

The model (4.1), which interpolates between Poisson and Wigner-Dyson statistics, bears some resemblance to the Rosenzweig-Porter model [132, 133]

$$H = D + \frac{\lambda}{n^{\alpha}} G, \tag{4.3}$$

consisting of a superposition of a random diagonal matrix D (i.e. an REM) and a random matrix draw from the GOE or GUE, both matrices of size $n \times n$. The exponent α controls the behaviour of the model in the thermodynamic limit: the form factor is Poissonian for $\alpha > 1$, of Wigner-Dyson form for $\alpha < \frac{1}{2}$, shows a crossover region of intermediate statistics for $\frac{1}{2} < \alpha < 1$, and critical statistics at the transitions at $\alpha = 1/2$ (localisation transition) and $\alpha = 1$ (ergodic-nonergodic metal transition) [54].

The difference in the model we study is that the two matrices we are mixing would individually show Poisson statistics (i.e. they are localised in either the z- or the x-basis), and we expect a delocalised phase for some value of the mixing parameter. If we set $\gamma_z = 1$, numerical analysis of the averaged level-spacing ratio indicates that the transition occurs at a value of γ_x that scales to zero as $N \to \infty$, and so we would need to scale γ_x by some function of N if we wanted to identify a parameter that would tune through the transition in the thermodynamic limit.

4.3 Perturbation theory

Following Chapter 2, we develop a perturbative expansion in H for the resolvent

$$R(\epsilon) = \frac{1}{\epsilon - V - T + i\delta} = R^{(0)}(\epsilon) + R^{(0)}(T+V)R^{(0)} + \cdots, \tag{4.4}$$

with the bare resolvent now taking the trivial form $R^{(0)}(\epsilon) = (\epsilon + i\delta)^{-1}$. This can be expressed diagrammatically in the usual way, with the difference that we need two types of vertex for scattering by V or T. We note that the Rosenzweig-Porter model mentioned above has been treated via a resolvent perturbation theory, though it differs significantly from our strategy in Chapter 2 in that it is a locator expansion (i.e. a perturbation theory around the localised phase) [134].

The disorder-averaged resolvent can be expressed in terms of a self-energy $\Sigma(\epsilon)$

$$\mathbb{E}[R(\epsilon)] = \frac{1}{\epsilon - \Sigma(\epsilon)}. \tag{4.5}$$

Diagrammatically, $\Sigma(\epsilon)$ contains all one-particle irreducible diagrams with disorder lines of the same type tied together in pairs, where each pair is associated with a factor of γ_V or γ_T. As for the case of a single particle in a random potential and the QREM, we now argue that a noncrossing approximation holds for large N: diagrams in which V and T lines cross are suppressed by a factor of 2^{-N}.

4.3.1 Noncrossing approximation

It is easy to see that for diagrams consisting only of one type of line, the uncrossed and crossed diagrams of a given order contribute equally: each diagram of order m (in γ_a; $a = T, V$) is proportional to the identity with weight $\gamma_a^m/\epsilon^{2m-1}$. However, we shall now consider diagrams containing both V and T lines ('mixed diagrams'), such as those of order $\gamma_V\gamma_T$ shown in Fig. 4.3.

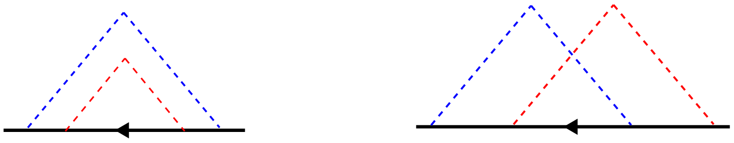

FIGURE 4.3: Uncrossed (left) and crossed (right) mixed self-energy diagrams, where V and T lines are coloured blue and red respectively.

Computing first the value of the uncrossed self-energy diagram in Fig. 4.3

$$\begin{aligned}\frac{\epsilon^3}{\gamma_V\gamma_T}\Sigma_{\text{uc}}(\epsilon) &= \sum_{\substack{z_1,x_2\\x_3,z_4}} |z_1\rangle\langle z_1|x_2\rangle\langle x_2|x_3\rangle\langle x_3|z_4\rangle\langle z_4|\,\delta_{z_1,z_4}\delta_{x_2,x_3}\\ &= \sum_{z_1,x_2} 2^{-N}|z_1\rangle\langle z_1| = \mathbb{1},\end{aligned} \tag{4.6}$$

whereas for the crossed diagram we find

$$\begin{aligned}\frac{\epsilon^3}{\gamma_V\gamma_T}\Sigma_{\mathrm{cr}}(\epsilon) &= \sum_{\substack{z_1,x_2\\x_3,z_4}} |z_1\rangle\langle z_1|x_2\rangle\langle x_2|z_3\rangle\langle z_3|x_4\rangle\langle x_4|\,\delta_{z_1,z_3}\delta_{x_2,x_4}\\ &= \sum_{z_1,x_2} 2^{-N}|z_1\rangle\langle z_1|x_2\rangle\langle x_2| = \frac{1}{2^N}\mathbb{1},\end{aligned} \tag{4.7}$$

where in each case we have exploited the fact that $|\langle z|x\rangle|^2 = 2^{-N}$. So, we find that the crossed diagram is suppressed by a factor of 2^{-N} relative to the uncrossed diagram, and are therefore justified in neglecting self-energy diagrams containing crossings between V and T lines in the large-N limit.

We are able to compute the resolvent self-energy in this noncrossing approximation – a generalised self-consistent Born approximation (SCBA) – by means of the self-consistent scheme shown below

$$\begin{aligned}\frac{1}{\epsilon-\Sigma_V-\Sigma_T} &= \mathbb{E}_T\left[\frac{1}{\epsilon-\Sigma_V-T}\right]\\ \frac{1}{\epsilon-\Sigma_V-\Sigma_T} &= \mathbb{E}_V\left[\frac{1}{\epsilon-\Sigma_T-V}\right],\end{aligned} \tag{4.8}$$

where the SCBA self-energy is given by $\Sigma_{\mathrm{SCBA}} = \Sigma_V + \Sigma_T$, and Σ_V (Σ_T) consists of all diagrams starting and ending with a V (T) line and containing no crossings between the V and T lines.

If we temporarily neglect the T term, we have

$$\frac{1}{\epsilon-\Sigma_V} = \mathbb{E}\left[\frac{1}{\epsilon-V}\right], \tag{4.9}$$

which can be computed exactly as the Stieltjes transform of the Gaussian

$$\mathbb{E}\left[\frac{1}{\epsilon-V+i\delta}\right] = \frac{\mathbb{1}}{\sqrt{2\pi\gamma_V}}\int_{-\infty}^{\infty}\frac{e^{-v^2/2\gamma_V}}{\epsilon-v+i\delta}\,\mathrm{d}v = \sqrt{\frac{2}{\gamma_V}}F\left(\frac{\epsilon}{\sqrt{2\gamma_V}}\right) - i\sqrt{\frac{\pi}{2\gamma_V}}e^{-\epsilon^2/2\gamma_V}, \tag{4.10}$$

where $F(z)$ is the Dawson function. More generally (i.e. for $z\in\mathbb{C}$), we have

$$\mathbb{E}\left[\frac{1}{z-V}\right] = \frac{\mathbb{1}}{\sqrt{2\pi\gamma_V}}\int_{-\infty}^{\infty}\frac{e^{-v^2/2\gamma_V}}{z-v}\,\mathrm{d}v = -i\sqrt{\frac{\pi}{2\gamma_V}}w\left(\frac{z}{\sqrt{2\gamma_V}}\right), \tag{4.11}$$

where

$$w(z) = \frac{i}{\pi}\int_{-\infty}^{\infty}\frac{e^{-t^2}}{z-t}\,\mathrm{d}t \tag{4.12}$$

is the Faddeeva function. For concision we absorb numerical factors by defining a scaled Fadeeva function

$$\mathcal{R}(z) \equiv -i\sqrt{\frac{\pi}{2}}w(z), \tag{4.13}$$

such that

$$\mathbb{E}\left[\frac{1}{z-V}\right] = \frac{1}{\sqrt{\gamma_V}}\mathcal{R}\left(\frac{z}{\sqrt{2\gamma_V}}\right). \tag{4.14}$$

4.4 Density of states

We are able to solve the self-consistent equations (4.8) numerically and thus determine the SCBA self-energy and resolvent. The natural physical quantity to extract is the (averaged) density of states

$$\nu(\epsilon) = -\frac{1}{\pi}\,\mathrm{Im}\,\mathrm{tr}\left(\mathbb{E}[R(\epsilon)]\right) = -\frac{2^N}{\pi}\frac{\Sigma''}{(\epsilon-\Sigma')^2+\Sigma''^2}, \tag{4.15}$$

where $\Sigma' = \mathrm{Re}[\Sigma(\epsilon)]$ and $\Sigma'' = \mathrm{Im}[\Sigma(\epsilon)]$. The SCBA density of states is found to closely reproduce the exact diagonalisation result for $N = 13$ spins (see Fig. 4.4). The effect of the random kinetic term on the density of states is a small departure from the Gaussian form of the REM density of states as γ_T is increased from zero; we plot only the case of $\gamma_V = \gamma_T$, where non-Gaussianity is maximal.

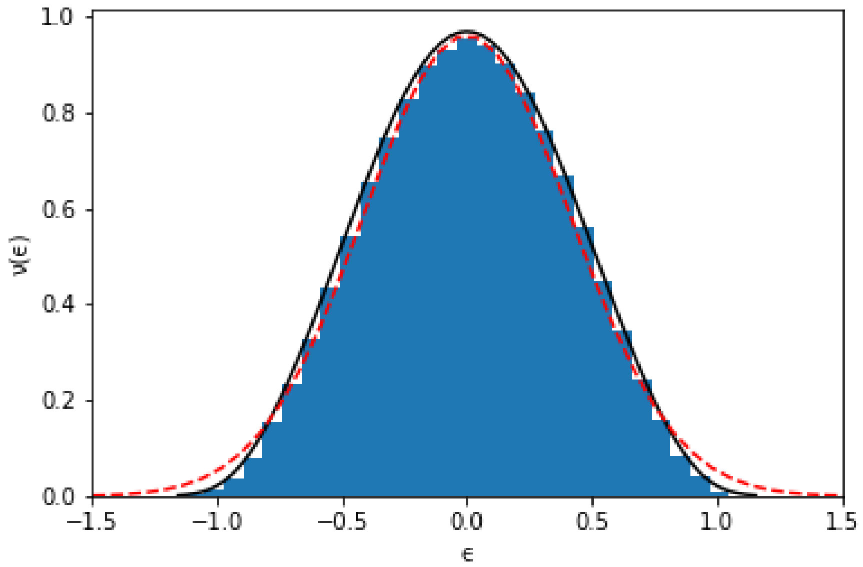

FIGURE 4.4: A comparison of the density of states for $N = 13$ spins and $\gamma_V = \gamma_T$ found by: a) exact diagonalisation (blue) and b) numerically exact solution of the self-consistent equations (black). A Gaussian fit (red) is also shown to illustrate the departure from the Gaussian density of states of the REM.

4.5 Binary disorder

Do the self-consistent equations (4.8) hold for non-Gaussian disorder? If the disorder is uncorrelated such that higher moments of the potential take the form $\mathbb{E}[V_{z_1}\dots V_{z_n}] \propto \prod_{i=1}^{n-1}\delta_{z_i,z_{i+1}}$ (and similarly for T) in diagrams describing n-tuple scattering, then diagrams with $V-T$ crossings are suppressed. This suggests that the self-consistent equations will remain the same, with the only change being the probability distribution with respect to which the expectation is taken.

The freedom to explore non-Gaussian disorder facilitates two things: firstly, we can look for a distribution which will reveal a sharper distinction in the density of states between the localised and delocalised regimes, and secondly, we can choose a simpler disorder distribution that will enable analytic solution of the self-consistent equations. In fact, both these objectives can be attained with a single choice: binary disorder, for which the simplest case to consider is a symmetric two-point distribution, $p(x) = \frac{1}{2}\left(\delta(x-\gamma)+\delta(x+\gamma)\right)$ [1]. For simplicity, we begin with the equal disorder width γ for the V and T distributions, for which we expect to see the maximum departure in the density of states from that of the pair of delta functions of a single binary REM. In this case, equations 4.8 reduce to the single equation

$$\frac{1}{\epsilon-\Sigma} = \frac{1}{2}\int_{-\infty}^{\infty}\frac{\delta(V+\gamma)+\delta(V-\gamma)}{\epsilon-\frac{\Sigma}{2}-V}\,dV \tag{4.16}$$

$$= \frac{\epsilon-\frac{\Sigma}{2}}{(\epsilon-\frac{\Sigma}{2})^2-\gamma^2}. \tag{4.17}$$

The solution, $\Sigma(\epsilon) = \epsilon \pm \sqrt{\epsilon^2-4\gamma^2}$, can be inserted into (4.15) to give a density of states

$$\nu(\epsilon) \propto \frac{1}{\sqrt{4\gamma^2-\epsilon^2}}, \tag{4.18}$$

whose characteristic singularity is captured well by the exact diagonalisation result shown in Fig. 4.5. Since the exact diagonalisation results are shown for a single realisation, one may wonder why the plots appear to be perfectly symmetric – this reflects rapid convergence to the large-N distribution; for the Gaussian disorder case, signs of asymmetry can just about be seen for $N = 8$. Although our exact calculation is for the average density of states, convergence in expectation in RMT can usually be extended to almost sure convergence by appealing to concentration of measure results [136]. We shall see that this is the case for the problem at hand in the next section, when we give a free probability interpretation of the calculation.

If we now introduce an $x - z$ asymmetry such that $\gamma_V \neq \gamma_T$ i.e. the symmetric two-point distributions for V and T are of different width, a gap opens (for arbitrarily small asymmetry) in the density of states at $\epsilon = 0$ as shown in Fig. 4.6. Since the noncrossing calculation gives a large-N result, this is a gap that is predicted to exist in the thermodynamic limit.

The SCBA equations continue to hold if we take an asymmetric two-point distribution i.e. $p(x) = \left(p_R\delta(x-a)+p_L\delta(x+a)\right)$, where $p_R + p_L = 1$ (see Fig. 4.7). The self-energy is given by $\Sigma(\epsilon) = \frac{1}{2}\left(\Delta+2\epsilon\pm 2\sqrt{\epsilon^2+\frac{\Delta^2}{4}-4a^2}\right)$ where $\Delta = 8a\left(p_R-\frac{1}{2}\right)$, and thus the density of states is

$$\nu(\epsilon) \propto \frac{\sqrt{4a^2-\kappa-\epsilon^2}}{\kappa+(4a^2-\kappa-\epsilon^2)}, \tag{4.19}$$

---

[1] Extending the proof of Anderson localisation in one dimension to include binary disorder was in fact a more challenging problem rather than a simplification [135].

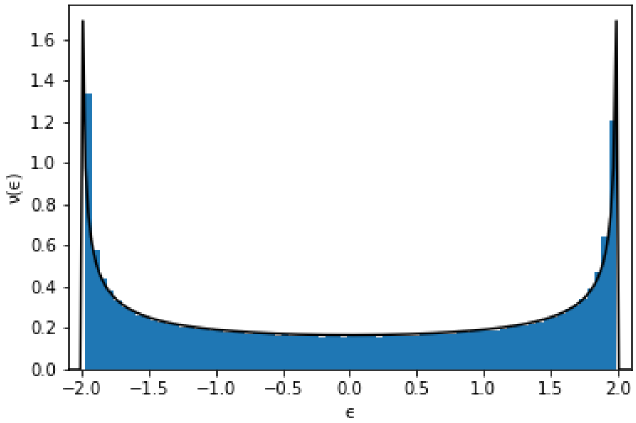

FIGURE 4.5: A comparison of the density of states when $V(z)$ and $T(x)$ are drawn from a symmetric two-point distribution for $N = 13$ spins. As for the Gaussian case we compare: a) exact diagonalisation (blue histogram) and b) exact solution of the self-consistent equations (black line).

for $\kappa = \Delta^2/4$.

4.6 Free probability

In this section we will establish a connection between our results for the density of states in the random kinetic QREM and free probability theory: in the large-N limit, the terms in the Hamiltonian (4.1) become freely independent random variables, whence their joint distribution may be computed using the R-transform of free probability. To elucidate these remarks, we make a diversion in order to introduce the central idea of free probability: free independence (below, we shall generally follow Refs. [137, 138] for definitions).

4.6.1 Free independence

Modern (measure-theoretic) probability theory begins with the definition of the probability space $(\Omega, \mathcal{F}, \mathbb{P})$, consisting of a sample space Ω, a σ-algebra of events $\mathcal{F}$ on Ω, and a probability measure $\mathbb{P}$ on $\mathcal{F}$. However, one can take an alternative view point by abstracting away the algebra of events and considering instead the algebra of measurable functions on the Ω (i.e. random variables) equipped with a linear functional induced by $\mathbb{P}$ (i.e. the expectation). It is in this language that we can naturally formulate the notion of noncommutative probability theory – by allowing the algebra of random variables to be noncommutative – which in turn enables us to introduce free independence as the natural analogue of classical independence in the noncommutative setting [136]. Free independence cannot occur (nontrivially) for commuting variables, so this complication is essential.

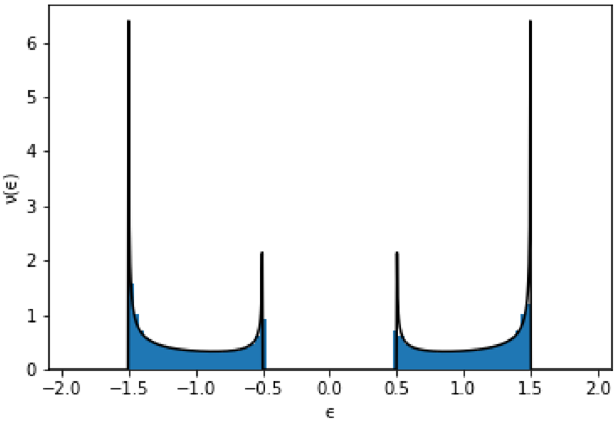

FIGURE 4.6: A comparison of the density of states when $V(z)$ is drawn from a symmetric two-point distribution of twice the width of the $T(x)$ distribution; exact diagonalisation for $N = 13$ spins (blue) is compared to exact solution of the SCBA equations (black).

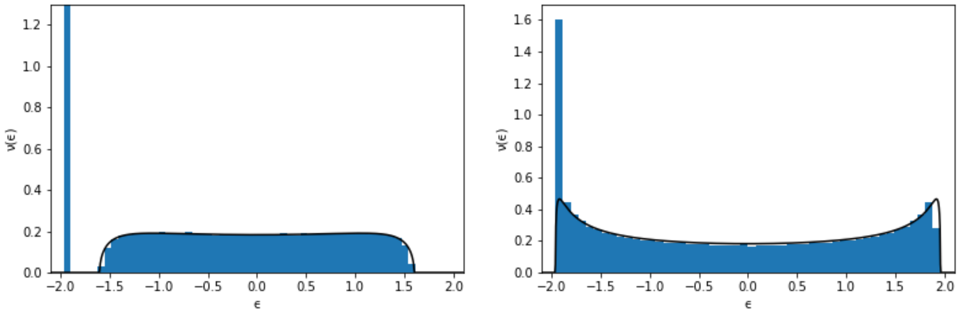

FIGURE 4.7: The density of states for binary disorder ($\gamma_V = \gamma_T$) with an asymmetric two-point distribution with weights (left) $p_R = 0.8, p_L = 0.2$ and (right) $p_R = 0.6, p_L = 0.4$; $N = 13$ exact diagonalisation (blue) is compared to numerical solution of the SCBA equations (black).

Definition. *Let* $(\mathcal{A}, \tau)$ *denote a noncommutative probability space, described by the unital algebra* $\mathcal{A}$ *and linear functional* $\tau : \mathcal{A} \to \mathbb{C}$ *(with* $\tau(\mathbb{1}) = 1$*). The unital subalgebras* $(\mathcal{A}_i)_{i\in I} \subset \mathcal{A}$ *are said to be* ***freely independent*** *(or simply "free") if* $\tau(a_1 \dots a_m) = 0$ *(*$m \in \mathbb{Z}^+$*) whenever*

1. $a_j \in \mathcal{A}_{i(j)}$ *for* $i : \mathbb{Z}^+ \to I$
2. $\tau(a_j) = 0 \; \forall j$
3. $i(1) \neq i(2), i(2) \neq i(3), \dots, i(m-1) \neq i(m)$.

The random variables a_j *are said to be free if the unital subalgebras generated by* $\{\mathbb{1}, a_j\}$ *are free.*

This can be compared to the more straightforward definition of classical independence in the algebraic framework, which is simply the factorisation property of the expectation: $\tau(a_1 \dots a_m) = \prod_i \tau(a_i)$. In fact, this suggests a more helpful definition of free independence as a rule for how mixed moments can be expanded in terms of sums of products of the moments of individual random variables. For instance, we can find the formula for $\tau(X^m Y^n)$ by using the definition above to write down

$$\tau\left[(X^m - \tau(X^m)\mathbb{1})(Y^n - \tau(Y^n)\mathbb{1})\right] = 0, \tag{4.20}$$

which upon expansion yields the factorisation law $\tau(X^m Y^n) = \tau(X^m)\tau(Y^n)$, just as for classical independence. However, to see that free independence is indeed a different definition, one needs to consider more general mixed moments for which the noncommutativity of the algebra is important, for instance $\tau(XYXY)$, which is found to satisfy

$$\tau(XYXY) = \tau(X^2)\tau(Y)^2 + \tau(X)^2\tau(Y^2) - \tau(X)^2\tau(Y)^2. \tag{4.21}$$

An important consequence of classical independence is that that for independent random variables X, Y, the distribution of $Z = X + Y$ is given by the convolution of the probability density functions of X and Y. The natural way to compute these convolutions is in terms of the characteristic function $\phi_Z(t) = \mathbb{E}[e^{itZ}]$:

$$\begin{aligned} \mathbb{E}[e^{it(X+Y)}] &= \mathbb{E}[e^{itX}e^{itY}] && (4.22)\\ &= \phi_X(t)\phi_Y(t), && (4.23) \end{aligned}$$

where the second line follows by independence of X and Y. What is the analogous operation for freely independent random variables, termed free convolution of the probability densities, and the analogue of the characteristic function (i.e. the Fourier transform of the probability density function, when the latter exists)? The analogue of the characteristic function turns out to be the analytic part of the inverse Stieltjes transform, known as the R-transform, which satisfies the additivity property

$$\mathcal{R}_{X+Y}(z) = \mathcal{R}_X(z) + \mathcal{R}_Y(z), \tag{4.24}$$

for X, Y freely independent. The R-transform is most conveniently defined in terms of the Stieltjes transform $\mathcal{S}_X(z) = \tau((z - X)^{-1})$ through the implicit functional relation [139, 140]

$$\mathcal{R}_X\left[\mathcal{S}_X(z)\right] + \frac{1}{\mathcal{S}_X(z)} = z. \tag{4.25}$$

We shall omit any discussion of how the R-transform can be actually evaluated (see for instance Ref. [138]) in the case of interest, since we shall find that we have already done so under a different name.

4.6.2 Connection to random matrix theory

After Voiculescu had first introduced the concept of freeness in the context of operator algebras [139], he observed that the Wigner semicircle distribution played an important role (in fact, it is the "free" analogue of the Gaussian in the free central limit theorem), which hinted that there might be a connection to random matrix theory, where the Wigner semicircle is the universal limit distribution for the spectral density for a number of Hermitian $N \times N$ independent-entry random matrix ensembles as $N \to \infty$. In the large-N limit, many classes of independent random matrices become freely independent with respect to a unital linear functional given by the normalised trace $\tau(\ldots) := \frac{1}{N}\operatorname{tr}(\ldots)$ [141]. The particular theorem of interest to us is the following [138, 142]

Theorem. *Let* $\{A_N\}$, $\{B_N\}$ *be sequences of* $N \times N$ *random matrices with convergent empirical spectral measures* $\mu_N^{A(B)} \xrightarrow[N\to\infty]{a.s.} \mu^{A(B)}$, *and* $\{U_N\}$ *a sequence of* $N \times N$ *Haar random unitary matrices, then* $A_N, U_N B_N U_N^\dagger \xrightarrow[N\to\infty]{d} A, B$ *where* A, B *are freely independent random variables with distributions* μ^A, μ^B *respectively.*

Roughly speaking, provided the eigenspaces of a set of random matrices are in generic positions with respect to another, then we expect them to be asymptotically free; this intuition is clearest in the deterministic limit in which A_N, B_N are constant matrices. At last, we have set out all we need in order to make the connection to our density of states calculation for the random kinetic QREM. Interpreted as a random matrix model, (4.1) is the sum of a random diagonal matrix, and a second, independent random diagonal matrix (where we consider the case that it is drawn from the same distribution, but with possibly different parameters) that has been rotated into a new basis by a deterministic unitary transformation (Walsh-Hadamard transform). Importantly, the asymptotic freeness result above can be strengthened from convergence in distribution, to almost sure convergence [141, 143]. The important consequence of this is that, for large-N, we expect the result to hold at the level of a single realisation. So, we expect the two terms in H in (4.1) to be asymptotically free for large-N, such that the spectral density of H, for a single realisation, is given by the free convolution of the V and T disorder distributions. We note that a similar approach has been adopted in Refs. [144, 145], where an Anderson Hamiltonian is split into a sum of two terms, rotating one of the terms to give a free approximant to the Hamiltonian, and then computing the free convolution to find an approximation to the density of states, which could then be compared to exact diagonalisation results for the original Hamiltonian.

For the case of binary disorder, we are able to analytically corroborate our earlier result for the density of states using the free probability approach, for it is a well known result that the free convolution of two Bernoulli distributions is the arcsine distribution we obtained in (4.18). Our calculation of the self-energies Σ_V and Σ_T corresponds to the computation of the R-transforms, writing down the SCBA resolvent then gives us the Stieltjes transform of the probability density for the sum of two Bernoulli variables, from which we finally obtain the density of states by the Stieltjes inversion formula (4.15). Of course, this is general and holds for arbitrary disorder distribution, though in most cases the density of states will not have a simple analytic form as it does here.

As well as this mathematical connection, one may wonder if we can further elucidate the connection between the SCBA self-energy and the R-transform. A combinatorial formulation of free probability has established that the R-transform should be understood as a free-cumulant generating function. For classical random variables X_i, we have the combinatorial formula for the moments in terms of the cumulants κ [2]

$$\mathbb{E}[X_1 \dots X_n] = \sum_{\sigma \in \mathcal{P}_n} \prod_{b \in \sigma} \kappa(X_j | j \in b), \tag{4.26}$$

where $\mathcal{P}_n$ is the set of all partitions of $[n] = \{ 1, 2, \dots, n \}$. The analogous result for free random variables is obtained by restricting the summation to only the noncrossing partitions [140]: if one diagrammatically represents a partition σ of the ordered set $[n]$ by connecting integers belonging to the same subset $b \in \sigma$, the noncrossing partitions are those in which no lines cross.

4.7 Single-particle analogue

We originally approached the QREM in Chapter 2 by making an analogy to a single particle in a random potential. Having considered a modified QREM in this chapter, we may ask about the corresponding modification in the single-particle problem: an Anderson model with a random kinetic energy.

Consider a single particle in one dimension, with position x ($0 \leq x \leq L$) and momentum k, moving in a random potential $V(x)$ with a random momentum-space 'potential' $T(k)$ replacing the kinetic energy

$$H = \sum_x V(x) \left| x \right\rangle \left\langle x \right| + \sum_k T(k) \left| k \right\rangle \left\langle k \right|, \tag{4.27}$$

where $V(x), T(k)$ are again distributed according to uncorrelated zero-mean Gaussians with respective variances γ_V, γ_T.

4.7.1 Density of states

If we compare the uncrossed and crossed self-energy, we find that the argument for the suppression of crossed diagrams in (4.6) and (4.7) goes through in the same way, with the exception that the inner product $\langle x|k \rangle = L^{-1/2} e^{ikx}$ appears instead of $\langle x|z \rangle = 2^{-N/2} \prod_j [1 - \frac{1}{2}(x_j - 1)(z_j - 1)]$, which means that the crossed self-energy diagrams is smaller by a factor of L instead of 2^N. Otherwise, the density of states calculation is the same and so our results for N spins could equally be thought of as arising from the single-particle version of the model in a one-dimensional system of length $L = 2^N$. However, there is not a duality between the two models as can be seen by the difference in structure that appears at the level of two-particle correlations (see the second half of Appendix C).

---

[2] We note that Wick's theorem follows from this result in the case of Gaussian random variables.

4.8 Conclusions

Our fundamental achievement in this chapter has been the exact calculation of the density of states for the Hamiltonian (4.1), a QREM in which the kinetic term has itself been replaced by an REM in the Fourier basis. We proceeded by developing a diagrammatic perturbation theory for the resolvent, finding that a generalisation of the self-consistent Born approximation that appears in the single-particle theory of weakly disordered disordered metals becomes exact in the thermodynamic limit. Upon noting that our result holds for arbitrary disorder distribution and finding an arcsine form of the density of states in the case of Bernoulli distributions of equal variance, we were led to the realisation that our Hamiltonian is a random matrix model whose large-N limit describes the sum of freely independent random variables.

Having made the connection to free probability, one can ask to what extent we can use the native techniques of this field to analyse (4.1). We have begun to pursue this programme by reinterpreting the density of states diagrammatics as an R-transform computation. Since the calculation of two-particle correlation functions in our diagrammatic framework quickly becomes cumbersome, generating a two-particle vertex function that is difficult to analyse (see Appendix C), one might wonder whether free probability can help here. Whilst the notion of freeness was required to access the average spectral density, the appropriate concept that facilitates the treatment of eigenvalue correlations is that of second-order (and higher-order) freeness [138]. Exploring this connection is a worthwhile task for future work.

Part II

Noisy spins

Chapter 5

Noisy spins and the Richardson–Gaudin model

At this point we shall change tack: in the present chapter and the next we shall be looking at many-body systems with dynamical noise instead of quenched disorder. This chapter will be concerned with a system of noninteracting spins (qubits) coupled to a common noisy environment, with each spin precessing at its own frequency – a situation reflecting inhomogeneity in the splittings of a set of qubits. The correlated noise that the spins experience, which incidentally is another feature that sets this chapter apart from the others which treat only uncorrelated disorder and noise, is found to give rise to long-lived correlations that relax only due to the differing frequencies. Our main achievement is to prove that the problem can be mapped onto a non-Hermitian integrable Richardson–Gaudin model in the high-temperature limit, enabling us to draw upon a Bethe ansatz solution to find the exact spectrum of the quantum master equation and hence determine the relaxation rate of the spin correlations. Integrable quantum master equations are relatively scarce and to be contrasted with the typical situation, exemplified by the Liouvillian (2.123) we derived for the QREM, for which numerics and perturbation theory are all we have at our disposal. By their very nature, integrable models are fine-tuned, but an interesting feature that we encounter here is that a set of random variables, the qubit splittings, enter as free parameters and not as integrability-breaking terms.

5.1 Background and model

The coherence of a quantum system is limited by the strength and nature of its coupling to the environment. Often, an environment consisting of many degrees of freedom can be treated as a source of noise that subjects the system to random disturbances [146]. A central theme in quantum information science is high-fidelity preparation and manipulation of quantum states in the presence of such noise. There are essentially two categories of strategy to achieve this: actively encoding information in such a way that errors can be detected and corrected (quantum error-correcting codes [147]), or passively protecting information from disturbance in the first place. The latter includes, for instance, topological quantum computation in which both the qubits – spatially separated non-Abelian anyons – and the operations upon them –

braiding of these anyonic quasiparticles – are nonlocal and thus intrinsically insensitive to local perturbations [148]. However, the present work is connected to another passive approach in which subspaces of states where decoherence is absent or minimal (decoherence-free subspaces) arise due to noise correlations [149, 150].

The usual framework for the theoretical analysis of the open quantum systems described above is the quantum master equation (QME) for the system's density matrix ρ. Assuming Markovian dynamics, this may be written in Lindblad form [146]

$$\dot{\rho} = -i\,[H, \rho] + \sum_{\alpha} \left[L_\alpha \rho L_\alpha^\dagger - \frac{1}{2} L_\alpha^\dagger L_\alpha \rho - \frac{1}{2} \rho L_\alpha^\dagger L_\alpha \right], \tag{5.1}$$

where H is the system Hamiltonian, L_α are known as the Lindblad operators, and we set $\hbar = 1$.

Solving the master equation exactly for a large system is in general impossible. However, as with pure unitary dynamics described by the Schrödinger equation, we may ask whether there are examples of exact solutions that are nontrivial, physically motivated, and valid for a system of arbitrary size. There is a long history of master equations of *classical* stochastic processes being solved by methods developed for exactly solvable quantum models [151]. Surprisingly, very few examples of integrable QMEs – allowing for a complete determination of the spectrum of decay modes – may be found in the literature [152–155].

We shall present an exact solution of a model of N spins described by [156]

$$H = \sum_{j=1}^{N} \left[\Omega + \omega_j \right] s_j^z, \qquad L_z = \sqrt{g_0} \sum_j s_j^z, \quad \text{and} \quad L_\pm = \sqrt{g_\pm} \sum_j s_j^\pm. \tag{5.2}$$

This model describes precession of the individual spins at frequencies $\Omega + \omega_i$, representing unequal level splittings in a system of qubits. The L_α describe correlated coupling to the environment: L_z accounts for pure dephasing, while $L_\pm$ respectively describe excitation and decay of the spins. The three couplings $g_0, g_\pm$ depend on the spectral density of the environment at frequencies $0, \pm\Omega$. Detailed balance for an environment at temperature T implies $g_-/g_+ = e^{-\Omega/k_B T}$. We solve the model (5.2) exactly in the high-temperature limit when $g_+ = g_-$. This limit is relevant in a number of situations; as a representative sample, we cite superconducting qubits [157], photosynthetic light-harvesting complexes [158–160], and ion traps [161]. In a Rabi driven system, an infinite-temperature bath can arise as an effective description of a zero-temperature bath describing only spontaneous emission [162].

When $\omega_j = 0$ the components of the density matrix describing isotropic spin correlations are stationary, corresponding to degenerate zero eigenvalues of the Liouvillian. The exact solution allows us to calculate the spectrum of n-spin correlations when $\omega_j \neq 0$ for arbitrary n, a result which can only be obtained for moderate n by exact diagonalisation (see Fig. 5.1). When the ω_j are small, the decay rates have parametric form ω_j^2/g_+, showing that increasing noise reduces the decay rate, a manifestation of the quantum Zeno effect [163]. Although it is natural to interpret this in terms of second-order degenerate perturbation theory, it is not clear to us how

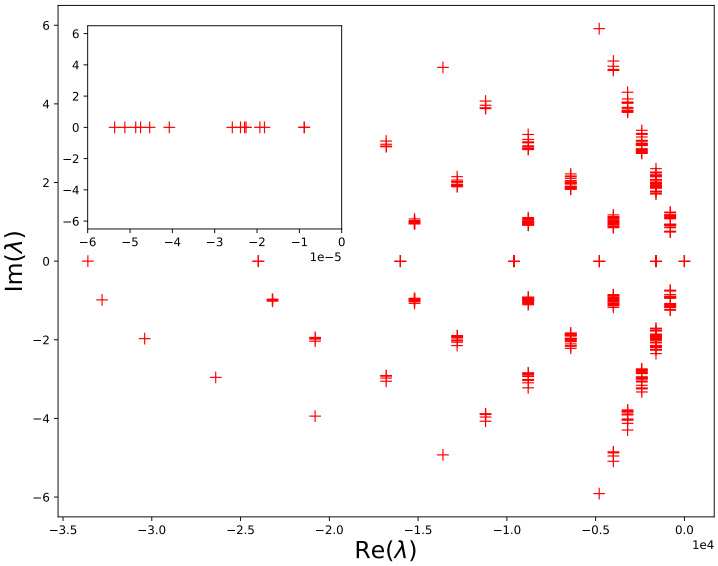

FIGURE 5.1: Spectrum of the Liouvillian (5.12) for $n = 6$ spin correlations for the case of $\Omega = 1, g_+ = 800$, $g_0 = 0$ and $\omega_i \sim \mathrm{Uni}(-0.2, 0.2)$ obtained by exact diagonalisation. The inset is a magnified view of a split multiplet of 15 states near zero. The spectrum is symmetric with respect to the real axis due to the PT-symmetry of the Liouvillian.

to actually perform such a calculation. Indeed, the first step – to resolve the degeneracy at $\omega_j = 0$ into an appropriate eigenbasis – is most effectively accomplished by the exact solution.

Solving (5.2) is possible because of the correlated coupling to the environment. Models of this type may be traced back to Dicke's paper [164, 165] on the spontaneous emission of atoms confined to a region smaller than the wavelength of the emitted light, and have appeared in many contexts since [156]. Dicke identified superradiant and subradiant states of the atomic ensemble, corresponding to states of maximum and minimum total spin. For $\omega_j = 0$ the QME may be written purely in terms of total spin, and the solution was found nearly fifty years ago [166–169]. For $\omega_j \neq 0$, however, the total spin does not commute with the Hamiltonian. Our solution proceeds via a mapping to a non-Hermitian version of the Richardson–Gaudin model [170].

5.2 Density matrix and correlation functions

The density matrix for a single spin-1/2 may be written

$$\rho^{(1)} = \frac{1}{2}\mathbb{1} + \mathbf{c}\cdot s \qquad (|\mathbf{c}| \leq 1), \tag{5.3}$$

where s denotes the vector of Pauli matrices, such that $|\mathbf{c}| = 1$ corresponds to pure states. More generally, a spin-s density matrix can be decomposed into a convex combination of spherical tensors $T_q^{(k)}$ according to [171]

$$\rho^{(1)} = \frac{1}{2s+1} \sum_{k=0}^{2s} \sum_{q=-k}^{k} c_q^k T_q^{(k)}, \tag{5.4}$$

where $T_q^{(k)}$ obey the following commutation relations with the the angular momentum operator J:

$$[J_z, T_q^{(k)}] = q T_q^{(k)} \quad \text{and} \quad [J_\pm, T_q^{(k)}] = \sqrt{(k \mp q)(k \pm q + 1)}\, T_{q\pm 1}^{(k)}. \tag{5.5}$$

For N spins ($s = 1/2$) we may write the density matrix as

$$\rho^{(N)} = \frac{1}{2^N} \sum_{\{a_j\}} c_{a_1 \cdots a_N} s_1^{a_1} \cdots s_N^{a_N}, \tag{5.6}$$

where $a_j = 0, x, y, z$, with $s^0 = \mathbb{1}$. The coefficients $c_{a_1 \cdots a_N}$ may be identified with the correlation functions of the spins

$$c_{a_1 \ldots a_N} = \mathrm{tr}\left[\rho^{(N)} s_1^{a_1} \cdots s_N^{a_N}\right]. \tag{5.7}$$

Note that $c_{0\ldots 0} = 1$ is required by normalisation of the density matrix. The reduced density matrix for any subsystem of spins is obtained by setting the indices for all spins in its complement to zero.

5.3 Mapping to the Richardson–Gaudin model

The equation of motion of $c_{a_1 \cdots a_N}$ may be found by substituting (5.6) into the QME. First, we note that for $g_+ = g_-$ we may write the Lindblad operators as

$$L_{x,y} = \sqrt{g_+} \sum_j s_j^{x,y}, \qquad L_z = \sqrt{g_0} \sum_j s_j^z. \tag{5.8}$$

Considering now the effect of one of the L_α and invoking the cyclic invariance of the trace we observe

$$\begin{aligned} &\sum_{j,k} \mathrm{tr}\left[s_k^\alpha \rho s_j^\alpha (\cdots) - \frac{1}{2}\{s_k^\alpha s_j^\alpha, \rho\}(\cdots)\right] = \frac{1}{2} \sum_{j,k} \\ &\mathrm{tr}\left[\rho\left(s_j^\alpha (\cdots) s_k^\alpha + s_k^\alpha (\cdots) s_j^\alpha \;\; -(\cdots) s_j^\alpha s_k^\alpha - s_j^\alpha s_k^\alpha (\cdots)\right)\right]. \end{aligned} \tag{5.9}$$

We also note the following identity

$$\begin{aligned} &s_j^\alpha s_j^{a_j} s_k^{a_k} s_k^\alpha + s_k^\alpha s_j^{a_j} s_k^{a_k} s_j^\alpha - s_j^{a_j} s_k^{a_k} s_j^\alpha s_k^\alpha - s_j^\alpha s_k^\alpha s_j^{a_j} s_k^{a_k} \\ &= -[s_j^\alpha, s_j^{a_j}][s_k^\alpha, s_k^{a_k}] \\ &= \sum_{b,c} \varepsilon_{\alpha a_j b}\, \varepsilon_{\alpha a_k c}\, s_j^b s_k^c = (\mathsf{T}^\alpha \boldsymbol{s}_j)^{a_j} (\mathsf{T}^\alpha \boldsymbol{s}_k)^{a_k}, \end{aligned} \tag{5.10}$$

where $(\mathsf{T}^\alpha)_{bc} = -\epsilon_{\alpha bc}$ are the generators of $\mathfrak{so}(3)$ in the adjoint representation. Since $\mathfrak{su}(2) \cong \mathfrak{so}(3)$, they can alternatively be thought of as generators of $\mathfrak{su}(2)$ in the adjoint representation.

If we switch to Hermitian Lie algebra generators, we can introduce spin-1 operators $\mathsf{S}^a_j = i\mathsf{T}^a_j$. After combining Eqs. (5.1),(5.9), and (5.10), we obtain the equation of motion for the correlator C (with tensor components defined by (5.7))

$$\partial_t \mathsf{C} = \mathcal{L}\mathsf{C}, \tag{5.11}$$

where the Liouvillian superoperator $\mathcal{L}$ takes the form of the non-Hermitian spin-1 Richardson-Gaudin model

$$\mathcal{L} = i\sum_{j=1}^{n}\left[\Omega + \omega_j\right]\mathsf{S}^z_j - g_+\sum_{j,k=1}^{n}\left(\mathsf{S}^x_j\mathsf{S}^x_k + \mathsf{S}^y_j\mathsf{S}^y_k\right) - g_0\sum_{j,k=1}^{n}\mathsf{S}^z_j\mathsf{S}^z_k. \tag{5.12}$$

Here n is the number of nonzero indices of C, which describe the reduced density matrix of the corresponding spins. The same model, involving a system of spins with $\mathsf{S}_j = 1, \ldots, 2s$, would arise for higher spin.

5.4 Equivalence to stochastic evolution

We can obtain the same result in a more robust and transparent fashion by regarding the high-temperature limit ($g_+ = g_-$) as a problem of stochastic evolution due to classical noise [172–178].

Consider N spins precessing in a common stochastic field, so that their evolution is governed by the Hamiltonian $H_\eta = \sum_{j=1}^{N} h_j(t)$, where

$$h_j(t) = \eta_x(t)s^x_j + \eta_y(t)s^y_j + \left[\Omega + \omega_j + \eta_z(t)\right]s^z_j, \tag{5.13}$$

and $\eta_j(t)$ describe Gaussian white noises with covariances $\mathbb{E}[\eta_z(t)\eta_z(t')] = g_0\delta(t-t')$ and $\mathbb{E}[\eta_x(t)\eta_x(t')] = \mathbb{E}[\eta_y(t)\eta_y(t')] = g_+\delta(t-t')$. The corresponding infinitesimal stochastic unitary evolution $U(t+dt,t) = e^{-idH_t}$ is generated by

$$dH_t = \sum_j(\Omega + \omega_j)s^z_j\,dt + \sum_{j,\alpha}\sqrt{g_\alpha}\,s^\alpha_j\,d\eta^\alpha_t, \tag{5.14}$$

where the white noise has been expressed as the differential of a Brownian motion $d\eta^\alpha$, from which it follows by Itô's lemma [1] that the density matrix ϱ_t satisfies the Itô stochastic differential equation

$$d\varrho_t = -\left(i[H,\varrho_t] + \frac{1}{2}\sum_\alpha[L_\alpha,[L_\alpha,\varrho_t]]\right)dt - i\sum_\alpha[L_\alpha,\varrho_t]\,d\eta^\alpha_t. \tag{5.15}$$

---

[1] Recall that if $f(t,B_t)$ is a function depending on a Brownian motion (Wiener process) B_t, then the differential is given by: $df = \partial_t f\,dt + \partial_{B_t} f\,dB_t + \frac{1}{2}\partial^2_{B_t} f\,dB^2_t + O(dt^{3/2})$. Ito's lemma follows upon applying the property of Brownian motion (in its ubiquitous shorthand form) that: $dB_t dB_t = dt$.

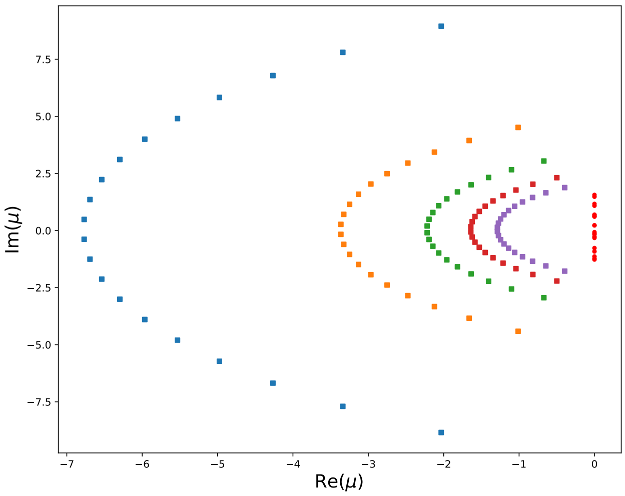

FIGURE 5.2: Bethe root distribution corresponding to the $\mathsf{S}^z_{\text{tot}} = 0$ eigenstate descended from the maximal S_{tot} state of the $\omega_i = 0$ model ($n = 20$). The curves of different colour correspond to different values of $1/g_+$ (increasing from left to right), and the ω_i are shown as red circles along the imaginary axis. One can see that S_{tot} is maximum by noting that all μ_i go to infinity as $1/g_+$ vanishes, and so from (5.19) the state is derived from $|\chi^-\rangle$ simply by raising $\mathsf{S}^z_{\text{tot}}$ to zero.

After averaging, $\rho = \mathbb{E}_\eta[\varrho]$ can be seen to satisfy the QME described by (5.2). However, we could alternatively consider the evolution of the correlation tensor C, which for *nonstochastic* η_j would be given by (5.11) with

$$i\mathcal{L}_{\text{ns}} = \sum_{j=1}^{n} \eta_x(t)\mathsf{S}^x_j + \eta_y(t)\mathsf{S}^y_j + \left[\Omega + \omega_j + \eta_z(t)\right]\mathsf{S}^z_j. \tag{5.16}$$

Whilst this could be seen by a direct algebraic argument, as done in the previous section, it is simpler to decompose the spin-1/2 density matrix into the spherical tensor basis and use the defining commutation relations (5.5): only the spin-1 ($T^{(1)}_q$) components survive (i.e. have nontrivial dynamics) and evolve according to the Liouvillian above. If we now consider stochastic η_j – by writing down the stochastic differential equation for dC and averaging (just as for the density matrix above) – we can see that the Itô terms (i.e. those proportional to $d\eta_\alpha(t)^2$) generate the spin-spin interaction in (5.12). We note that more detailed derivations of this kind shall be presented in the next chapter when we study operator spreading in noisy spin models.

5.5 Exact solution

As a prelude to the exact solution of (5.12), we first consider the much simpler case of $\omega_j = 0$ (and $g_0 = 0$) [2], such that the model reduces to

$$\mathcal{L} = i\Omega \mathsf{S}^z_{\text{tot}} - g\left[\mathsf{S}^2_{\text{tot}} - (\mathsf{S}^z_{\text{tot}})^2\right], \tag{5.17}$$

from which the spectrum can be obtained immediately. It consists of degenerate multiplets for given values of $(\mathsf{S}_{\text{tot}}, \mathsf{S}^z_{\text{tot}})$, with the multiplets of fixed S_{tot} lying on parabolas. In particular, states with $\mathsf{S}_{\text{tot}} = 0$ have exactly zero eigenvalue. For these states the tensor $c_{a_1 \ldots a_N}$ is *isotropic*. The simplest example is provided by $N = 2$, where the most general rotationally invariant density matrix (two-qubit Werner state) is

$$\rho^{(2)}_c = \frac{1}{4}\mathbb{1} + c_\bullet \mathbf{s}_1 \cdot \mathbf{s}_2, \qquad -1 \le c_\bullet \le 1/3, \tag{5.18}$$

corresponding to $c_{00} = 1$, and $c_{a_1 a_2} = 4c_\bullet \delta_{a_1,a_2}$ for $a_{1,2} = x, y, z$. Note that $c_\bullet = -1$ corresponds to a pure singlet state, but for larger N one cannot express the isotropic tensors only in terms of singlet states. By virtue of the Choi isomorphism, the density matrix can be regarded as an element of the tensor product space $\mathcal{H} \otimes \mathcal{H}$, where $\mathcal{H} = (\mathbb{C}^2)^{\otimes N}$ is the Hilbert space of N spins. Thus the isotropic tensors with up to N indices are the $\mathsf{S}_{\text{tot}} = 0$ states formed from $2N$ spin-1/2 spins which number $\frac{1}{N+1}\binom{2N}{N}$ (the Catalan numbers, C_N). The number of isotropic tensors of fixed rank n is the number of $\mathsf{S}_{\text{tot}} = 0$ states that can be formed from n spin-1 spins. These are the Riordan numbers $R_n = \sum_{m=0}^{n} (-1)^{n-m}\binom{n}{m} C_m$ [180–182].

Turning to nonzero ω_i, the multiplets can be seen to split as shown in Fig. 5.1. To find the decay rate, one must identify the state whose eigenvalue has the least negative real part (which we shall term the dominant eigenvalue). Therefore, for small ω_i ($|\omega_i| \ll |\Omega|$) at least, the dominant eigenvalue will lie within the $\mathsf{S}_{\text{tot}} = 0$ (i.e. singlet) subspace. The splitting of the singlet multiplet in the real direction can be thought of as a second-order perturbative correction of the form ω_i^2/g_+. However, for this problem we are in fact afforded a more facile route via the exact solution, to which we now turn.

The exact eigenstates of (5.12) take the Bethe form [183]

$$|\mu_1 \cdots \mu_m\rangle = \prod_{k=1}^{m}\left(\sum_{j=1}^{n} \frac{\mathsf{S}^+_j}{\mu_k - \frac{1}{2}i\omega_j}\right)|\chi^-\rangle, \tag{5.19}$$

where $\mathsf{S}^z_{\text{tot}} = m - n$, the pseudovacuum $|\chi^-\rangle$ is the lowest weight state $|-1\rangle^{\otimes n}$, and the Bethe roots $\{\mu_i\}$ satisfy the Bethe ansatz equations

$$\frac{1}{g_+} + \sum_{k=1}^{n} \frac{1}{\mu_j - \frac{1}{2}i\omega_k} - \sum_{k \neq j}^{m} \frac{1}{\mu_j - \mu_k} = 0. \tag{5.20}$$

---

[2] In fact, the case of $g_+ \neq g_-$ and $\omega_j = 0$ is also exactly solvable: it corresponds to the Lipkin–Meshkov–Glick model [179].

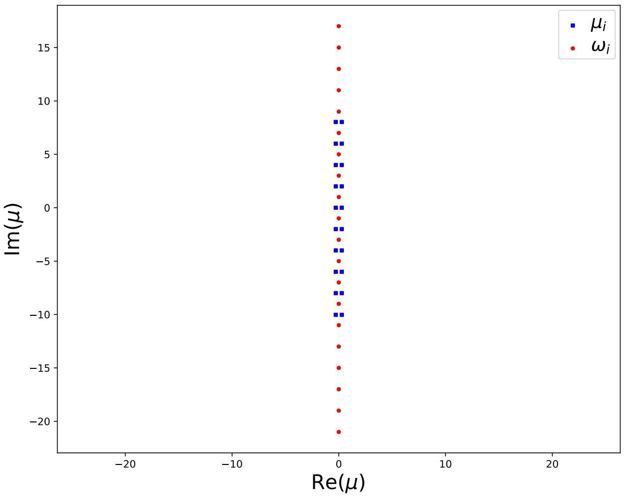

FIGURE 5.3: Illustration of the string state formed by the Bethe roots (blue squares), found by numerical solution of (5.20) for $n = 20$ and $g_+ \to \infty$; as in Fig. 5.2, the ω_i are represented by red circles. The effect of finite g_+ is to push the Bethe roots in the negative real direction.

The eigenvalue $\lambda(\vec{\mu})$ of a Bethe state is given by

$$\lambda(\vec{\mu}) = 2\sum_{j=1}^{m} \mu_j - i\sum_{j=1}^{n} \omega_j, \tag{5.21}$$

where, since $\mathsf{S}^z_{\text{tot}}$ is conserved, we continue to set $g_0 = 0$ without loss of generality.

The equations (5.20) can be interpreted in terms of two-dimensional classical electrostatics [170]: if the ω_i and μ_i correspond to the positions of fixed and free point charges respectively, and $1/g_+$ represents a uniform electric field, then (5.20) describes the equilibrium condition. The equilibrium configurations describe saddle points of the energy (Earnshaw's theorem), and so finding all solutions for large n is a difficult task.

Naive numerical root finding on the Bethe equations for random ω_j configurations tends to yield solutions in which the Bethe roots condense onto curves as shown in Fig. 5.2. These are the descendants of the states of maximum S_{tot} (when $\omega_i = 0$), which though of interest in the context of superradiance do not directly concern us here. We note in passing that the analogue of superradiance that appears here is that the eigenvalues of these states (for fixed g_+) scale quadratically with n, and so the correlations for states of $\mathsf{S}_{\text{tot}} \sim n$ decay at a rate that is $O(n^2)$ (cf. the quadratic dependence on S_{tot} also found when $\omega_i = 0$). This is to be contrasted with the $O(n)$ decay rate of the singlet correlations, which we shall discuss next.

We were able to find the Bethe roots for the dominant state in the case of uniformly spaced ω_i: they form the string state shown in Fig. 5.3. In the $n \to \infty$ limit, it is possible to evaluate the infinite summations in (5.20) exactly. If the spacing of the fixed charges is $i\Delta_y$ and the free

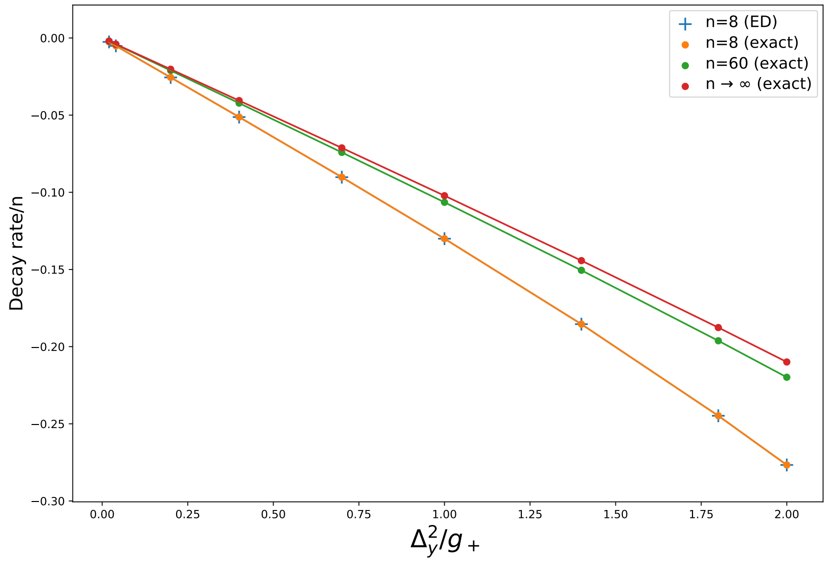

FIGURE 5.4: Comparison of the decay rate (dominant Liouvillian eigenvalue) of n-spin correlations for $\Omega = -(n+3)$ and $\omega_j = j\Delta_y$ (where $\Delta_y = 2$) evaluated by (i) exact diagonalisation for $n = 8$, (ii) exact solution at $n = 8$ and 60 and (iii) exact solution for $n \to \infty$.

charges on either side of the imaginary axis have real parts Δ_+ and $-\Delta_-$, we are left with

$$\begin{aligned} \frac{2\pi}{\Delta_y}\tanh\left(\frac{2\pi\Delta_+}{\Delta_y}\right) &= \frac{\pi}{\Delta_y}\coth\left(\frac{\pi(\Delta_+ + \Delta_-)}{\Delta_y}\right) - \frac{1}{g_+}, \\ \frac{2\pi}{\Delta_y}\tanh\left(\frac{2\pi\Delta_-}{\Delta_y}\right) &= \frac{\pi}{\Delta_y}\coth\left(\frac{\pi(\Delta_+ + \Delta_-)}{\Delta_y}\right) + \frac{1}{g_+}. \end{aligned} \tag{5.22}$$

Solving these two equations numerically for $\Delta_\pm$ enables us to find the Liouvillian eigenvalue of the string state.

In Fig. 5.4, we show convergence of the finite n solution of the Bethe equations to this large n result and also verify that for small n, the string solution coincides with the dominant eigenvalue found by exact diagonalisation. The observed linear dependence of the dominant eigenvalue on $1/g_+$ is consistent with the aforementioned ω_i^2/g_+ splitting predicted by perturbation theory.

A further interesting consequence of the integrability of our model is the absence of level repulsion as the spectrum varies with varying ω_i (see Fig. 5.5), leading to Poissonian level statistics. We conjecture that choosing ω_i to be independent and identically distributed will therefore lead to the relaxation rate (magnitude of the real part of the dominant eigenvalue) λ_0 ($\lambda_0 \geq 0$) having the Weibull distribution $\frac{\alpha}{\beta}\left(\frac{\lambda_0}{\beta}\right)^{\alpha-1} e^{-(\lambda_0/\beta)^\alpha}$ for some α and β [62]. This is a special case of the generalised extreme value distribution (1.41) introduced in Chapter 1 that accounts for the fact that λ_0 is nonnegative.

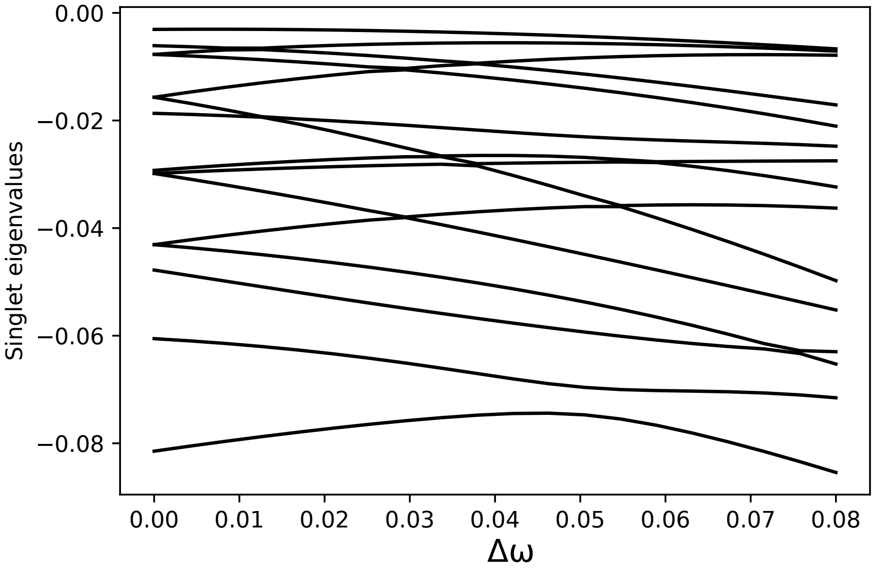

Figure 5.5: Typical motion of the singlet eigenvalues as the ω_i are smoothly translated (parameterised by $\Delta\omega$), revealing the presence of level crossings.

5.6 Conclusions and outlook

We have computed the exact relaxation rate of correlations in a model of spins precessing at different frequencies and coupled to a common noise source by exploiting a mapping to an exactly solvable model in the high-temperature limit. Our solution can be used to evaluate the effect of inhomogeneous splittings on a system of qubits coupled to a common bath.

The derivation of the spin-spin interaction in (5.12) may be generalised to the case of noise with arbitrary correlations between different spins j and k, leading to a coupling g_{ij} that could define an arbitrary quadratic spin-spin interaction. In general, the dominant eigenvalue of such an interaction will be nonzero and negative – a spin model will have a finite positive ground state energy – whereas for the infinite-range coupling we have considered a nonzero dominant eigenvalue arises because of the ω_i. Nevertheless, it would be interesting to explore other possibilities e.g. integrable 1D spin chains.

What happens at finite temperature when $g_+ \neq g_-$ – a situation describing relaxation as well as classical noise? The Lindblad operators vanish on any state $|\Psi\rangle$ satisfying $\sum_j \mathbf{s}_j |\Psi\rangle = 0$, and for $\omega_i = 0$ these form a decoherence-free subspace for N even of dimension $C_{N/2}$, for any $g_\pm$ [149, 150]. Density matrices formed from these states are a subset of the isotropic density matrices considered earlier. As in that case, $\omega_j \neq 0$ will cause decoherence of this subspace. Unfortunately, we have no reason to believe that the model remains integrable in the more general case, so finding an analytical description of the relaxation of n-spin correlations at finite temperature remains an open problem.

Chapter 6

Noisy coupled qubits: operator spreading and the Fredrickson–Andersen model

In the last chapter, it turned out to be a useful perspective to interpret the high-temperature limit of spins coupled to a common bath in terms of a coupling to a classical stochastic field. Here we shall exploit this approach more extensively in order to study noise-averaged observables for a system of exchange-coupled quantum spins (qubits), each subject to a stochastic drive. Averaging over noise yields Lindbladian equations of motion; when these are subjected to a strong-noise perturbative treatment, classical master equations are found to emerge. The dynamics of noise averages of operators displays diffusive behaviour or exponential relaxation, depending on whether the drive conserves one of the spin components or not. In the latter case, the *second moment* of operators – from which the average subsystem purity and out-of-time-order correlation functions can be extracted – is described by the Fredrickson–Andersen model, originally introduced as a model of cooperative relaxation near the glass transition. It is known that fluctuations of a ballistically propagating front in the model are asymptotically Gaussian in one dimension. We extend this by conjecturing, with strong numerical evidence, that in two dimensions the long-time fluctuations are in the Kardar–Parisi–Zhang universality class, complementing a similar observation in random unitary circuits. The operator spreading phenomenology that emerges, that of ballistic propagation with a diffusively broadening front is to be contrasted with the sharp front arising from exponential growth of the out-of-time-order correlator, characterised by a Lyapunov exponent, that has been found in a number of large-N quantum field theories. These latter models, typically featuring nonlocal interactions like the QREM, are also marked by an information scrambling time scale logarithmic in the system size (cf. the $O(\ln N)$ Thouless time we found for the stroboscopic QREM), instead of the linear in system size time scale for the decay of purity, entirely consistent with the local Hamiltonian we choose, that we find here.

6.1 Motivation

The success of microscopic models of matter hinges upon the assumption that the resulting macroscopic description is relatively insensitive to the precise disposition of the constituent particles. When applied to dynamical phenomena – collective motion – this assumption seems at odds with our usual understanding of generic dynamical systems: that they display chaos and an exponential sensitivity to initial conditions.

That we can derive the (deterministic) laws of hydrodynamics from the motion of gas particles and the assumption of molecular chaos shows that this contradiction is not as severe as it may at first seem. By focussing on coarse-grained variables like the average local velocity, the underlying chaotic motion fades into the background and serves only to give rise to the pressure, viscosity and other parameters of the effective description.

Nevertheless, if one believes that the butterfly effect is more than a figure of speech, something must have been lost along the way. By focusing on *average* quantities, the growth of *fluctuations* from the microscopic to the macroscopic is obscured. Long a part of statistical fluid dynamics [184–186], these questions have only recently been taken up in quantum field theory [79, 86, 90, 187–191] and many-body physics [92–94, 192–195].

Traditionally, these fields have been concerned with averages $\langle O_j(t)\rangle$, and response functions $i\langle[O_j(t), O_k(0)]\rangle$ of Heisenberg picture observables $O_j(t)$. However, the act of taking expectations in these quantities obscures the possibility that in a given experiment we may observe a very different response in observable $O_j(t)$ to a perturbation coupled to observable $O_j(0)$. The variance of the response function defines the out-of-time-order correlation function (OTOC)

$$C_{jk}(t) \equiv \frac{1}{2}\langle\left[O_j(t), O_k(0)\right]^\dagger \left[O_j(t), O_k(0)\right]\rangle, \tag{6.1}$$

that has been suggested as a diagnostic of many-body quantum chaos [77, 79, 86, 191]. In light of the above discussion, it is convenient to think of the OTOC in terms of a supersystem consisting of two independent copies of the system under consideration, and extract it from the operator $O_j(t) \otimes O_j(t)$. The duplicate system is sometimes known as the thermofield double [196].

In recent years, OTOCs have been calculated in a variety of models, including the SYK model [78, 197, 198], the many-body localised phase of one-dimensional spin models [80–83, 199], weakly interacting fermions [88, 200], as well as chaotic single-particle systems [201].

The models we shall study consist of a system of coupled qubits (spin-1/2 objects) subject to classical noise described by a stochastic process η_t [202]. Our focus will be the first two operator moments:

$$\overline{O_j} \equiv \mathbb{E}_\eta\left[O_j\right], \qquad \overline{O_j \otimes O_j} \equiv \mathbb{E}_\eta\left[O_j \otimes O_j\right]. \tag{6.2}$$

where $O_j \in \{X_j, Y_j, Z_j\}$ is one of the Pauli matrices describing qubit j. The motivations for this study are:

1. Conventional wisdom suggests that noise is antithetical to quantum coherence. On the other hand, the evolution of a quantum system in the presence of classical noise is still

unitary. We will see that the expected loss of coherence is only true on average: the first and second moments have completely different behaviour.

2. The limit of strong noise provides a controlled approximation in which we can obtain a tractable dynamics of the moments.

3. In the era of real noisy intermediate-scale quantum computers [203], there is need to understand the dynamics of quantum information in the presence of strong noise.

The stochastic models we introduce may be regarded as continuous-time analogues of the random unitary circuit model studied in many recent works [91–94, 125, 192, 204–209]. Though they share some phenomenology, our analysis of the stochastic models is completely different, being based on Lindblad equations. Expectations over stochastic trajectories are taken at the first step, and the analysis of the strong-noise limit is based on conventional many-body perturbation theory. This allows any (deterministic) coupling between qubits to be taken into account – though we focus on a Heisenberg coupling for simplicity of presentation – and allows models with conservation of one of the spin components to be handled on the same footing.

As is the case for the random unitary circuit models, the dynamics of moments in certain cases can be identified with the probability distribution of a classical stochastic process [210–213] (see Table 6.1). For the second moment (or OTOC) in a model without any conserved quantities, this is the Fredrickson–Andersen (FA) model, originally introduced to describe dynamics at the glass transition [214]. The FA model is an example of a *kinetically constrained model* – see [215] for a recent review – and has a rich phenomenology that we apply to the stochastic spin model[1]. Specifically, we will see that with appropriate initial conditions the FA model describes ballistically growing fronts that are associated with the spreading of the support of local operators in the Heisenberg picture (see Fig. 6.1). A characteristic speed for operator spreading in many-body systems was first identified in [189], and it has since become known as the 'butterfly velocity' v_{B}.

6.2 Models and mapping

6.2.1 Models

We consider a system of N spin-1/2 objects (qubits), and the closely related cases of (1) Heisenberg picture evolution of observables $O(t)$: $\partial_t O(t) = i[H(\eta_t), O(t)]$ under a Hamiltonian $H(\eta_t)$ depending on a stochastic process η_t, and (2) the von Neumann equation for the density matrix $\rho(t)$: $\partial_t \rho(t) = -i[H(\eta_t), \rho(t)]$.

We will be concerned with the first two operator moments:

$$\overline{O} \equiv \mathbb{E}_\eta\left[O\right], \qquad \overline{O \otimes O} \equiv \mathbb{E}_\eta\left[O \otimes O\right]. \tag{6.3}$$

---

[1] We note that *deterministic* kinetically constrained models – including a discrete-time deterministic FA model – recently appeared in the study of certain unitary circuits [193, 216].

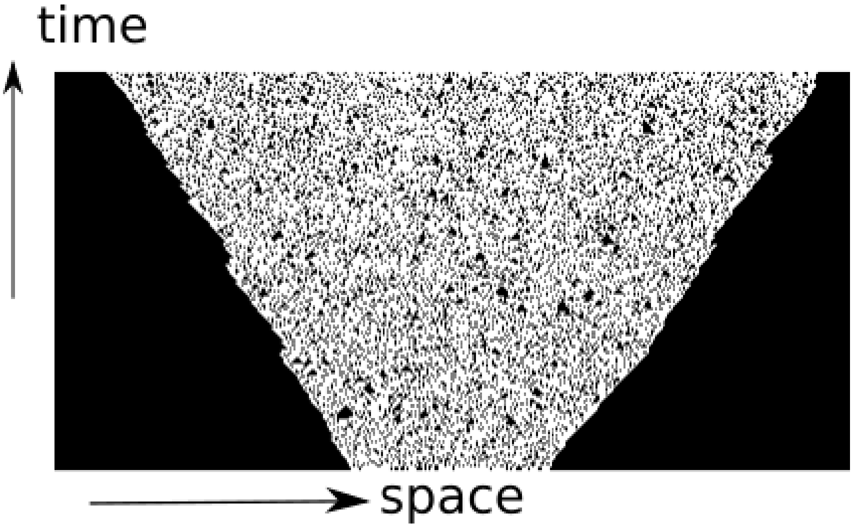

FIGURE 6.1: Growth of fronts in the one dimensional FA model with a finite average 'butterfly' velocity v_{B}.

The second (and higher) moments of an operator carry a great deal more information about the dynamics than the average alone. In particular, the second moment gives us:

1. The average purity
$$\overline{\gamma} \equiv \overline{\operatorname{tr}\left[\rho_A^2\right]}, \tag{6.4}$$
where ρ_A is the reduced density matrix of a subsystem A. Labelling bases of the subsystem A and its complement A^c by the (multi-)indices A and A^c, we have
$$\overline{\gamma} = \sum_{\mathsf{A}_1,\mathsf{A}_2,\mathsf{A}_1^c,\mathsf{A}_2^c} \overline{\rho_{\mathsf{A}_1\mathsf{A}_1^c,\mathsf{A}_2\mathsf{A}_1^c}\,\rho_{\mathsf{A}_2\mathsf{A}_2^c,\mathsf{A}_1\mathsf{A}_2^c}}\ , \tag{6.5}$$
which may be extracted from $\overline{\rho \otimes \rho}$.

2. The average OTOC
$$\overline{C}(j-k,t) \equiv \overline{\frac{1}{2}\operatorname{tr}\left[\rho\left[O_j(t),O_k(0)\right]^\dagger\left[O_j(t),O_k(0)\right]\right]}, \tag{6.6}$$
where $O_{i,j}$ are operators on qubit j and k. $\overline{C}(x,t)$ may be extracted from $\overline{O_j(t)\otimes O_j(t)}$ by contracting indices with ρ and $O_k(0)$.

The generalisation of our approach to higher moments is straightforward, and we will return to this point in the conclusion.

We will consider two models, one with conserved total z-component of spin (C) and one without (NC). In both cases, the Hamiltonian is the sum of deterministic and stochastic terms

$$H_{\mathrm{C}} = H + \sum_{j=1}^{N} \eta_t^j Z_j \tag{C}$$

$$H_{\mathrm{NC}} = H + \sum_{j=1}^{N} \boldsymbol{\eta}_t^j \cdot \boldsymbol{\sigma}_j, \tag{NC}$$

where $\boldsymbol{\sigma} = (X, Y, Z)$ are the usual Pauli matrices and η_t is assumed to be delta-correlated noise,

$$\mathbb{E}_\eta \left[\eta_t^j \eta_{t'}^k\right] = g\delta(t-t')\delta_{j,k}, \tag{6.7}$$

while $\boldsymbol{\eta}_t = (\eta_t^x, \eta_t^y, \eta_t^z)$ contains three independent components (assumed identical for ease of notation). H is a time-independent Hamiltonian describing local coupling between the spins. Our approach is not particularly sensitive to the precise form of H, but for simplicity we will begin with the Heisenberg chain

$$H = J \sum_{j=1}^{N} \boldsymbol{\sigma}_j \cdot \boldsymbol{\sigma}_{j+1}. \tag{6.8}$$

The generalisation to other models, including those in higher dimension, will be evident.

If we formally express the white noise η_t^j as the Itô differential of a Brownian motion B_t^j,

$$\int^{t'} \eta_t^j \, dt = \sqrt{g} \int^{t'} dB_t^j, \tag{6.9}$$

then one finds that the generator dH_t^{C} of infinitesimal stochastic unitary evolution in model C is given by [202]

$$dH_t^{\mathrm{C}} = H dt + \sqrt{g} \sum_j Z_j \, dB_t^j. \tag{6.10}$$

A straightforward exercise in Itô calculus yields the equation of motion of the density matrix [175]

$$\begin{aligned} d\rho_t = e^{-idH_t^{\mathrm{C}}} \rho_t e^{idH_t^{\mathrm{C}}} - \rho_t &= -i\left[H, \rho\right] dt \\ - \frac{g}{2} \sum_j \left[Z_j, \left[Z_j, \rho\right]\right] dt &- i\sqrt{g} \sum_j \left[Z_j, \rho\right] dB_t^j, \end{aligned} \tag{6.11}$$

the expectation of which is thus of Lindblad form [146]

$$\partial_t \bar{\rho} = \overbrace{-i\left[H, \bar{\rho}\right]}^{L_H(\bar{\rho})} \overbrace{- \frac{g}{2} \sum_j \left[Z_j, \left[Z_j, \bar{\rho}\right]\right]}^{D(\bar{\rho})}. \tag{6.12}$$

The corresponding equation for model NC, obtained by an analogous procedure, is

$$\partial_t \bar{\rho} = -i[H, \bar{\rho}] - \frac{g}{2} \sum_j \sum_{a=1}^{3} [\sigma_j^a, [\sigma_j^a, \bar{\rho}]]. \tag{6.13}$$

The derivation for the first moment of an operator is obtained similarly, the only differences being $\rho \to O$ and $dH_t \to -dH_t$. We also note that this calculation can alternatively be done, albeit less concisely, by interpreting the stochastic process η_t in the Stratonovich sense (see e.g. Appendix A.4 of [217]).

6.2.2 Model C at strong noise: symmetric exclusion process for $\overline{O}$

A key simplification occurs in the limit of strong noise (g large), where the dynamics of the moments is restricted to certain *slow subspaces*. In the case of $\overline{O}$, this is the kernel of the dissipator $D(\bar{(O)})$. For example, in Model C the dynamics of $\overline{O}$ is restricted to the 2^N-dimensional diagonal matrix elements in the basis of Z_j eigenstates $|z_1 : z_N\rangle$ (here $z_1 : z_N$ denotes the N-tuple $(z_1, \cdots, z_N)$) with $z_j = \pm 1$. That is, only the matrix elements $\langle z_1 : z_N | O | z_1 : z_N \rangle$ survive the averaging as they are unaffected by the dephasing noise. We now show that the evolution of the probability distribution of a spin configuration $z_1 : z_N$ is described by the symmetric exclusion process (SEP) [218] (see Table 6.1).

	Model NC	Model C
$\overline{O}$	Exponential decay	Symmetric Exclusion Process
$\overline{O \otimes O}$	Fredrickson–Andersen	'Octahedral' model

TABLE 6.1: The behaviour of the first and second operator moments in Models NC and C in the strong-noise limit.

The dynamics on the slow subspace $\mathcal{S}$ can be analyzed perturbatively in g^{-1} (as is done in [217] and [219]); the effective Liouvillian to leading order takes the form $\mathcal{L}_{\text{eff}} = -\mathcal{P}_{\mathcal{S}} L_H D^{-1} L_H \mathcal{P}_{\mathcal{S}}$, where $\mathcal{P}_{\mathcal{S}}$ is the projector onto $\mathcal{S}$ and D^{-1} is the inverse of the restriction of D to its coimage. Explicit evaluation leads to

$$\mathcal{L}_{\text{eff}} \bar{\rho} = -\frac{J^2}{16g} \sum_j [\sigma_j^+ \sigma_{j+1}^- + \text{h.c.}, [\sigma_j^+ \sigma_{j+1}^- + \text{h.c.}, \mathcal{P}_{\mathcal{S}} \bar{\rho}]]. \tag{6.14}$$

Let us regard $\bar{\rho} \in \mathcal{S}$ as an element $\vec{\rho}$ of a vector space over $\mathbb{R}$ (sometimes referred to as 'superspace') with basis $\{|1\rangle\langle 1|, |0\rangle\langle 0|\}^{\otimes N}$. Then $\mathcal{L}_{\text{eff}}$ acts as a matrix L on $\vec{\rho}$, giving the master equation

$$\partial_t \vec{\rho} = \mathsf{L} \vec{\rho}, \tag{6.15}$$

with $\mathsf{L} = \frac{J^2}{g} \sum_i (\vec{\sigma}_i \cdot \vec{\sigma}_{i+1} - \mathbb{1})$. The corresponding effective Hamiltonian $-\mathsf{L}$ (if we think of the master equation as an imaginary-time Schrödinger equation) coincides with that of a Heisenberg ferromagnet. Up to a constant, L is thus seen to be the generator of the SEP [220]. In the one-dimensional case, we have an alternative route to this result as the model is found to be integrable by means of a mapping to an imaginary-U Hubbard model [154]. In the strong-noise limit, the Bethe ansatz equations reduce to those of the spin-1/2 ferromagnetic Heisenberg model, from which the quadratically dispersing Liouvillian spectrum and consequent diffusive relaxation follow (as was established earlier in [221] by analytic evaluation of the single-particle Green's function).

6.2.3 Model NC at strong noise: Fredrickson–Andersen model for $\overline{O \otimes O}$

The dynamics of the first moment in model NC is trivial: the slow subspace is one-dimensional (i.e. contains only the identity) and so we find fast local relaxation rather than any hydrodynamics as in model C.

The second moment of Model NC does have interesting dynamics in the presence of strong noise, however. Since the noise in this model randomises all components of the spins, $\overline{O \otimes O}$ lives in the tensor product of the space spanned by the rotationally invariant single-site factors

$$
\begin{aligned}
|0_j\rangle &\equiv \frac{1}{2}\mathbb{1}_j \otimes \mathbb{1}_j \\
|1_j\rangle &\equiv \frac{1}{6}\left[X_j \otimes X_j + Y_j \otimes Y_j + Z_j \otimes Z_j\right].
\end{aligned}
\tag{6.16}
$$

Any $\overline{O \otimes O}$ of this form has the expansion

$$
\overline{O \otimes O} = \sum_{n_1:n_N \in \{0,1\}^N} \mathsf{C}^O_{n_1:n_N} \, |n_1 : n_N\rangle . \tag{6.17}
$$

Using the properties of the Pauli matrices it is easy to show

$$
\overline{\operatorname{tr}\left[O^2\right]} = \sum_{n_1:n_N \in \{0,1\}^N} \mathsf{C}^O_{n_1:n_N}. \tag{6.18}
$$

Since the trace of any operator product $\operatorname{tr}\left[O_1(t)O_2(t)\right]$ is conserved under Heisenberg evolution, we may think of $\mathsf{C}^O_{n_1:n_N}$ as a probability distribution (up to overall normalisation) and its evolution equation

$$
\partial_t \mathsf{C}^O = \mathsf{L}\mathsf{C}^O \tag{6.19}
$$

as a (classical) master equation. In Refs. [210–213], a related discrete-time Markov chain was obtained for the dynamics of operator moments due to randomly chosen two-qubit unitary transformations. This Markov chain was the basis of the calculations of OTOCs and purity in the random unitary circuit model in Ref. [92].

What stochastic process is described by L? We will see that it is the *Fredrickson–Andersen* (FA) model [214]. The FA model is defined on a lattice with sites that may either be in state 1 or

0, with pairs of neighbouring sites j and k undergoing the transitions

$$1_j 1_k \underset{\Gamma_1}{\overset{\Gamma_0}{\rightleftharpoons}} 1_j 0_k \tag{6.20}$$

with rates $\Gamma_{0,1}$. In the stationary state, sites are independent with probability $p_1 = \Gamma_1/(\Gamma_1 + \Gamma_0)$ to be 1. We find $\Gamma_0 = \Gamma_1/3 = 4J^2/3g$ for model NC, i.e., 1s are three times more common than 0s:

$$\mathsf{C}^{O}_{n_1:n_N}\big|_{\text{stationary}} = \frac{1}{4^N}\prod_j 3^{n_j}. \tag{6.21}$$

Two further comments: (1) The dynamics of C^A and C^ρ are identical because the rates are quadratic in J. (2) Individual trajectories of the FA model have no meaning, as only the probability distribution C^O appears in the moment $\overline{O \otimes O}$.

The derivation of the effective dynamics for $\overline{O \times O}$ follows the same pattern as for the first moment. Noise averaging the stochastic differential equation for the second moment of ρ in model NC leads to the Lindblad equation for the replicated system

$$\partial_t \overline{\rho \otimes \rho} = -i[\mathcal{H}, \overline{\rho \otimes \rho}] - \frac{g}{2}\sum_{j,a}[\Sigma^a_j, [\Sigma^a_j, \overline{\rho \otimes \rho}]] \tag{6.22}$$

where we have introduced the operators $\mathcal{H} = H \otimes \mathbb{1} + \mathbb{1} \otimes H$ and $\Sigma^a_j = \sigma^a_j \otimes \mathbb{1} + \mathbb{1} \otimes \sigma^a_j$.

The kernel of the dissipator determines the slow subspace $\mathcal{S} = \operatorname{span}\left(\{|0\rangle, |1\rangle\}^{\otimes N}\right)$, where the $\{|0\rangle, |1\rangle\}$ states were defined in (6.16). The effective Liouvillian to leading order (see Appendix D.1 for the derivation for model C; the model NC result is obtained similarly) acts on elements of $\mathcal{S}$ according to

$$\mathcal{L}_{\text{eff}}(\cdots) = -\frac{1}{4g}\mathcal{P}_{\mathcal{S}}[\mathcal{H}, [\mathcal{H}, \cdots]. \tag{6.23}$$

A matrix representation for $\mathcal{L}_{\text{eff}}$ can again be found (see Appendix D.2 for details) if we take $\{|0\rangle, |1\rangle\}^{\otimes N}$ as a vector space basis. This matrix is given by $\mathsf{L} = \sum_j \mathsf{L}_{j,j+1}$, where

$$\mathsf{L}_{j,j+1} = \frac{4J^2}{g}\begin{pmatrix} 0 & 0 & 0 & 0 \\ 0 & -1 & 0 & 1/3 \\ 0 & 0 & -1 & 1/3 \\ 0 & 1 & 1 & -2/3 \end{pmatrix}, \tag{6.24}$$

can be identified as the transition rate matrix of a continuous-time Markov process: the one-spin facilitated FA model with rates given in (6.20).

A similar analysis for the second moment of model C does not appear to lead to a mapping to a classical stochastic model, but we nevertheless make some observations about the effective dynamics in Appendix D.1.

6.3 Phenomenology of fronts

6.3.1 Fronts in the FA model

The FA model was originally introduced to describe dynamics at the glass transition, and is an example of a *kinetically constrained model* [215]. The model has a spectral gap [222], indicating that equilibrium fluctuations are generically exponentially decaying in time. Our main interest, however, is in the nonequilibrium dynamics of the model, in particular in initial conditions with only a few 1s, or regions devoid of 1s. In this case a nonzero density of 1s grows into the empty region with a finite front velocity, see Fig. 6.1.

The dynamics of a front in the FA model in one dimension was recently analysed rigorously in Ref. [223] for a variant of the model [224] in which the transition rate is independent of the number of neighbours (see Ref.[225] for the related case of the East model). There it was shown that if the rightmost 1 starts at site 0, its displacement X_t after time t is asymptotically given by the normal distribution

$$\frac{X_t - v_{\mathrm{B}}t}{\sqrt{t}} \xrightarrow[t\to\infty]{d} \mathcal{N}(0, s^2), \tag{6.25}$$

for some v_{B} and s. This chimes with the arguments given in Refs. [92–94] for the random unitary circuit model that the probability distribution of X_t is that of a biased random walk.

6.3.2 Fronts in two dimensions

The derivation of the FA model in the strong-noise limit holds in any dimension. Ballistic motion of the front in kinetically constrained models in higher dimensions is discussed in Refs. [226–228]. It is natural to ask how the front distribution in (6.25) generalises to higher dimensions. For the random unitary circuit model, Ref. [92] proposed – and provided numerical evidence – that the fluctuations of the front at long times are in the universality class of the Kardar–Parisi–Zhang (KPZ) equation [229, 230]. In the $1 + 1$-dimensional case, relevant for the growth of a front in two dimensions, this equation has the form

$$\partial_t h = c_0 + \nu\partial_x^2 h + \frac{\lambda}{2}(\partial_x h)^2 + \zeta(x, t). \tag{6.26}$$

Here $h(x, t)$ denotes the displacement of the front in the direction of growth, as a function of transverse coordinate x. The first term in (6.26) is a contribution to the ballistic growth rate; the second describes diffusive motion of the surface; the third captures a quadratic dependence of the local growth rate on the tilt of the surface; the last is a spatially uncorrelated white noise. The quadratic term is a relevant perturbation below two spatial dimensions that is responsible for novel scaling behaviour. For the one-dimensional case considered here, fluctuations of the surface have a dynamical critical exponent z – describing the relative scaling of spatial and temporal fluctuations as $t \sim x^z$ – of $z = 3/2$, and growth exponent β – describing the growth of interface fluctuations as $h \sim t^\beta$ – of $\beta = 1/3$.

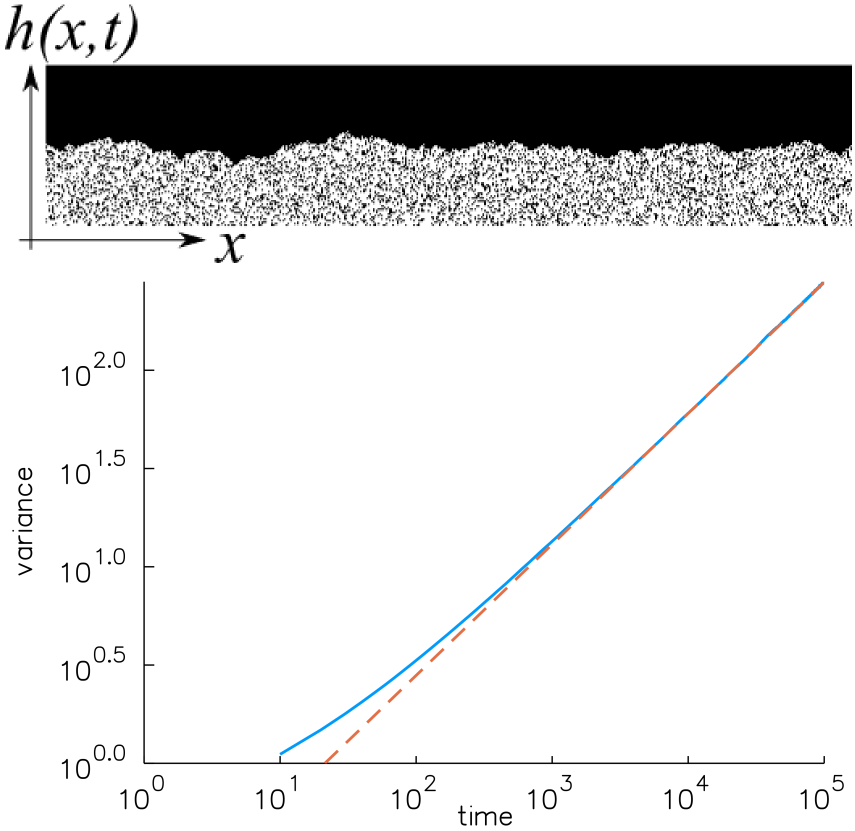

FIGURE 6.2: (Top) Upward growth of a front in the 2D FA model into a region of 0s (black), starting from a row of 1s. (Bottom) Growth of front variance with time. Dashed line is the power law $0.13t^{2/3}$, consistent with the KPZ growth exponent $\beta = 1/3$.

We performed a numerical simulation to determine the growth exponent for the FA model, the details of which are described in section 6.4. For simplicity, we considered the growth from a row of 1s, corresponding to flat initial conditions, rather than from a single 1, which leads to a rounded cluster. This option was not available to the authors of Ref. [92], as the peculiarities of the circuit model mean there is no roughening in a lattice direction. In a simulation of 10^5 time steps, we observe nearly two decades of scaling with the KPZ exponent $\beta \sim 1/3$ (see Fig. 6.2).

There is a wealth of exact results for the $1+1$-dimensional KPZ universality class: see Ref. [231] for a recent review. In particular, the long-time scaling form of the probability distributions of the height of a growing interface has been determined starting from various initial conditions. More precisely, we write

$$h(x,t) \underset{t\to\infty}{\overset{d}{\longrightarrow}} ct + \alpha t^{1/3}\chi, \tag{6.27}$$

where χ is a random variable with known distribution, and c and α are constants. In the case of flat initial conditions, χ is drawn from the Tracy-Widom distribution corresponding to the Gaussian Orthogonal Ensemble (GOE) [66, 232, 233].

In Fig. 6.3 we show a comparison between the probability distribution of the front obtained

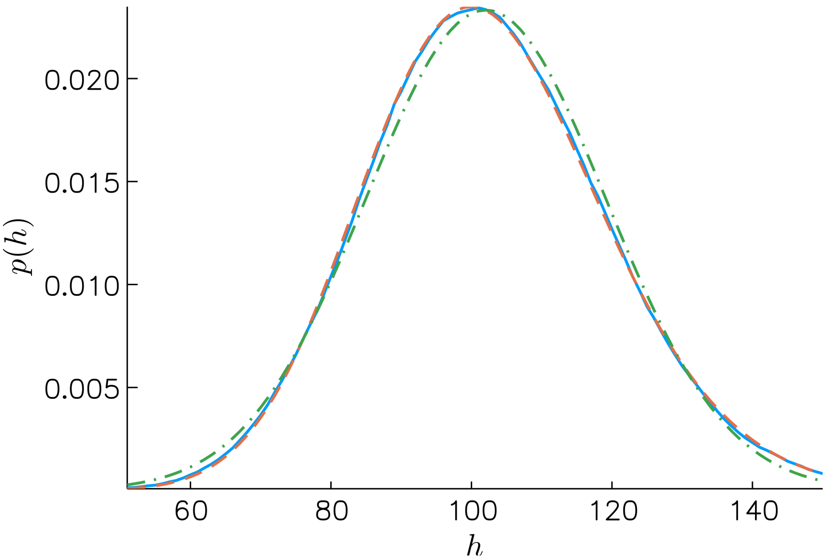

FIGURE 6.3: Front probability distribution at $t = 10^5$ compared with best fit Tracy-Widom density $F_1'(s)$ (dashed) and Gaussian (dash-dotted), where the width and shift of the distributions are fitting parameters.

at the end of our numerical simulation, and the best fit GOE Tracy-Widom and Gaussian distributions. The superiority of the Tracy-Widom fit is evident, in particular in capturing the skew of the distribution and the differing behaviour of the left and right tails

$$\log p(h) \propto \begin{cases} -|h|^3 & h \to -\infty \\ -h^{3/2} & h \to +\infty. \end{cases} \tag{6.28}$$

6.4 Details of the numerical simulation

For convenience we study the version of the FA model in which the probability of a site to flip its state depends only on having neighbours, not their number [224].

We use multispin coding [234–236], whereby 64 configurations of the model are represented as an array of (unsigned) 64-bit integers, and updated by bitwise operations. This allows 64 trajectories to be simulated simultaneously on a single core. Our simulation consisted of a single run on each of 16 virtual cores, corresponding to 1024 trajectories.

We initialised a $L \times H$ lattice with L 1s in the first row, enforcing periodic boundary conditions along the rows. The front is defined as the height of the highest 1 in each column. As the front grows in the vertical direction, it must be periodically reset so that it remains roughly centered. This is achieved by calculating the mean height of the front across the 64 configurations every 10 updates and moving the configuration downward by 10 sites when the mean exceeds $H/2 + 5$.

For the largest simulations we took $L = 10^4$, $H = 200$, and $T = 10^5$ timesteps. A height of $H = 100$ resulted in a breakdown of scaling behaviour at the longest times, presumably a

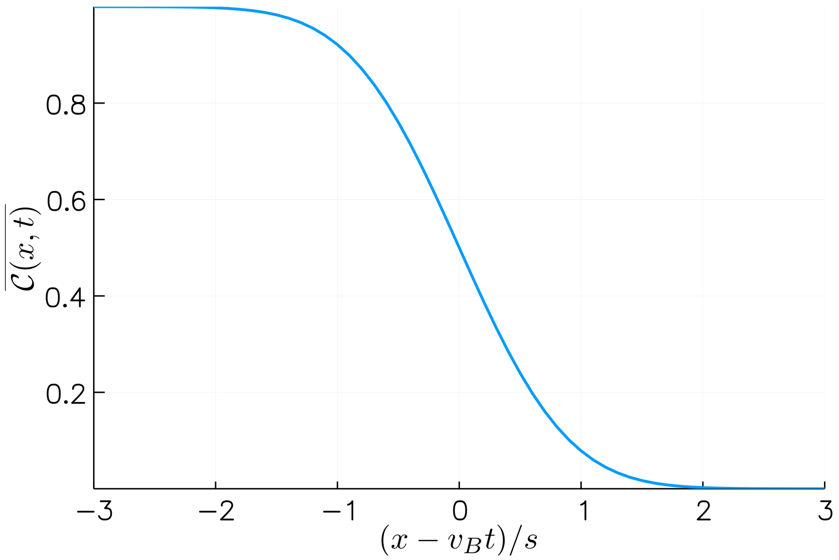

FIGURE 6.4: The averaged OTOC $\overline{C}_{jk}(t)$ is identified with the probability for sites j and k to be in the same cluster. Here, we have illustrated the Gaussian case – the functional form being that of an error function, the cumulative distribution function of a Gaussian – appropriate to one dimension.

consequence of the fluctuations of the interface being bounded by the finite height window [2].

6.5 Applied Phenomenology

6.5.1 Out-of-time-order correlation functions

The mapping to the FA model yields a simple expression for the OTOC (6.6) in Model NC with infinite temperature initial density matrix ρ

$$\overline{C}_{jk}(t) = 2^{-N}\left(\frac{4}{3}\right) \sum_{\substack{n_1:n_N\in\{0,1\}^N \\ n_k=1}} C^{O_j}_{n_1:n_N}(t), \tag{6.29}$$

where the normalisation follows from $\operatorname{tr}\left[O_j(t)^2\right] = 2^N$. For an FA model starting with only site j in state 1, the OTOC is then ($4/3$ times) the probability k has value 1 at time t.

Let us further make the reasonable assumption that, after the front arrives at site k, the probability to be in state 1 quickly approaches the equilibrium value of $3/4$. Then we identify

$$\overline{C}_{jk}(t) = \Pr\left[k \text{ in cluster seeded by } j\right], \tag{6.30}$$

or in other words, the cumulative distribution function of the front. The resulting behaviour of the OTOC is illustrated in Fig. 6.4.

---

[2] The simulation code and data analysis are written in Julia and are available as a Jupyter notebook, together with the simulation data, at `https://github.com/AustenLamacraft/FA-front`

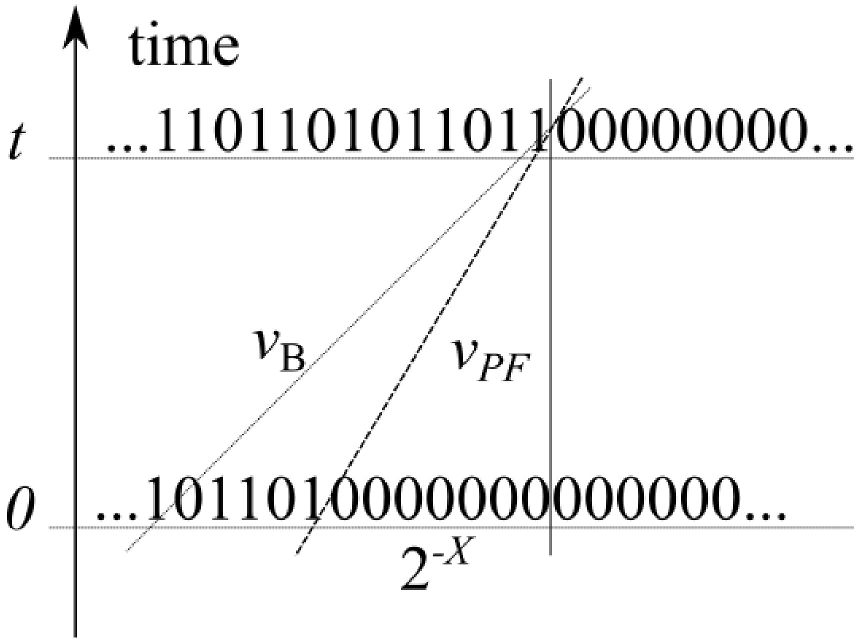

FIGURE 6.5: A ‘purity front’ velocity $v_{\mathrm{PF}} < v_{\mathrm{B}}$ arises from the joint probability of the propagating front deviating from the velocity v_{B} and an initial condition with X extra 0s.

6.5.2 Purity decay

Consider a partition of the qubits into sets A and A^c, of sizes $|A|$ and $|A^c|$. The average purity of a region A is expressed as (cf. Refs. [93, 204])

$$\overline{\gamma} = \overline{\operatorname{tr}\left[\rho_A^2\right]} = 2^{|A^c|} \sum_{\substack{n_j=0,1 \text{ for } j\in A \\ n_j=0 \text{ for } j\in A^c}} \mathsf{C}^{\rho}_{n_1:n_N}. \tag{6.31}$$

The purity is ($2^{|A^c|}$ times) the probability that A^c contain only 0s. Consider taking as an initial condition a random pure product state, described by a density matrix

$$\rho = \frac{1}{2^N} \prod_j \left[\mathbb{1}_j + \varrho_j \cdot \boldsymbol{\sigma}_j\right] \tag{6.32}$$

with unit vectors ϱ_j. Projected into the slow subspace of Model NC, this gives $\mathsf{C}_{n_1:n_N}(t=0) = 2^{-N}$. Comparing with (6.31), we see $\overline{\gamma}(t=0) = 1$, as required. Note that the overall probability of A^c being empty is $1/2^{|A^c|}$, but this exponentially small factor is cancelled by the prefactor in (6.31).

If A^c is empty (i.e. contains only 0s) at time t, we expect the fronts to be within A at earlier times. To see how this picture leads to the decay of purity, consider the growth of a single front in one dimension. The position of the front is described by (6.25). To find the most likely trajectory, the probability of finding a front at a distance X inside A at time 0 must be combined with the probability of the front propagating to the boundary between A and A^c at time t (see

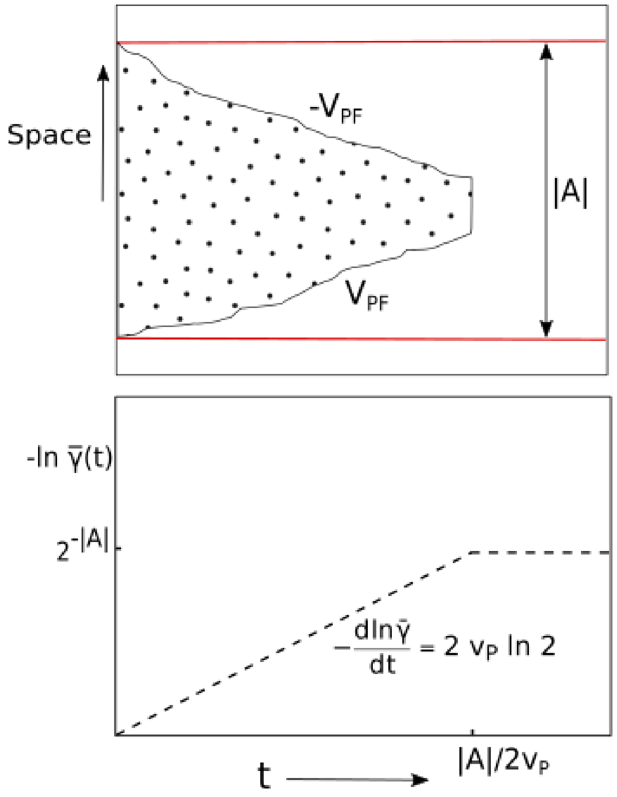

FIGURE 6.6: (Top) Schematic representation of the propagation of two fronts in 1+1 spacetime. White represents a region of 0s and black dots an active region of 1s and 0s. (Bottom) $-\ln \bar{\gamma}(t)$ for the case when $\bar{\gamma}(t)$ is computed for a finite subsystem. The red lines at fixed spatial positions in the upper right figure demarcate a finite subsystem of size $|A|$. Before saturation, $-\ln \gamma(\bar{t})$ grows at a rate (shown) controlled by the purity velocity.

Fig.6.5). The joint probability of these two events is then

$$P(X_t = 0, X_0 = -X) \sim \frac{1}{2^{|A^c|+X}} \exp\left(-\frac{[X - v_{\mathrm{B}} t]^2}{2s^2 t}\right). \tag{6.33}$$

For large t, it suffices to find the optimum value X_* of the initial front position, giving a 'purity front' velocity $v_{\mathrm{PF}} < v_{\mathrm{B}}$

$$v_{\mathrm{PF}} \equiv \frac{X_*}{t} = v_{\mathrm{B}} - s^2 \ln 2. \tag{6.34}$$

The fronts move slower than the butterfly velocity v_{B}. Note that a similar argument appears in Ref. [204], though with *ad hoc* assumptions about the statistics of front motion.

Substituting the optimal value X_* in (6.33) gives the exponential decay of the purity

$$\gamma(t) \sim \exp\left(-v_{\mathrm{B}} t \ln 2 + \frac{s^2 t}{2} \ln^2 2\right), \tag{6.35}$$

which enables us to define the 'purity velocity' $v_{\mathrm{P}} = v_{\mathrm{B}} - \frac{1}{2} s^2 \ln 2$, such that $\gamma(t) \sim \gamma(0) e^{-v_{\mathrm{P}} t \ln 2}$.

Applied to a region A of finite size, a simple generalisation of the above argument implies that two fronts move towards each other at $\pm v_{\mathrm{PF}}$. However, the two fronts *never touch* (see Fig. 6.6), for when $t > |A|/2v_{\mathrm{P}}$, the most likely initial configuration is completely empty, and the purity saturates. Thus we have

$$\gamma(t) \sim \begin{cases} e^{-2v_{\mathrm{P}}t\ln 2} & t < |A|/2v_{\mathrm{P}} \\ \frac{1}{2^{|A|}} & t > |A|/2v_{\mathrm{P}} \end{cases} \tag{6.36}$$

These results are valid for large t and $|A|$, where the optimum dominates the probability. The fact that purity decays on a time scale linear in the subsystem size is consistent with our local Hamiltonian, and is to be contrasted with the fast scrambling (i.e. in a time logarithmic in the size) possible in systems with highly nonlocal coupling, such as black holes [90, 188, 189].

If $|A^c| < |A|$, the situation is slightly different. Once $t > |A^c|/2v_{\mathrm{P}}$, the most probable way for an empty A^c to arise is from the stationary distribution (6.21), assuming this distribution is approached exponentially quickly from the initial state, giving

$$\gamma(t > |A|/2v_{\mathrm{P}}) = \frac{1}{2^{|A^c|}}. \tag{6.37}$$

The purity dynamics we have found (see Fig. 6.6) are consistent with the expectation, largely based on exact diagonalisation studies [85] and toy models [192], that ballistic entanglement growth is a universal feature of quantum chaotic many-body systems. By Jensen's inequality, the growth rate of $-\ln\bar{\gamma}(t)$ that we have calculated is a lower bound on the growth of the averaged second Rényi entanglement entropy. Moreover, our continuous-time results supplement the analytic discrete-time calculations in random unitary circuits [92–94], which have also confirmed this phenomenology (with a purity velocity satisfying $v_{\mathrm{P}} < v_{\mathrm{B}}$), via a mapping of the average purity onto the partition function of a directed random walk. The approach, which has been extended to obtain the higher Rényi entropies from a correspondence with a hierarchy of classical statistical mechanics models [237], has motivated the suggestion of a "minimal membrane" picture of entanglement spreading in generic nonintegrable quantum systems [206].

6.6 Conclusions

We have provided a precise account of operator spreading for a system of interacting qubits undergoing continuous time evolution, with each qubit independently coupled to a stochastic drive. By averaging over noise, Lindblad equations for the first and second operator moments were derived and studied perturbatively in the strong-noise limit; the central result being the identification of a mapping to the Fredrickson–Andersen model for the second moment dynamics in the case of noise that does not conserve a spin component. Considering the phenomenology of front growth in this model then enabled us to determine the implications for the behaviour of OTOCs and the decay of subsystem purity, which were found to be in line with the results established in random unitary circuit models. Although the mapping holds in arbitrary dimension, we restricted our attention to the one- and two-dimensional case: in one spatial dimension, we exploited the known exact Gaussian asymptotics of the front, whilst in two dimensions we conjectured, with numerical support, that front fluctuations exhibit (1+1)-dimensional KPZ universality, thus giving us access to exact results for the front shape in terms of Tracy-Widom distributions. After the completion of this work, a preprint appeared in which entanglement growth and operator spreading were numerically studied in a noisy spin model (in fact, model C) by a Krylov subspace method, and results consistent with the picture we have presented here were found [238].

Our approach generalises naturally to higher operator moments [239]. We expect that the identification of the slow subspaces and projection of the dynamics into those spaces will be more involved but tractable, and will allow the study of higher entanglement entropies and the full distribution of operator statistics; a convenient way to obtain these quantities may be to find the equation of motion for the moment-generating function of the density matrix.

Acknowledgements We thank Oriane Blondel, Juanpe Garrahan, Robert Jack, and Katarzyna Macieszczak for useful discussions.

Chapter 7

Concluding remarks

To conclude, we summarise the research presented in the preceding chapters, with emphasis on further work that suggests itself. We began in Chapter 2 with an attempt to identify a many-body counterpart of weak localisation by studying the ergodic phase of the quantum random energy model in analogy to the corresponding single-particle diagrammatic perturbation theory. A formal analogy can indeed be pursued by interpreting the QREM as an Anderson model on the hypercube, enabling a self-consistent Born approximation to the resolvent and subsequent ladder summation to describe diffusion modes. The analogy was found to break down upon attempting to evaluate the cooperon, where we observed that the dominant contribution is outside the diffusive regime. This kind of situation bears a resemblance to that of ballistic weak localisation, but we were not able to find a means of transposing the approaches successful there – kinetic equations in a Wigner representation – into the present context. The original question of whether weak-localisation corrections exist in the QREM thus remains open, although our efforts suggest diagrammatics are not likely to be fruitful and an alternative approach, perhaps via a supersymmetric field integral formulation, should be explored. However, we do at least find a compact master equation description of the relaxation of the disorder-averaged density matrix, whose evolution we can numerically simulate in a dimensionally reduced space and also study analytically after tracing out all but one of the spins.

Before attempting to obtain the weak-localisation corrections, it is a good start to analytically derive the RMT limit in the ergodic phase. This is what we proceeded to do in the next chapter, where we studied a stroboscopic QREM and applied a periodic-orbit perspective inspired by the analogy between our Floquet operator and quantum graph evolution operators. The diagonal approximation gave the first term in the short-time expansion of the form factor and was found to match that of RMT; based on the direct relevance of quantum graph results which have established agreement to all orders, we claim that the same conclusion can be drawn in this case too. On the other hand, weak localisation remains an unsolved problem from the perspective of periodic-orbit theory and further progress requires a conceptual breakthrough to correctly handle Hikami boxes in general.

Turning to a modified QREM in which the transverse field was replaced with a REM in a rotated basis, what we called a QREM with a random kinetic term, we were able to carry out a diagrammatic calculation of the density of states straightforwardly. The analogue of the self-consistent Born approximation in fact turned out to be a veiled R-transform calculation: the machinery required to compute the distribution of a sum of free random variables. The natural extension of our work is to attempt to apply free probability, namely the idea of higher-order freeness, in order to extract two-particle correlations, which we were unable to manipulate into an intelligible form in our diagrammatic framework. Moreover, it is worth pointing out a connection with the Floquet model that we studied in Chapter 3. If we define a stroboscopic analogue of the QREM with a random kinetic term, then the Floquet operator would consist of products rather than sums of free random variables: free probability again has a tool to use here, the S-transform, which enables the computation of the free multiplicative convolution describing the spectral density of the Floquet operator in terms of the constituent x- and z-basis distributions. These means of potentially broadening the applicability of free probability to random matrix models of interest in the context of localisation and quantum chaos represent good opportunties for further work.

In the second part of the thesis, we turned our attention from disordered to noisy quantum spin models and began with the problem of noninteracting spins coupled to a common noise source; this situation of correlated noise is quite different from the disordered problems we considered where disorder was always uncorrelated. Moreover, we showed that the model was Bethe ansatz integrable by mapping it to a non-Hermitian Richardson–Gaudin model. This situation is quite distinct from generic many-body systems: even when an MBL phase exists – exhibiting Poisson statistics as in an integrable model – the emergent integrability in that case is distinguished by a number of features, for instance, it does not rely on fine-tuning and so is robust to perturbation. Avenues for future work include: the finite-temperature regime, where integrability appears to be broken and a new approach needs to be found to understand the effect of temperature on the relaxation of correlations; the consideration of more general noise correlation models where these could be chosen to generate mappings to other integrable models; and a quantitative study of the structure of quantum correlations and how they evolve in time by making use of the Bethe wavefunctions.

Although we initially presented the model in Chapter 5 directly as a Lindblad master equation, we found it was more instructive to think of it as arising from averaging over a classical stochastic field. In the final chapter, we considered a more general class of stochastically driven interacting quantum spin models and analysed the dynamics of operator moments, distinguishing qualitatively different behaviour depending on whether or not the drive preserved a $U(1)$ symmetry (model C and model NC respectively). The second-moment dynamics for model NC was found to map onto a Fredrickson-Andersen model in the strong-noise limit, enabling us to use existing results in order to understand the phenomenology of the dynamics of averaged subsystem purity and out-of-time-order correlation functions. The behaviour we found of a front propagating ballistically and broadening diffusively is consistent with that seen in random unitary circuits and conjectured to hold in generic many-body Hamiltonians, but our results provide analytic confirmation of this in a continuous-time Hamiltonian model. Although the second-moment dynamics for model C does not map onto a classical stochastic model, it remains to be seen whether further analytic progress can be made in characterising the resultant ’octahedral’ model, which a recent exact diagonalisation study suggests is largely the same as model NC. Extending our calculation to higher moments is also natural, and would provide a means of bounding the higher entanglement entropies, relating the butterfly velocity (set by the Hilbert-Schmidt norm) to the Lieb-Robinson bound (set by the operator norm), and ultimately studying the full distribution (over noise trajectories) of the quantum statistics of observables.

Appendix A

Harmonic analysis on $\mathbb{Z}_2^N$

Consider the measure space $(\mathbb{Z}_2^N, P(\mathbb{Z}_2^N), \mathbb{P})$, where $\mathbb{Z}_2^N = \{-1, 1\}^N$, the σ-algebra $P(\mathbb{Z}_2^N)$ is the power set of $\mathbb{Z}_2^N$, and $\mathbb{P} = (\frac{1}{2}\delta_{-1} + \frac{1}{2}\delta_1)^{\otimes N}$ is the uniform probability measure. We shall be interested in the space $L^2(\mathbb{Z}_2^N)$ of functions $f : \mathbb{Z}_2^N \to \mathbb{R}$ that are square integrable with respect to $\mathbb{P}$ (i.e. $\int_{\mathbb{Z}_2^N} |f|^2 \, \mathrm{d}\mathbb{P}$ is finite). Equipped with the inner product

$$\langle f, g\rangle = \mathbb{E}[fg] = \int_{\mathbb{Z}_2^N} fg \, \mathrm{d}\mathbb{P} = 2^{-N} \sum_{z \in \mathbb{Z}_2^N} f(z)g(z), \tag{A.1}$$

$L^2(\mathbb{Z}_2^N)$ forms a Hilbert space.

The fundamental objects for doing harmonic analysis on an Abelian group G (such as $\mathbb{Z}_2^N$) are elements of the Abelian group of multiplicative characters $\mathrm{ch}(G)$ – the multiplicative characters are the homomorphisms from G to the multiplicative group of a field (usually real or complex numbers). On $\mathbb{Z}_2^N$, the characters χ_x can be expressed as

$$\chi_x(z) := \prod_{i | x_i = -1} z_i. \tag{A.2}$$

Note that 2^N elements $x \in \mathbb{Z}_2^N$ are in one-to-one correspondence with subsets $S \subseteq \{1, \ldots, N\}$. The set of characters $\mathrm{ch}(\mathbb{Z}_2^N)$ forms a complete, orthonormal basis of $L^2(\mathbb{Z}_2^N)$. We thus can define the Fourier transform $\widetilde{f}$ of f

$$f(z) = \sum_{x \in \mathbb{Z}_2^N} \widetilde{f}(x)\chi_x(z), \tag{A.3}$$

where the Fourier components can be written as

$$\widetilde{f}(x) = \mathbb{E}[f\chi_x] = \langle f, \chi_x\rangle. \tag{A.4}$$

Recasting this in the language of eigenstates of spin operators that we employed in section 2.1.1 by using the result $\chi_x(z) = 2^{N/2} \langle x|z\rangle$, we can write

$$\widetilde{f}(x) = \frac{1}{\sqrt{2^N}} \sum_z f(z) \langle x|z\rangle . \tag{A.5}$$

Appendix B

Hamming scheme combinatorics

We shall now compute the normalisation coefficients $\mathcal{N}_{h_1,h_2,h_{12}}$ for the permutation-invariant basis states defined in (2.125). Let us begin by writing down a generating function

$$G(z_1, z_2, z_{12}) = (1 + z_1 z_2 + z_{12}(z_1 + z_2))^N , \tag{B.1}$$

where $\mathcal{N}_{h_1,h_2,h_{12}}$ is equal to the coefficient of $z_1^{h_1} z_2^{h_2} z_{12}^{h_{12}}$. If we now extract the terms in G of order $z_{12}^{h_{12}}$ we have

$$\binom{N}{h_{12}} z_{12}^{h_{12}} (z_1 + z_2)^{h_{12}} (1 + z_1 z_2)^{N-h_{12}} \tag{B.2}$$

$$= \binom{N}{h_{12}} z_{12}^{h_{12}} z_2^{h_{12}} (1 + \frac{z_1}{z_2})^{h_{12}} (1 + z_1 z_2)^{N-h_{12}}. \tag{B.3}$$

From here, we can expand the two remaining binomial terms, writing down the general terms in their expansion in terms of two free parameters h and H

$$\mathcal{N}_{h_1,h_2,h_{12}} z_1^{h_1} z_2^{h_2} z_{12}^{h_{12}} = \binom{N}{h_{12}} z_{12}^{h_{12}} z_2^{h_{12}} \binom{h_{12}}{h} \left(\frac{z_1}{z_2}\right)^h \binom{N - h_{12}}{H} (z_1 z_2)^H, \tag{B.4}$$

where h and H can be chosen such that the powers of z_1, z_2, and z_{12} are equal to h_1, h_2, and h_{12} respectively. Solving simultaneously for h and H we find that $h = (h_1 - h_2 + h_{12})/2$ and $H = (h_1 + h_2 - h_{12})/2$, yielding

$$\mathcal{N}_{h_1,h_2,h_{12}} = \binom{N}{h_{12}} \binom{h_{12}}{\frac{h_1 - h_2 + h_{12}}{2}} \binom{N - h_{12}}{\frac{h_1 + h_2 - h_{12}}{2}}. \tag{B.5}$$

Having obtained the result in a mechanical fashion via the generating function, we can quickly arrive at the result through an explicit combinatorial argument. For a given state (i.e. a z_1, z_2 configuration with fixed $\{ h_1, h_2, h_{12} \}$; see Fig.B.1), each site contributes either 0 ($z_1^i = z_2^i$) or 1 ($z_1^i \neq z_2^i$) to h_{12}. So, we must first choose h_{12} of the N sites to contribute 1 to h_{12}; this can be done in $\binom{N}{h_{12}}$ ways. After choosing the h_{12}-contributing sites, there is still the freedom of arranging the sites with $z_1^i = 1, z_2^i = 0$ and $z_1 = 0, z_2^i = 1$ amongst themselves, and then of arranging the sites with $z_1^i = 0, z_2^i = 0$ and $z_1^i = 1, z_2^i = 1$, which do not contribute to h_{12}; these correspond to the second and third factors in

$$\mathcal{N}_{h_1,h_2,h_{12}} = \binom{N}{h_{12}} \times \binom{h_{12}}{|S_1| - |S_1 \cap S_2|} \times \binom{N - h_{12}}{h_1 - (|S_1| - |S_1 \cap S_2|)}. \tag{B.6}$$

We can apply the inclusion-exclusion principle in order to evaluate the intersection that appears: $h_{12} = |S_1| + |S_2| - 2|S_1 \cap S_2|$, whilst the remaining cardinalites that appear above are trivially $|S_1| = h_1$ and $|S_2| = h_2$ by definition. We can now relate the normalisation coefficients to an object in coding theory known as the Hamming scheme [240].

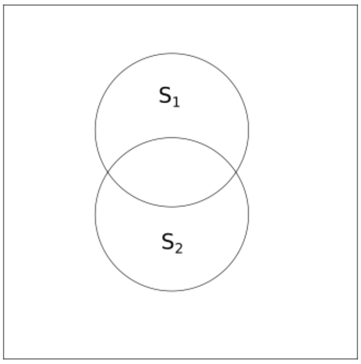

FIGURE B.1: For a given $|z_1\rangle \otimes |z_2\rangle$ state, we can construct a Venn diagram describing the four possible values of $z_1^i, z_2^i \in \{0, 1\}$ on each of the N sites: S_1 is the set of sites with $z_1^i = 1$, and S_2 the set of sites with $z_2^i = 1$.

Definition. *An association scheme $A = \{S, \mathcal{R}\}$ is a finite set S equipped with a set $\mathcal{R} = \{R_0, \dots, R_n\}$ of symmetric binary relations satisfying*

1. $R_0 = \{(s, s) \mid s \in S\}$.
2. *$\mathcal{R}$ is a partition of $S \times S$.*
3. $\forall\, i, j, k \in [0, n], \exists\, p_{ij}^k \in \mathbb{Z} \setminus \mathbb{Z}^-$ *such that* $\forall\, (s_1, s_2) \in R_k$

$$p_{ij}^k = |\{s_3 \in S \mid (s_1, s_3) \in R_i \text{ and } (s_2, s_3) \in R_j\}|. \tag{B.7}$$

The Hamming scheme is the association scheme when S is the hypercube (i.e. $S = \mathbb{Z}_2^N$) and the binary relation R_d relates points on the hypercube separated by a Hamming distance d. The intersection parameters p_{ij}^k describe the number of triangles on the hypercube with a fixed base of length k, and remaining sides of length i and j. In the case of the normalisation coefficients calculated above, we are counting the number of Hamming triangles with given side lengths and one vertex fixed; the two combinatorial quantities are thus related by

$$\mathcal{N}_{h_1,h_2,h_{12}} = p_{h_1,h_2}^{h_{12}} \binom{N}{h_{12}}, \tag{B.8}$$

reflecting the freedom to choose the position of the base in the case of $\mathcal{N}_{h_1,h_2,h_{12}}$.

Appendix C

Two-point correlators in the random kinetic quantum random energy model

Here we consider the averaged product of two resolvents for the random kinetic QREM and so are concerned with diagrams that have the structure shown in Fig. C.1. We proceed by analysing the various distinct configurations of A_i. Where V-lines occur ($A_i = z$), we can insert a resolution of the identity in the z-basis, $\sum_i |z_i\rangle\langle z_i|$, and similarly for $A_i = x$. The magnitude of the diagram will thus be controlled by the values of the inner products

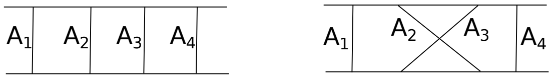

FIGURE C.1: Comparison of the contribution of ladder diagrams and diagrams with crossings to the two-particle vertex. $A_i \in \{x, z\}$ denote blocks of V (z-diagonal) or T (x-diagonal) lines.

$$|\langle a_1|a_2\rangle|^2 = \begin{cases} \delta_{a_1,a_2} & A_1 = A_2 \\ 2^{-N} & A_1 \neq A_2. \end{cases} \tag{C.1}$$

For arbitrary $\{A_i\}$, the ladder diagram gives

$$|a_1\rangle\langle a_1|a_2\rangle\langle a_2|a_3\rangle\langle a_3|a_4\rangle\langle a_4| \times \tag{C.2}$$

$$|a_1\rangle\langle a_1|a_2\rangle\langle a_2|a_3\rangle\langle a_3|a_4\rangle\langle a_4|\,, \tag{C.3}$$

and the crossed diagram

$$|a_1\rangle\langle a_1|a_2\rangle\langle a_2|a_3\rangle\langle a_3|a_4\rangle\langle a_4| \times \tag{C.4}$$

$$|a_1\rangle\langle a_1|a_3\rangle\langle a_3|a_2\rangle\langle a_2|a_4\rangle\langle a_4|\,. \tag{C.5}$$

Let us now consider the particular distinct configurations of $\{A_i\}$.

$\underline{A_1 = A_2 = A_3 = A_4}$

$$\text{Ladder}: \sum_{a_i} \delta_{a_1,a_2}\delta_{a_2,a_3}\delta_{a_3,a_4} = \sum_{a_1}, \tag{C.6}$$

$$\text{crossed}: \sum_{a_i} \delta_{a_1,a_2}\delta_{a_2,a_3}\delta_{a_3,a_4}\delta_{a_1,a_3}\delta_{a_2,a_4} = \sum_{a_1}, \tag{C.7}$$

$\Longrightarrow$ crossed diagram not suppressed.

$\underline{A_1 = A_2 = A_4 \neq A_3}$

$$\text{Ladder}: \sum_{a_i} \delta_{a_1,a_2} 2^{-2N} = 2^{-2N} \sum_{a_1,a_3,a_4}, \tag{C.8}$$

$$\text{crossed}: \sum_{a_i} \delta_{a_1,a_2}\delta_{a_2,a_4} 2^{-2N} = 2^{-2N} \sum_{a_1,a_3}, \tag{C.9}$$

$\Longrightarrow$ crossed diagram suppressed due to one fewer free summation.

$\underline{A_1 = A_4 \neq A_2 = A_3}$

$$\text{Ladder}: \sum_{a_i} 2^{-2N} \delta_{a_2,a_3} = 2^{-2N} \sum_{a_1,a_2,a_4}, \tag{C.10}$$

$$\text{crossed}: \sum_{a_i} \langle a_1|a_2\rangle \langle a_1|a_3\rangle \langle a_3|a_4\rangle \langle a_2|a_4\rangle \delta_{a_2,a_3} = 2^{-2N} \sum_{a_1,a_2,a_4}, \tag{C.11}$$

$\Longrightarrow$ crossed diagram not suppressed.

$\underline{A_1 = A_3 \neq A_2 = A_4}$

$$\text{Ladder}: \sum_{a_i} 2^{-3N}, \tag{C.12}$$

$$\text{crossed}: \sum_{a_i} 2^{-N} \delta_{a_1,a_3}\delta_{a_2,a_4} \langle a_1|a_2\rangle \langle a_3|a_4\rangle = 2^{-2N} \sum_{a_1,a_2} \tag{C.13}$$

$\Longrightarrow$ crossed diagram $\sim 2^N$ smaller than ladder.

The appropriate approximation for the two-particle vertex, as for the averaged resolvent, is thus to neglect diagrams with crossings between V and T lines. We can build up such diagrams using blocks consisting of only V or T lines, given respectively by the quantities

$$\Pi_V = \mathbb{E}\left[\frac{1}{\epsilon_1 - \Sigma_T - V}\frac{1}{\epsilon_2 - \Sigma_T - V}\right] = \frac{1}{\sqrt{\gamma_V}(\epsilon_2 - \epsilon_1)}\left[\mathcal{R}\left(\frac{\epsilon_1 - \Sigma_T}{\sqrt{2\gamma_V}}\right) - \mathcal{R}\left(\frac{\epsilon_2 - \Sigma_T}{\sqrt{2\gamma_V}}\right)\right] \tag{C.14}$$

$$\Pi_T = \mathbb{E}\left[\frac{1}{\epsilon_1 - \Sigma_V - \mathcal{T}}\frac{1}{\epsilon_2 - \Sigma_V - \mathcal{T}}\right] = \frac{1}{\sqrt{\gamma_T}(\epsilon_2 - \epsilon_1)}\left[\mathcal{R}\left(\frac{\epsilon_1 - \Sigma_V}{\sqrt{2\gamma_T}}\right) - \mathcal{R}\left(\frac{\epsilon_2 - \Sigma_V}{\sqrt{2\gamma_T}}\right)\right]. \tag{C.15}$$

Consider two-particle ladder diagrams built from blocks A_i as in Fig. C.1. First, if we have two

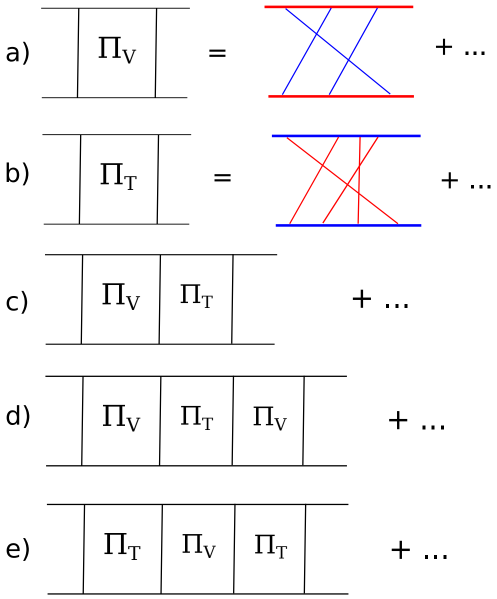

FIGURE C.2: Diagrams corresponding to the terms in (C.19). As before V and T lines are coloured blue and red respectively, whilst a bold blue (red) line corresponds to dressing by Σ_V (Σ_T). Diagrams a) and b) correspond to the two terms on the first line of (C.19), whilst c), d), and e) are the terms on lines 2, 3, and 4 respectively. The ... in these terms represent the geometric series generated by adding successive $\Pi_V\Pi_T$ blocks for c) and e), or $\Pi_T\Pi_V$ blocks in the case of d).

blocks of the same type, e.g. $A_1 = A_2 = x$:

$$\sum_{x_1,x_2} |x_1\rangle \langle x_1|x_2\rangle \langle x_2| \otimes |x_1\rangle \langle x_1|x_2\rangle \langle x_2| = \sum_{x} |x\rangle \langle x| \otimes |x\rangle \langle x| \,. \tag{C.16}$$

If we have two blocks of different type, e.g. $A_1 = z$ and $A_2 = x$

$$\sum_{z,x} |z\rangle \langle z|x\rangle \langle x| \otimes |z\rangle \langle z|x\rangle \langle x| = 2^{-N} \sum_{z,x} |z\rangle \langle x| \otimes |z\rangle \langle x| \,. \tag{C.17}$$

If we have three blocks, where A_i alternates e.g. $A_1 = A_3 = z$ and $A_2 = x$

$$\sum_{z_1,x_2,z_3} |z_1\rangle \langle z_1|x_2\rangle \langle x_2|z_3\rangle \langle z_3| = 2^{-N} \sum_{z_1,z_3} |z_1\rangle \langle z_3| \otimes |z_1\rangle \langle z_3| \tag{C.18}$$

The two-particle vertex Γ will thus contain terms of distinct matrix structure depending on the starting and ending block (i.e. Π_V or Π_T), and so Γ takes the form

$$\begin{aligned}\Gamma = {} & \Pi_V \sum_z |z\rangle\langle z| \otimes |z\rangle\langle z| + \Pi_T \sum_x |x\rangle\langle x| \otimes |x\rangle\langle x| \\ & + \frac{\Pi_V\Pi_T}{1-\Pi_V\Pi_T} \sum_{z,x} 2^{-N} (|z\rangle\langle x| \otimes |z\rangle\langle x| + \text{h.c.}) \\ & + \frac{\Pi_V\Pi_T\Pi_V}{1-\Pi_T\Pi_V} \sum_{z_1,z_3} 2^{-N} |z_1\rangle\langle z_3| \otimes |z_1\rangle\langle z_3| \\ & + \frac{\Pi_T\Pi_V\Pi_T}{1-\Pi_V\Pi_T} \sum_{x_1,x_3} 2^{-N} |x_1\rangle\langle x_3| \otimes |x_1\rangle\langle x_3| ,\end{aligned} \tag{C.19}$$

which can be represented diagrammatically as in Fig. C.2. Further work is required to extract useful information from this equation, though we can see from the frequency dependence of (C.14) that at high frequencies the two terms on the first line of (C.19) dominate with frequency dependence ω^{-1}, whereas in the low-frequency limit only the second line can be neglected whilst the other terms are responsible for ω^{-1} dependence in this regime too.

We can also consider the two-particle diagrams for the single-particle version of the model

$$\langle a_1|a_2\rangle = \begin{cases} \delta_{a_1,a_2} & A_1 = A_2 \\ \frac{e^{ikx}}{\sqrt{N}} & A_1 = x, A_2 = k \\ \frac{e^{-ikx}}{\sqrt{N}} & A_1 = k, A_2 = x. \end{cases} \tag{C.20}$$

$\underline{A_1 = A_2 = A_3 = A_4}$

Crossed diagram not suppressed (as above, for spins).

$\underline{A_1 = A_2 = A_4 \neq A_3}$

$$\text{Ladder}: \frac{1}{N^2}\sum_{a_i} \delta_{a_1,a_2} e^{2ik_3(x_1-x_4)} = \frac{1}{N}\sum_{x_1}, \tag{C.21}$$

$$\text{crossed}: \frac{1}{N^2}\sum_{a_i} \delta_{x_1,x_2}\delta_{x_2,x_4} e^{ik_3(x_1-x_4)} = \frac{1}{N}\sum_{x_1,x_2,x_4} \delta_{x_1,x_2}\delta_{x_2,x_4}\delta_{x_1,x_4} = \frac{1}{N}\sum_{x_1}, \tag{C.22}$$

$\implies$ crossed diagram not suppressed.

$\underline{A_1 = A_4 \neq A_2 = A_3}$

$$\text{Ladder}: \frac{1}{N^2}\sum_{a_i} \delta_{k_2,k_3} e^{2ik_2x_1} e^{-2ik_3x_4} = \frac{1}{N}\sum_{x_1}, \tag{C.23}$$

$$\text{crossed}: \frac{1}{N^2}\sum_{a_i} \delta_{k_2,k_3} e^{ik_2x_1} e^{ik_3x_1} e^{-ik_3x_4} e^{-ik_2x_4} = \frac{1}{N}\sum_{x_1}, \tag{C.24}$$

$\implies$ crossed diagram not suppressed.

$\underline{A_1 = A_3 \neq A_2 = A_4}$

$$\text{Ladder}: \frac{1}{N^3}\sum_{a_i} e^{2ik_2x_1}e^{-2ik_2x_3}e^{2ik_4x_3} = \frac{1}{N}\sum_{x_1}\delta_{x_1,0} = \frac{1}{N}, \tag{C.25}$$

$$\text{crossed}: \frac{1}{N^2}\sum_{a_i}\delta_{x_1,x_3}\delta_{k_2,k_4}e^{ik_2x_1}e^{-ik_2x_3}e^{ik_2x_3}e^{ik_4x_3} = \frac{1}{N}\sum_{x_1}\delta_{x_1,0} = \frac{1}{N}, \tag{C.26}$$

$\implies$ crossed diagram not suppressed.

So, we conclude that crossed two-particle diagrams are not suppressed in the single-particle model.

Appendix D

Effective Liouvillians for second-moment dynamics

D.1 Second-moment dynamics of Model C in the strong-noise limit

Application of Itô's lemma enables us to write down the stochastic differential equation for the second moment of the density matrix in model C

$$\begin{aligned} d(\rho \otimes \rho) = -i[\mathcal{H}, \rho \otimes \rho]\, dt - i\sqrt{g} \sum_j [\Sigma_j^z, \rho \otimes \rho]\, dB_t^j \\ - \frac{g}{2} \sum_j [\Sigma_j^z, [\Sigma_j^z, \rho \otimes \rho]]\, dt, \end{aligned} \tag{D.1}$$

which upon averaging leaves us with

$$\partial_t \overline{\rho \otimes \rho} = -i[\mathcal{H}, \overline{\rho \otimes \rho}] - \frac{g}{2} \sum_j [\Sigma_j^z, [\Sigma_j^z, \overline{\rho \otimes \rho}]] \tag{D.2}$$

where we have adopted analogous notation to that of (6.22), i.e., $\Sigma_j^z = Z_j \otimes \mathbb{1} + \mathbb{1} \otimes Z_j$. In the strong-noise limit, the dynamics is projected onto the 6^N slow subspace $\mathcal{S}$ spanned by $\{|z_1\rangle \langle z_1| \otimes |z_2\rangle \langle z_2|, |z_3\rangle \langle -z_3| \otimes |-z_3\rangle \langle z_3| \,:\, z_i \in \{-1, 1\}\}^{\otimes N}$. The first nonvanishing term in perturbation theory for the generator of the strong-noise dynamics of the second moment of the density matrix, which we also refer to as an effective Liouvillian, is given by $\mathcal{L}_{\text{eff}} = -\mathcal{P}_{\mathcal{S}} L_H D^{-1} L_H \mathcal{P}_{\mathcal{S}}$. If we consider the action of DL_H on a single site, we have

$$\begin{aligned} &DL_H\left(|z_1\rangle \langle z_{1'}| \otimes |z_2\rangle \langle z_{2'}|\right) = \frac{ig}{2}\Bigg([H, |z_1\rangle \langle z_{1'}|] \otimes |z_2\rangle \langle z_{2'}| \\ &\times \left((z_2^j - z_{2'}^j)^2 + 4\left(1 - \frac{(z_1^j - z_{1'}^j)^2}{4}\right) - 4z_1^j\left(1 - \frac{(z_1^j - z_{1'}^j)^2}{4}\right)(z_2^j - z_{2'}^j)\right) \\ &+ |z_1\rangle \langle z_{1'}| \otimes [H, |z_2\rangle \langle z_{2'}|] \\ &\times \left((z_1^j - z_{1'}^j)^2 + 4\left(1 - \frac{(z_2^j - z_{2'}^j)^2}{4}\right) - 4z_2^j\left(1 - \frac{(z_2^j - z_{2'}^j)^2}{4}\right)(z_1^j - z_{1'}^j)\right)\Bigg), \end{aligned} \tag{D.3}$$

from which it follows that $L_H \mathcal{P}_\mathcal{S}\left(\overline{\rho\otimes\rho}\right)$ is an eigenstate of D with eigenvalue 4. The effective Liouvillian can thus be written

$$\mathcal{L}_{\text{eff}} = -\frac{1}{2g}\mathcal{P}_\mathcal{S}\,\text{ad}^2_{\mathcal{H}}, \tag{D.4}$$

where we have used the adjoint action notation $\text{ad}_\mathcal{H}(\cdots) := [\mathcal{H},\cdots]$.

In the strong-noise limit, the dynamics is projected onto the 6^N-dimensional slow subspace $\mathcal{S}$ spanned by $\{|z_1\rangle\langle z_1|\otimes|z_2\rangle\langle z_2|, |z_3\rangle\langle -z_3|\otimes|-z_3\rangle\langle z_3| \,:\, z_i\in\{-1,1\}\}^{\otimes N}$. It is helpful to partition the single-site factors of $\mathcal{S}$ into three types of pairs of states

$$\begin{array}{lll} 1. & (11,11) & (-1-1,-1-1) \\ 2. & (11,-1-1) & (-1-1,11) \\ 3. & (1-1,-11) & (-11,1-1), \end{array} \tag{D.5}$$

where we have represented the state $|z_1\rangle\langle z_2|\otimes|z_3\rangle\langle z_4|$ by the tuple (z_1z_2, z_3z_4). It is helpful to visualise each pair of states as occupying antipodal vertices of an octahedron. If we consider the effective Liouvillian, which differs from that of model C only by a multiplicative constant and the fact that the projector is into a different slow subspace, we identify three classes of matrix element (with the possible values given in parenthesis, and their representation on the octahedron given in Fig. D.1):

1. Pair changing (±2): A pair of a given type, with each element of the pair occupying adjacent sites, may be transformed into a pair of another type.
2. Exchange (±2): The states of adjacent sites may be exchanged, if the two states belong to different pairs.
3. Diagonal (2 or 4): No change, but a constant factor equal to the Hamming distance between the two states is acquired.

The differing signs can be seen to ensure that the both the trace (only pairs 1 and 2 contribute) and purity (only pairs 1 and 3 contribute) of the full density matrix are preserved under evolution.

D.2 Effective Liouvillian for the second moment of model NC

We begin by evaluating the double commutators that arise when $\mathcal{L}_{\text{eff}}$ acts on the basis states of $\mathcal{S}$. If we write the Heisenberg Hamiltonian as $\sum_{j,k} h_{jk}$ for $h_{jk} = \sigma^a_j\sigma^a_k$ (n.b. we shall assume the summation convention only for the upper (i.e. spin) indices), we have

$$\left[h_{jk},\left[h_{jk},\sigma^a_k\right]\right] = 8\left(\sigma^a_k - \sigma^a_j\right) \tag{D.6}$$

$$\left[h_{jk},\left[h_{jk},\sigma^a_j\sigma^b_k\right]\right] = 8\left(\sigma^a_j\sigma^b_k - \sigma^b_j\sigma^a_k\right). \tag{D.7}$$

Since we are considering a Hamiltonian with only a two-body interaction, we only need to consider four possible states: each local factor for the two sites that h_{jk} couples is either $|0\rangle$ or

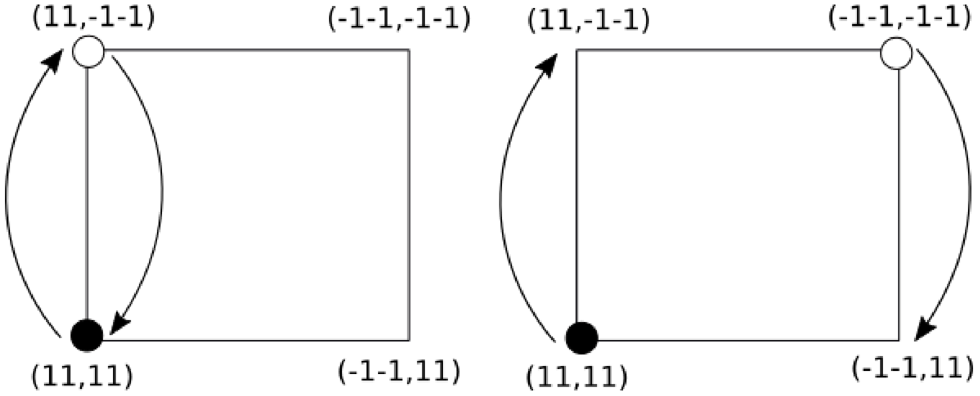

FIGURE D.1: An example of exchange (left) and pair changing (right) terms, as visualised on a square cross section of the ‘octahedron’ of single-site states that span the slow subspace of model C. The filled and empty circles represent the states on adjacent sites.

$|1\rangle$ (as defined in (6.16)). The $|0_j 0_k\rangle$ state is trivially seen to lie in the kernel of $\mathcal{L}_{\text{eff}}$, so that we only need to compute

$$\begin{aligned}\mathcal{L}_{jk}\left(\sigma_j^a\sigma_k^b\otimes\sigma_j^a\sigma_k^b\right) = \mathcal{P}_{\mathcal{S}}\Big[&-8\left(\sigma_j^a\sigma_k^b-\sigma_j^b\sigma_k^a\right)\otimes\sigma_j^a\sigma_k^b\\ &-8\sigma_j^a\sigma_k^b\otimes\left(\sigma_j^a\sigma_k^b-\sigma_j^b\sigma_k^a\right)+16\left(\sigma_k^\alpha-\sigma_j^\alpha\right)\otimes\left(\sigma_k^\alpha-\sigma_j^\alpha\right)\Big].\end{aligned} \tag{D.8}$$

and

$$\begin{aligned}\mathcal{L}_{jk}\left(\mathbb{1}_j\sigma_k^a\otimes\mathbb{1}_j\sigma_k^a\right) = \mathcal{P}_{\mathcal{S}}\Big[&-8\left(\mathbb{1}_j\sigma_k^a-\sigma_j^a\mathbb{1}_k\right)\otimes\mathbb{1}_j\sigma_k^a-\\ 8\mathbb{1}_j\sigma_k^a\otimes\left(\mathbb{1}_j\sigma_k^a-\sigma_j^a\mathbb{1}_k\right)&+8\left(\sigma_j^b\sigma_k^c\otimes\sigma_j^b\sigma_k^c-\sigma_j^b\sigma_k^c\otimes\sigma_j^c\sigma_k^b\right)\Big],\end{aligned} \tag{D.9}$$

with the corresponding result for $|1_j 0_k\rangle$ following by interchanging j and k in the last equality. It remains only to perform the projection back into the slow subspace: terms of the form $\sigma_j^a\mathbb{1}_k\otimes\mathbb{1}_j\sigma_k^a$ are projected out, but $\sigma_j^b\sigma_k^a\otimes\sigma_j^a\sigma_k^b$ terms have a nonzero component in $\mathcal{S}$ that we must compute. This is most clearly seen by decomposing the dyadic Cartesian tensor operator $\sigma_j^a\otimes\sigma_j^b$ into irreducible representations of $SO(3)$ as

$$\begin{aligned}\sigma_j^a\otimes\sigma_j^b &= \frac{1}{3}\left(\sigma_j^\alpha\otimes\sigma_j^\alpha\right)\delta_{ab}+\frac{1}{2}\left(\sigma_j^a\otimes\sigma_j^b-\sigma_j^b\otimes\sigma_j^a\right)\\ &+\frac{1}{2}\left(\sigma_j^a\otimes\sigma_j^b+\sigma_j^b\otimes\sigma_j^a-\frac{2}{3}\sigma_j^\alpha\otimes\sigma_j^\alpha\delta_{ab}\right),\end{aligned} \tag{D.10}$$

from which it follows that

$$\mathcal{P}_{\mathcal{S}}\left[\sigma_j^b\sigma_k^a\otimes\sigma_j^a\sigma_k^b\right]=\frac{1}{3}\sigma_j^a\sigma_k^b\otimes\sigma_j^a\sigma_k^b. \tag{D.11}$$

Combining these results and exploiting orthogonality of the $\{|0\rangle, |1\rangle\}$ states with respect to the Hilbert-Schmidt inner product yields the matrix given in (6.24).

Bibliography

[1] P. Kos, M. Ljubotina, and T. Prosen, Phys. Rev. X **8**, 021062 (2018).

[2] N. F. Mott, Proceedings of the Physical Society. Section A **416** (1949).

[3] P. W. Anderson, Physical Review **109**, 1492 (1958).

[4] L. Gor'kov, A. Larkin, and D. Khmel'nitskii, JETP lett (1979).

[5] E. Abrahams, Physical Review Letters **42**, 673 (1979).

[6] P. Vollhardt, D.; Wölfle, in *Electronic phase transitions*, edited by Y. V. Hanke, W.; Kopaev (Elsevier Science Publishers B.V., North-Holland, 1992) Chap. 1, pp. 1–78.

[7] M. Aizenman and S. Molchanov, Communications in Mathematical Physics **157**, 245 (1993).

[8] I. Y. Gol'dshtein, S. A. Molchanov, and L. A. Pastur, Functional Analysis and Its Applications **11**, 1 (1977).

[9] N. F. Mott, Advances in Physics **16**, 49 (1967).

[10] N. F. Mott, Philosophical Magazine **19**, 835 (1969).

[11] L Fleishman and P. Anderson, Physical Review B **21**, 2366 (1980).

[12] B. L Altshuler and A. G. Aronov, in *Electron-Electron Interactions in Disordered Systems*, edited by A. L. Efros and M. Pollak (North-Holland, Amsterdam, 1985), pp. 1–153.

[13] B. L. Altshuler, A. G. Aronov, and D. E. Khmelnitsky, Journal of Physics C: Solid State Physics **15**, 7367 (1982).

[14] D. Basko, I. Aleiner, and B. Altshuler, Annals of Physics **321**, 1126 (2006).

[15] F. Alet and N. Laflorencie, Comptes Rendus Physique (2018) `https://doi.org/10.1016/j.crhy.2018.03.003`.

[16] D. A. Abanin, E. Altman, I. Bloch, and M. Serbyn, (2018).

[17] L. D. J. and L. Y. Bar, Annalen der Physik **529**, 1600350 (2017).

[18] R. Nandkishore and D. A. Huse, Annual Review of Condensed Matter Physics **6**, 15 (2015).

[19] D. A. Huse, R. Nandkishore, and V. Oganesyan, Phys. Rev. B **90**, 174202 (2014).

[20] J. Z. Imbrie, Journal of Statistical Physics **163**, 998 (2016).

[21] J. Z. Imbrie, V. Ros, and A. Scardicchio, Annalen der Physik **529**, 1600278 (2017).

[22] R. Vosk, D. A. Huse, and E. Altman, Phys. Rev. X **5**, 031032 (2015).

[23] A. C. Potter, R. Vasseur, and S. A. Parameswaran, Phys. Rev. X **5**, 031033 (2015).

[24] P. T. Dumitrescu, R. Vasseur, and A. C. Potter, Phys. Rev. Lett. **119**, 110604 (2017).

[25] A. A. Abrikosov, L. P. Gorkov, and D. I. E., *Fundamentals of the Theory of Metals* (North-Holland, Amsterdam, 1988).

[26] A. I. Larkin and D. E. Khmel’nitskiĭ, Soviet Physics Uspekhi **25**, 185 (1982).

[27] S. Chakravarty and A. Schmid, Physics Reports **140**, 193 (1986).

[28] P. Coleman, *Introduction to Many-Body Physics* (Cambridge University Press, Cambridge, 2015).

[29] A. A. Abrikosov, L. P. Gorkov, and D. I. E., *Methods of Quantum Field Theory in Statistical Physics [Reprint]* (Dover Publications, New York, 1976).

[30] J. Rammer, *Quantum transport theory* (Perseus Books, Reading, MA, 1998).

[31] H. Bruus and K. Flensberg, *Many-Body Quantum Theory in Condensed Matter Physics* (Oxford University Press, Oxford, 2004).

[32] D. Delande and C. Texier, “Waves in disordered media and localization phenomena”, Lecture notes, 2015.

[33] J. W. Negele and H. Orland, *Quantum Many-particle Systems* (Perseus Books, Reading, Mass., 1998).

[34] A. L. Fetter and J. D. Walecka, *Quantum Theory of Many-Particle Systems [Reprint]* (Dover Publications, Mineola, N.Y., 2003).

[35] P. Brouwer, “Theory of Many-Particle Systems”, Lecture notes, 2005.

[36] A. Altland and B. D. Simons, *Condensed Matter Field Theory*, 2nd ed. (Cambridge University Press, Cambridge, 2010).

[37] G. D. Mahan, *Many-particle physics*, 3rd ed. (Springer, New York, 2000).

[38] J. Langer and T Neal, Physical Review Letters (1966).

[39] E. P. Wigner, Annals of Mathematics **62**, 548 (1955).

[40] E. P. Wigner, in Proceedings of the fourth canadian mathematical congress (1957), pp. 174–184.

[41] F. J. Dyson, Journal of Mathematical Physics **3**, 140 (1962).

[42] F. J. Dyson, Journal of Mathematical Physics **3**, 157 (1962).

[43] F. J. Dyson, Journal of Mathematical Physics **3**, 166 (1962).

[44] O. Bohigas, M. J. Giannoni, and C. Schmit, Phys. Rev. Lett. **52**, 1 (1984).

[45] M. V. Berry and M. Tabor, Proc. Roy. Soc. A **356**, 375 (1977).

[46] D. J. Thouless, Phys. Rev. Lett. **39**, 1167 (1977).

[47] B. Altshuler and B. Shklovskii, Sov. Phys. JETP **64**, 127 (1986).

[48] A. D. Mirlin and F. Evers, Phys. Rev. B **62**, 7920 (2000).

[49] V. Oganesyan and D. A. Huse, Physical Review B **75**, 155111 (2007).

[50] M. Serbyn and J. E. Moore, Phys. Rev. B **93**, 041424 (2016).

[51] C. L. Bertrand and A. M. García-García, Phys. Rev. B **94**, 144201 (2016).

[52] A. De Luca, B. L. Altshuler, V. E. Kravtsov, and A. Scardicchio, Phys. Rev. Lett. **113**, 046806 (2014).

[53] B. L. Altshuler, E. Cuevas, L. B. Ioffe, and V. E. Kravtsov, Phys. Rev. Lett. **117**, 156601 (2016).

[54] V. E. Kravtsov, I. M. Khaymovich, E Cuevas, and M Amini, New Journal of Physics **17**, 122002 (2015).

[55] B. L. Altshuler, Y. Gefen, A. Kamenev, and L. S. Levitov, Phys. Rev. Lett. **78**, 2803 (1997).

[56] M. Pino, L. B. Ioffe, and B. L. Altshuler, Proceedings of the National Academy of Sciences **113**, 536 (2016).

[57] T. Guhr, A. Müller–Groeling, and H. A. Weidenmüller, Physics Reports **299**, 189 (1998).

[58] M. L. Mehta, *Random Matrices*, 3rd ed. (Elsevier Academic Press, Amsterdam, 2004).

[59] P. J. Forrester, *Log-Gases and Random Matrices*, Vol. 34, London Mathematical Society Monographs (Princeton University Press, Princeton, NJ, 2010).

[60] V. Kravtsov and A. Mirlin, JETP letters **60**, 656 (1994).

[61] A. Andreev and B. Altshuler, Physical review letters **75**, 2 (1995).

[62] E. J. Gumbel, *Statistics of extremes* (Courier, North Chelmsford, MA, 2012).

[63] J.-Y. Fortin and M. Clusel, Journal of Physics A: Mathematical and Theoretical **48**, 183001 (2015).

[64] C. A. Tracy and H. Widom, Physics Letters B **305**, 115 (1993).

[65] B. V. Bronk, Journal of Mathematical Physics **5**, 215 (1964).

[66] C. A. Tracy and H. Widom, Communications in Mathematical Physics **177**, 727 (1996).

[67] P. L. Ferrari, Communications in mathematical physics **252**, 77 (2004).

[68] M. V. Berry, Proc. Roy. Soc. A **400**, 229 (1985).

[69] S. Müller, S. Heusler, P. Braun, F. Haake, and A. Altland, Phys. Rev. Lett. **93**, 014103 (2004).

[70] T. Kottos and U. Smilansky, Phys. Rev. Lett. **79**, 4794 (1997).

[71] T. Kottos and U. Smilansky, Annals of Physics **274**, 76 (1999).

[72] S. Gnutzmann and U. Smilansky, Advances in Physics **55**, 527 (2006).

[73] G Berkolaiko and P Kuchment, *Introduction to Quantum Graphs*, Vol. 186, Mathematical Surveys and Monographs (American Mathematical Society, Providence, RI, 2013).

[74] H. Schanz and U. Smilansky, Chaos, Solitons & Fractals **5**, Quantum Chaos: Present and Future, 1289 (1995).

[75] S. Gnutzmann and A. Altland, Phys. Rev. E **72**, 056215 (2005).

[76] M. C. Gutzwiller, Journal of Mathematical Physics **12**, 343 (1971).

[77] A. Larkin and Y. N. Ovchinnikov, Sov Phys JETP **28**, 1200 (1969).

[78] A. Kitaev, “A simple model of quantum holography”, Talks at KITP, 2015.

[79] D. A. Roberts, D. Stanford, and L. Susskind, Journal of High Energy Physics **2015**, 51 (2015).

[80] B. Swingle and D. Chowdhury, Phys. Rev. B **95**, 060201 (2017).

[81] R.-Q. He and Z.-Y. Lu, Phys. Rev. B **95**, 054201 (2017).

[82] Y. Huang, Y. Zhang, and X. Chen, Annalen der Physik **529**, 1600318 (2017).

[83] R. Fan, P. Zhang, H. Shen, and H. Zhai, Science Bulletin **62**, 707 (2017).

[84] J. H. Bardarson, F. Pollmann, and J. E. Moore, Phys. Rev. Lett. **109**, 017202 (2012).

[85] H. Kim and D. A. Huse, Physical review letters **111**, 127205 (2013).

[86] J. Maldacena, S. H. Shenker, and D. Stanford, Journal of High Energy Physics **2016**, 106 (2016).

[87] D. Stanford, J. High Energ. Phys. **9** (2016).

[88] A. A. Patel, D. Chowdhury, S. Sachdev, and B. Swingle, Phys. Rev. X **7**, 031047 (2017).

[89] A. M. Lyapunov, International Journal of Control **55**, Originally published in Russian in 1892, 531 (1992).

[90] Y. Sekino and L. Susskind, Journal of High Energy Physics **2008**, 065 (2008).

[91] T. Rakovszky, F. Pollmann, and C. von Keyserlingk, arXiv preprint arXiv:1710.09827 (2017).

[92] A. Nahum, S. Vijay, and J. Haah, Physical Review X **8**, 021014 (2018).

[93] C. von Keyserlingk, T. Rakovszky, F. Pollmann, and S. Sondhi, Physical Review X **8**, 021013 (2018).

[94] V. Khemani, A. Vishwanath, and D. A. Huse, arXiv preprint arXiv:1710.09835 (2017).

[95] S. Xu and B. Swingle, arXiv preprint arXiv:1805.05376 (2018).

[96] Y. Y. Goldschmidt, Phys. Rev. B **41**, 4858 (1990).

[97] C. R. Laumann, A. Pal, and A. Scardicchio, Physical Review Letters **113**, 200405 (2014).

[98] C. L. Baldwin, C. R. Laumann, A. Pal, and A. Scardicchio, (2015).

[99] B. Altshuler, H. Krovi, and J. Roland, Proceedings of the National Academy of Sciences of the United States of America **107**, 12446 (2010).

[100] B. Derrida, Physical Review Letters **45**, 79 (1980).

[101] B. Derrida, Physical Review B **24**, 2613 (1981).

[102] C. Garban, *Selected Works of Oded Schramm* (Springer, New York, 2011).

[103] A. Altland and T. Micklitz, Phys. Rev. Lett. **118**, 127202 (2017).

[104] A. N. Shirayev, *Probability*, 2nd ed. (Springer-Verlag, New York, 1996).

[105] P Diaconis, Random Structures & Algorithms **1**, 51 (1990).

[106] C. Moore and S. Mertens, *The Nature of Computation* (Oxford University Press, Oxford, 2011).

[107] S. Hikami, Physical Review B **24**, 2671 (1981).

[108] I. L. Aleiner and A. I. Larkin, Physical Review B **54**, 14423 (1996).

[109] K. S. Gibbons, M. J. Hoffman, and W. K. Wootters, Phys. Rev. A **70**, 062101 (2004).

[110] G. F. Jonsson and L. N. Trefethen, in *Numerical analysis*, edited by D. F. Griffiths, D. J. Higham, and G. A. Watson (Addison Wesley Longman, 1998), pp. 150–178.

[111] C. M. Caves, C. A. Fuchs, and R. Schack, Journal of Mathematical Physics **43**, 4537 (2002).

[112] M. Tabor, Physica D: Nonlinear Phenomena **6**, 195 (1983).

[113] F. Haake, *Quantum Signatures of Chaos* (Springer-verlag, Berlin, 2010).

[114] A. Lazarides, A. Das, and R. Moessner, Phys. Rev. Lett. **115**, 030402 (2015).

[115] P. Ponte, Z. Papi ć, F. m. c. Huveneers, and D. A. Abanin, Phys. Rev. Lett. **114**, 140401 (2015).

[116] I. K. Zharekeshev and B. Kramer, Physica A: Statistical Mechanics and its Applications **266**, 450 (1999).

[117] P Gaspard, S. A. Rice, H. J. Mikeska, and K Nakamura, Physical Review A **42**, 4015 (1990).

[118] O. Bohigas, M. J. Giannoni, and C. Schmit, Journal de Physique Lettres **45**, 1015 (1984).

[119] Z. Pluha ř and H. A. Weidenmüller, Phys. Rev. Lett. **112**, 144102 (2014).

[120] Z. Pluha ř and H. A. Weidenmüller, Journal of Physics A: Mathematical and Theoretical **48**, 275102 (2015).

[121] G Berkolaiko and J. P. Keating, Journal of Physics A: Mathematical and General **32**, 7827 (1999).

[122] G Berkolaiko, J. P. Keating, and B Winn, Communications in Mathematical Physics **250**, 259 (2004).

[123] G. Tanner, Journal of Physics A: Mathematical and General **34**, 8485 (2001).

[124] A. Altland and D. Bagrets, Nuclear Physics B **930**, 45 (2018).

[125] A. Chan, A. De Luca, and J. Chalker, arXiv preprint arXiv:1803.03841 (2018).

[126] H Gharibyan, M Hanada, S. H. Shenker, and M Tezuka, arXiv:1803.08050 (2018).

[127] G Berkolaiko and P Kuchment, in *Quantum Graphs and Their Applications*, Vol. 415, edited by S. F. G. Berkolaiko R. Carlson and P. Kuchment, Contemporary Mathematics (American Mathematical Society, Providence, RI, 2006), pp. 35–50.

[128] K. Richter and M. Sieber, Phys. Rev. Lett. **89**, 206801 (2002).

[129] S. Gnutzmann and A. Altland, Phys. Rev. Lett. **93**, 194101 (2004).

[130] N. Argaman, Phys. Rev. B **53**, 7035 (1996).

[131] R. S. Whitney, I. V. Lerner, and R. A. Smith, Waves in Random Media **9**, 179 (1999).

[132] N. Rosenzweig and C. E. Porter, Phys. Rev. **120**, 1698 (1960).

[133] H. Kunz and B. Shapiro, Phys. Rev. E **58**, 400 (1998).

[134] A. Altland, M. Janssen, and B. Shapiro, Phys. Rev. E **56**, 1471 (1997).

[135] R. Carmona, A. Klein, and F. Martinelli, Communications in Mathematical Physics **108**, 41 (1987).

[136] T. Tao, *Random Matrices*, Vol. 132, Graduate Studies in Mathematics (American Mathematical Society, Providence, RI, 2017).

[137] R. Speicher, Jahresber. Dtsch. Math. Ver., 3 (2017).

[138] J. A. Mingo and R Speicher, *Free Probability and Random Matrices* (Springer, New York, 2017).

[139] D. Voiculescu, Journal of Functional Analysis **66**, 323 (1986).

[140] R. Speicher, Mathematische Annalen **298**, 611 (1994).

[141] D. Voiculescu, Inventiones Mathematicae **104**, 201 (1991).

[142] D. Voiculescu, International Mathematics Research Notices **1998**, 41 (1998).

[143] R. Speicher, Publications of the Research Institute for Mathematical Sciences **29**, 731 (1993).

[144] J. Chen, E. Hontz, J. Moix, M. Welborn, T. Van Voorhis, A. Suárez, R. Movassagh, and A. Edelman, Phys. Rev. Lett. **109**, 036403 (2012).

[145] M. Welborn, J. Chen, and T. Van Voorhis, Phys. Rev. B **88**, 205113 (2013).

[146] H.-P. Breuer and F. Petruccione, *The theory of open quantum systems* (Oxford University Press, 2002).

[147] D. Gottesman, "Stabilizer codes and quantum error correction", PhD thesis (California Institute of Technology, Pasadena, Ca, 1997).

[148] C. Nayak, S. H. Simon, A. Stern, M. Freedman, and S. Das Sarma, Rev. Mod. Phys. **80**, 1083 (2008).

[149] P. Zanardi and M. Rasetti, Physical Review Letters **79**, 3306 (1997).

[150] J. Kempe, D. Bacon, D. A. Lidar, and K. B. Whaley, Physical Review A **63**, 042307 (2001).

[151] O. Golinelli and K. Mallick, Journal of Physics A: Mathematical and General **39**, 12679 (2006).

[152] T. Prosen, New Journal of Physics **10**, 043026 (2008).

[153] T. Prosen and T. H. Seligman, Journal of Physics A: Mathematical and Theoretical **43**, 392004 (2010).

[154] M. V. Medvedyeva, F. H. Essler, and T. Prosen, Physical Review Letters **117**, 137202 (2016).

[155] L. Banchi, D. Burgarth, and M. J. Kastoryano, Phys. Rev. X **7**, 041015 (2017).

[156] J. Jeske and J. H. Cole, Phys. Rev. A **87**, 052138 (2013).

[157] M. H. Devoret and J. M. Martinis, in *Experimental aspects of quantum computing* (Springer, 2005), pp. 163–203.

[158] H Haken and G Strobl, Zeitschrift für Physik A Hadrons and Nuclei **262**, 135 (1973).

[159] M. Mohseni, P. Rebentrost, S. Lloyd, and A. Aspuru-Guzik, The Journal of Chemical Physics **129**, 174106 (2008).

[160] N. Trautmann and P. Hauke, Physical Review A **97**, 0236 (2017).

[161] R. L. Taylor, C. D. Bentley, J. S. Pedernales, L. Lamata, E. Solano, A. R. Carvalho, and J. J. Hope, Scientific Reports **7**, 46197 (2017).

[162] J. Hauss, A. Fedorov, C. Hutter, A. Shnirman, and G. Schön, Physical Review Letters **100**, 037003 (2008).

[163] A. Beige, D. Braun, B. Tregenna, and P. L. Knight, Physical Review Letters **85**, 1762 (2000).

[164] R. H. Dicke, Physical Review **93**, 99 (1954).

[165] B. M. Garraway, Philosophical Transactions of the Royal Society of London A: Mathematical, Physical and Engineering Sciences **369**, 1137 (2011).

[166] A. Belavin, B. Y. Zeldovich, A. Perelomov, and V. Popov, Sov. Phys. JETP **56**, 264 (1969).

[167] G. Agarwal, Physical Review A **2**, 2038 (1970).

[168] R Bonifacio, P Schwendimann, and F. Haake, Physical Review A **4**, 302 (1971).

[169] R Bonifacio, P Schwendimann, and F. Haake, Physical Review A **4**, 854 (1971).

[170] J Dukelsky, S Pittel, and G Sierra, Reviews of modern physics **76**, 643 (2004).

[171] U. Fano, Reviews of Modern Physics **29**, 74 (1957).

[172] C. Gardiner and M. Collett, Physical Review A **31**, 3761 (1985).

[173] A. Barchielli, Physical Review A **34**, 1642 (1986).

[174] G. C. Ghirardi, P. Pearle, and A. Rimini, Phys. Rev. A **42**, 78 (1990).

[175] S. L. Adler, Physics Letters A **265**, 58 (2000).

[176] M. Bauer, D. Bernard, and A. Tilloy, Phys. Rev. A **88**, 062340 (2013).

[177] M. Bauer, D. Bernard, and T. Jin, SciPost Physics **3**, 033 (2017).

[178] A Chenu, M Beau, J Cao, and A Del Campo, Physical Review Letters **118**, 140403 (2017).

[179] H. Lipkin, N. Meshkov, and A. Glick, Nuclear Physics **62**, 188 (1965).

[180] F. R. Bernhart, Discrete Mathematics **204**, 73 (1999).

[181] N. J. A. Sloane, *The on-line encyclopedia of integer sequences*, 2017.

[182] D. L. Andrews and T. Thirunamachandran, The Journal of Chemical Physics **67**, 5026 (1977).

[183] J. Links, H.-Q. Zhou, R. H. McKenzie, and M. D. Gould, Journal of Physics A: Mathematical and General **36**, R63 (2003).

[184] A. Monin and A. Yaglom, *Statistical fluid mechanics, volume ii: mechanics of turbulence*, Vol. 2 (Courier Corporation, 2013).

[185] E. N. Lorenz, Tellus **21**, 289 (1969).

[186] D. Ruelle, Physics Letters A **72**, 81 (1979).

[187] P. Hayden and J. Preskill, Journal of High Energy Physics **2007**, 120 (2007).

[188] N. Lashkari, D. Stanford, M. Hastings, T. Osborne, and P. Hayden, Journal of High Energy Physics **2013**, 22 (2013).

[189] S. H. Shenker and D. Stanford, Journal of High Energy Physics **2014**, 67 (2014).

[190] S. H. Shenker and D. Stanford, Journal of High Energy Physics **2014**, 46 (2014).

[191] D. A. Roberts and D. Stanford, Physical review letters **115**, 131603 (2015).

[192] W. W. Ho and D. A. Abanin, Physical Review B **95**, 094302 (2017).

[193] S. Gopalakrishnan and B. Zakirov, arXiv preprint arXiv:1802.07729 (2018).

[194] A. Lucas, arXiv preprint arXiv:1710.01005 (2018).

[195] D. A. Roberts, D. Stanford, and A. Streicher, arXiv preprint arXiv:1802.02633 (2018).

[196] Y. Takahasi and H. Umezawa, Collect. Phenom. **2**, 55 (1974).

[197] J. Polchinski and V. Rosenhaus, Journal of High Energy Physics **2016**, 1 (2016).

[198] D. Bagrets, A. Altland, and A. Kamenev, Nuclear Physics B **921**, 727 (2017).

[199] X. Chen, T. Zhou, D. A. Huse, and E. Fradkin, Annalen der Physik **529**, 1600332 (2016).

[200] I. L. Aleiner, L. Faoro, and L. B. Ioffe, Annals of Physics **375**, 378 (2016).

[201] E. B. Rozenbaum, S. Ganeshan, and V. Galitski, Physical review letters **118**, 086801 (2017).

[202] D. Bernard, M. Bauer, and T. Jin, SciPost Physics **3**, 033 (2017).

[203] J. Preskill, arXiv preprint arXiv:1801.00862 (2018).

[204] M. Mezei and D. Stanford, Journal of High Energy Physics **2017**, 65 (2017).

[205] A. Chan, A. De Luca, and J. Chalker, arXiv preprint arXiv:1712.06836 (2017).

[206] C. Jonay, D. A. Huse, and A. Nahum, arXiv preprint arXiv:1803.00089 (2018).

[207] T. Zhou and A. Nahum, arXiv preprint arXiv:1804.09737 (2018).

[208] G. Bentsen, Y. Gu, and A. Lucas, arXiv preprint arXiv:1805.08215 (2018).

[209] C. Sünderhauf, D. Pérez-García, D. A. Huse, N. Schuch, and J. I. Cirac, arXiv preprint arXiv:1805.08487 (2018).

[210] R Oliveira, O. Dahlsten, and M. Plenio, Physical review letters **98**, 130502 (2007).

[211] O. C. Dahlsten, R. Oliveira, and M. B. Plenio, Journal of Physics A: Mathematical and Theoretical **40**, 8081 (2007).

[212] M. Žnidarič, Physical Review A **76**, 012318 (2007).

[213] M. Žnidarič, Physical Review A **78**, 032324 (2008).

[214] G. H. Fredrickson and H. C. Andersen, Physical review letters **53**, 1244 (1984).

[215] J. P. Garrahan, P. Sollich, and C. Toninelli, Dynamical heterogeneities in glasses, colloids, and granular media **150**, 111 (2011).

[216] S. Gopalakrishnan, arXiv preprint arXiv:1806.04156 (2018).

[217] Z. Cai and T. Barthel, Phys. Rev. Lett. **111**, 150403 (2013).

[218] P. L. Krapivsky, S. Redner, and E. Ben-Naim, *A kinetic view of statistical physics* (Cambridge University Press, 2010).

[219] I. Lesanovsky and J. P. Garrahan, Phys. Rev. Lett. **111**, 215305.

[220] J. R. G Mendonça, Journal of Physics A: Mathematical and Theoretical **46**, 295001 (2013).

[221] V. Eisler, Journal of Statistical Mechanics: Theory and Experiment **2011**, P06007 (2011).

[222] N Cancrini, F Martinelli, C Roberto, and C Toninelli, Probability Theory and Related Fields **140**, 459 (2008).

[223] O. Blondel, A. Deshayes, and C. Toninelli, arXiv preprint arXiv:1803.08761 (2018).

[224] I. S. Graham, L. Piche, and M. Grant, Journal of Physics: Condensed Matter **5**, L349 (1993).

[225] O. Blondel, Stochastic Processes and their Applications **123**, 3430 (2013).

[226] S. Léonard and P. Harrowell, The Journal of chemical physics **133**, 244502 (2010).

[227] I. Douglass and P. Harrowell, The Journal of chemical physics **138**, 12A516 (2013).

[228] R. Gutiérrez and J. P. Garrahan, Journal of Statistical Mechanics: Theory and Experiment **2016**, 074005 (2016).

[229] M. Kardar, G. Parisi, and Y.-C. Zhang, Physical Review Letters **56**, 889 (1986).

[230] M. Kardar, *Statistical physics of fields* (Cambridge University Press, 2007).

[231] T. Kriecherbauer and J. Krug, Journal of Physics A: Mathematical and Theoretical **43**, 403001 (2010).

[232] M. Prähofer and H. Spohn, Physical review letters **84**, 4882 (2000).

[233] J. Baik and E. M. Rains, Random matrix models and their applications **40**, 1 (2001).

[234] R Friedberg and J. E. Cameron, The Journal of Chemical Physics **52**, 6049 (1970).

[235] L. Jacobs and C. Rebbi, Journal of Computational Physics **41**, 203 (1981).

[236] D. P. Landau and K. Binder, *A guide to monte carlo simulations in statistical physics* (Cambridge university press, 2014).

[237] T. Zhou and A. Nahum, arXiv preprint arXiv:1804.09737 (2018).

[238] M. Knap, arXiv preprint arXiv:1806.04686 (2018).

[239] J. Cotler, C.-M. Jian, X.-L. Qi, and F. Wilczek, arXiv preprint arXiv:1711.03119 (2017).

[240] P. Delsarte and V. I. Levenshtein, IEEE Transactions on Information Theory **44**, 2477 (1998).